

Development and Evaluation of Computerized Segmentation

Algorithm for 3D Multimodality Breast Images

BY

HSIEN-CHI KUO

B.S., National Taiwan University, 2006

THESIS

Submitted as partial fulfillment of the requirements
for the degree of Doctor of Philosophy in Bioengineering
in the Graduate College of the
University of Illinois at Chicago, 2014

Chicago, Illinois

Defense Committee:

Richard L. Magin, Chair
Maryellen L. Giger, Advisor, The University of Chicago
Rashid Ansari, Electrical and Computer Engineering
John R. Hetling
Ingrid Reiser, The University of Chicago

This dissertation is dedicated to my parents and my godfather.

Acknowledgements

I would like to thank my thesis committee – Dr. Richard L. Magin, Dr. Maryellen L. Giger, Dr. Rashid Ansari, Dr. John R. Hetling, and Dr. Ingrid Reiser – for their unwavering support and assistance. They provided guidance in all areas that helped me accomplish my research goals, and also gave me enough freedom so that I could conduct my work with my own pace. I would also like to acknowledge Dr. Karen Drukker, who made substantial contribution to help complete this study.

A number of individuals and institutions were extremely helpful to me regarding to data collection – at The University of Chicago Medical Center, Alexandra Edwards; at University of California at Davis Medical Center, Dr. John M. Boone, Dr. Karen K. Lindfors, and Dr. Kai Yang; and U-Systems, Inc., a GE company, Sunnyvale, CA.

Contribution of Authors

Chapter I is a literature and background review that places the dissertation questions in the context and highlights the significance of the research question. Chapter II describes the materials used in this research. Chapter III represents published manuscripts [68][74] for which I was the primary author and major driver of the research. Dr. Maryellen Giger and Dr. Ingrid Reiser contributed to the writing. Chapter IV represents a published manuscript [75] for which I was the first author and the main conductor of the research. Dr. Maryellen Giger and Dr. Ingrid Reiser contributed to the writing. Chapter V is a manuscript that has just been accepted for journal publication. I was the first author and main conductor of this research. Dr. Maryellen Giger, Dr. Ingrid Reiser, and Dr. Karen Drukker contributed to the writing. Chapter VI represents an unpublished study that aims to evaluate my proposed segmentation model and create a new independent feature for improving computer-aided diagnosis performance. This part of research was submitted for publication and is under review now. Chapter VII represents a preliminary study that is partially published [72] for which I was the primary author and research conductor. Dr. Maryellen Giger, Dr. Ingrid Reiser, and Dr. Karen Drukker contributed to the writing. Chapter VIII is a synthesis and the conclusion of this dissertation. Some suggestions for future research directions in this field are also included.

TABLE OF CONTENTS

<u>CHAPTER</u>	<u>PAGE</u>
I. INTRODUCTION	1
A. Breast Cancer and Breast Imaging	1
1. Breast Cancer and Mammography	1
2. Dedicated Breast CT in Early Days	3
3. Imaging of the Breast with A Conventional Whole-body CT Scanner	4
4. Dedicated Breast CT with Cone Beam X-ray	6
5. 3D Breast Ultrasound	11
B. Computer Aided Detection/Diagnosis (CAD)	13
1. Introduction to CAD	13
a. Computer Aided Detection	16
b. Computer Aided Diagnosis	16
2. CAD and Breast Cancer	17
3. Future of CAD	20
C. Overview of Segmentation on Medical Images	21
1. Thresholding	21
2. Region Growing	22
3. Classifiers and Clustering	22
4. Markov Random Field Models	24
5. Artificial Neural Networks	24
6. Deformable Models	25
7. Other Approaches	26
D. Hypothesis and Specific Aims	26
II. IMAGE DATABASE	28
III. DEVELOPMENT OF 3D LESION SEGMENTATION FOR DEDICATED BREAST CT	31
A. Introduction	31
B. Segmentation Methods	34
1. Contour Initialization	38
2. Original Level Set Model	40
3. Proposed Level Set Model	44

TABLE OF CONTENTS (continued)

<u>CHAPTER</u>	<u>PAGE</u>
4. Stopping Criteria	46
5. Evaluation	47
C. Results	48
D. Discussion and Conclusion	51
IV. APPLICATION OF THE PROPOSED SEGMENTATION MODEL ON UNENHANCED bCT IMAGES	59
A. Introduction	59
B. Materials and Methods	59
C. Results	60
D. Discussion and Conclusion	62
V. OPTIMIZATION OF THE SEGMENTATION MODEL	65
A. Introduction	65
B. Segmentation Methods	66
1. Contour Initialization	66
2. Modified Active Contour Model with Local Energy Term	68
a. Derivation of Level-Set Evolution Function from the New Energy Functional	70
b. Dynamic Stopping Criterion	76
3. Segmentation Evaluation	77
a. Segmentation Performance in terms of DICE	77
b. Segmentation Performance and Existing Fibroglandular Tissue on bCT	78
C. Results	79
1. Impact of the New Modification to the Active Contour Method: An Example	79
2. Comparison of Original and Optimized Segmentation Models	80
3. Segmentation Performance and Presenting Fibroglandular Tissue ...	84
D. Discussion and Conclusion	87
VI. TASK-BASED EVALUATION OF LESION SEGMENTATION: FEATURE ANALYSIS AND LESION CLASSIFICATION	90

TABLE OF CONTENTS (continued)

<u>CHAPTER</u>	<u>PAGE</u>
A. Introduction	90
B. Methods	93
1. Morphological and Texture Features	93
2. Feature Selection and Analysis	94
3. Development of the New Spiculation Feature	95
a. Automated Identification of Fibroglandular and Adipose Tissues	95
b. Spiculation Index Computation	96
C. Results	100
1. Comparison of Classification Performance between the Two Segmentation Models	100
2. Feature Analysis with and without Spiculation Index on the Optimized Segmentation Model	102
D. Discussion and Conclusion	110
VII. PRELIMINARY INVESTIGATION OF SEGMENTATION TECHNIQUES ON 3D BREAST ULTRASOUND LESIONS	115
A. Introduction	115
B. Methods	116
C. Results	117
D. Discussion and Conclusion	121
VIII. DISCUSSION AND CONCLUSION	123
CITED LITERATURES	127
VITA	137
APPENDIX	139

LIST OF TABLES

<u>TABLE</u>		<u>PAGE</u>
I.	IMAGE DATABASE OF DEDICATED BREAST CT	28
II.	IMAGE DATABASE OF ABUS	29
III.	SEGMENTATION PERFORMANCE IN TERMS OF AVERAGE OVERLAP RATIO FOR THE THREE STOPPING CRITERIA AND COMPARISON RESULTS IN TERMS OF <i>P</i> -VALUES FROM THE T-TEST	51
IV.	OPTIMIZED ACTIVE CONTOUR MODEL PARAMETER VALUES FOR SEGMENTATION OF BCT LESIONS	76
V.	SEGMENTATION RESULTS FOR CONTRAST-ENHANCED AND NON-CONTRAST-ENHANCED BREAST CT	82
VI.	SEGMENTATION PERFORMANCE WITH DIFFERENT FIBROGLANDULAR CATEGORIES ON BCT	85
VII.	FEATURE VALUES AND AREA UNDER THE ROC CURVE (AUC) OF INDIVIDUAL FEATURE AND COMBINED FEATURES	104
VIII.	CORRELATION COEFFICIENTS AND STATISTICAL SIGNIFICANCE BETWEEN EACH TWO SELECTED FEATURES	105
IX.	SEGMENTATION RESULTS FOR 3D BREAST ULTRASOUND	118

LIST OF FIGURES

<u>FIGURE</u>	<u>PAGE</u>
1. Example image of nowadays digital full-field mammography	2
2. Example image of CT/M image	4
3. Example images of dedicated breast CT	8
4. Example image of automated 3D breast ultrasound	11
5. Schematic diagram of a CAD system	14
6. Components within a CAD system	15
7. Contrast-enhanced and unenhanced breast CT image examples	29
8. Example image of 3D breast ultrasound	30
9. Schematic of the seeded breast CT lesion segmentation algorithm	34
10. Comparison of active contour segmentation with different initial contours	37
11. Demonstration of the RGI segmented contour and the subsequently-eroded contour	39
12. Dedicated breast CT lesion segmentations obtained for different values of $\tau\mu$ with original and proposed level set segmentation model	43
13. Segmentation examples with and without softened indication function ...	45
14. Segmentation examples for the three stopping criteria. $\tau\mu = 0.10$	49
15. Segmentation performance as a function of OR_{ave} threshold for the three stopping criteria	50

LIST OF FIGURES (continued)

<u>FIGURE</u>	<u>PAGE</u>
16. Stopping conditions as a function of iteration number, illustrated for two different masses	54
17. The relationship between OR and DICE	56
18. Comparison of segmentation performance between contrast and non-contrast images with radiologist’s outlines	60
19. Comparison of lesion volume obtained from lesion segmentation in unenhanced or contrast-enhanced breast CT images	62
20. Examples of lesion segmentation in contrast-enhanced bCT images, and unenhanced bCT images	64
21. Flowchart of the optimized automated breast lesion segmentation Scheme	67
22. An example contour generated by the proposed segmentation model in chapter III	69
23. Contrast-enhanced and non-contrast breast CT images, manual delineations, and computer-determined segmentations (using the original model and optimized model) of a lesion with a complicated shape	80
24. The fraction of lesions correctly segmented at various overlap (DICE coefficient) thresholds in bCT	83
25. Comparison of lesion Dice coefficients for the original and optimized segmentation models	84
26. Three different Non-contrast bCT segmentation examples	86
27. A contrast-enhanced bCT image segmentation example	87

LIST OF FIGURES (continued)

<u>FIGURE</u>	<u>PAGE</u>
28. Flowchart of the computation of the spiculation feature for bCT images	96
29. A cross section of a spiculated malignant mass imaged on breast CT ...	97
30. Example of a malignant lesion partially surrounded by, and connected to, fibroglandular tissue	98
31. Illustration of the concept of the spiculation index feature	99
32. Comparison of individual feature classification performance in terms of AUC values between the two segmentation algorithms	101
33. Illustration of the low correlation between the spiculation index and irregularity features	106
34. ROC curves of merged selected features with and without spiculation index	108
35. Examples of small lesions that is limited in both shape information and spiculation index	109
36. The CAD performance in terms of AUC for lesions with effective diameter $d < 11.3$ mm and $d \geq 11.3$ mm	110
37. Segmentation performance in 54 mammographically-occult and 44 Mammographically-positive 3D breast US images	119
38. Two cancer examples of 3D breast ultrasound segmentation	120

LIST OF ABBREVIATIONS

US	Ultrasound
CT	Computerized Tomography
bCT	Breast Computerized Tomography
MDCT	Multidetector Computerized Tomography
HU	Hounsfield Unit
AGD	Average glandular dose
CAD	Computer-aided detection/diagnosis
CADe	Computer-aided detection
CADx	Computer-aided diagnosis
ABUS	Automated 3D breast ultrasound
SNR	Signal-to-noise ratio
PPV	Positive predictive value
LDA	Linear discriminant analysis
ROC	Receiver-operating characteristic
EM	Expectation-maximization
MRF	Markov random field
ANNs	Artificial Neural Networks
BI-RADS	Breast Imaging-Reporting and Data System

LIST OF ABBREVIATIONS (continued)

VOI	Volume of interest
RGI	Radial gradient index
OR	Overlap ratio
OR _{avg}	Average overlap ratio
DICE	Dice coefficient
AUC	Area under the ROC curve

SUMMARY

Breast cancer is the 2nd most common cancer among US women, accounting for approximately 30% of newly diagnosed cancers. The chances of surviving a breast cancer diagnosis and the effectiveness of treatments rely on early detection of the disease. Since mammography has been widely accepted as a screening tool for breast cancer, the mortality rate was significantly reduced from 30 to 40% during the past three decades. However, mammography projects 3D tissue structures of the breast onto a 2D plane and which leads to superimposition resulting in low positive predictive value of biopsies performed based on diagnostic mammography. As a result, misdiagnoses on mammography ultimately drive up healthcare costs, as well as unnecessary patient anxiety

Recently, researchers have been developing CT systems and automated 3D breast ultrasound dedicated solely for breast imaging. Such imaging modalities generate 3D image volumes that completely resolve breast tissue structures and avoid the superimposition effect. However, it also produces large amount of image data that the radiologists need to review. Such data explosion could make image interpretation task even more difficult and time consuming. Therefore, CAD (computer-aided detection/diagnosis) technology is expected to alleviate the burden.

SUMMARY (continued)

Segmentation is an essential step in computer-aided diagnosis scheme. Accurate computer-aided diagnosis often relies on correct segmentation. Thus, the purpose of this work is to describe a segmentation algorithm for dedicated breast CT and automated 3D breast ultrasound. The lesion segmentation algorithm was initially developed on contrast-enhanced breast CT images by combining radial gradient index segmentation and level set based active contour algorithm. Then the segmentation algorithm was further optimized by modifying its corresponding energy functional, and obtained satisfactory segmentation results on both contrast-enhanced and unenhanced breast CT, as well as 3D breast ultrasound in terms of the measure of the overlap of computer segmentation and manually-delineated lesion outlines.

To reach the goal of automated diagnosis, the segmentation results were evaluated by feature analysis. The classification by using lesion shape features (irregularity measures) showed that the proposed segmentation algorithm was able to capture sufficient shape information (area under the receiver operating characteristic curve, $AUC = 0.81$), which is considered one important factor for differentiating tumors. In this study, we firstly developed a new 3D spiculation feature for dedicated breast CT image volumes in order to further improve the classification performance.

SUMMARY (continued)

This new spiculation feature utilizes the 3D structural information in the lesion neighborhood to analyze the lesion surface and evaluate the degree of spiculation. By adding the new spiculation feature, AUC was improved from 0.81 to 0.85 significantly, yielding promising lesion classification performance for our bCT database. In addition, the results suggest that the development of such feature which utilizes 3D information resolved by 3D imaging modalities should be further investigated for future CAD application.

I. INTRODUCTION

A. Breast Cancer and Breast Imaging

1. Breast Cancer and Mammography

Breast cancer is the 2nd most common cancer among US women, accounting for approximately 30% of newly diagnosed cancers. American Cancer Society estimated that 232,340 of new invasive cases would be identified and 39,620 women were expected to die from the disease in 2013 [1]. Since there is currently no cure for breast cancer, early detection by screening plays an important role in reducing mortality [1]. By widely performing X-ray mammography in screening, the breast cancer mortality rate has been decreased by 30% to 50% in the past 20 years [2].

Although X-ray mammography has achieved significant success, there are still considerable limitations of this technique. The poor positive predictive values (4% to 9% in mammography screening, and 39.5% based on biopsy diagnostic mammography) [3] result in a waste of medical resources and unnecessary patient anxiety. Some researchers have even claimed that the reduction of mortality rate is partly contributed by the overdiagnosis of screening [4]. This is due to a fundamental shortcoming of X-ray mammography: X-ray mammography is a 2D projected imaging technique; hence tissue superimposition occurs when 3D tissue structures

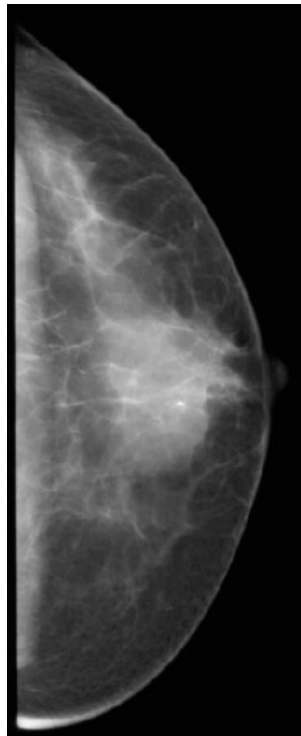


Figure 1. An example of a digital full-field mammography image. The spatial resolution is $50\ \mu\text{m} \times 50\ \mu\text{m}$. [5] (Open access online)

with similar X-ray attenuations are projected onto a 2D plane, including fibroglandular tissues and tumor masses. In addition, when the lesion size is small and is not associated with calcification, it is difficult to be visualized on mammography by the radiologists especially if presenting in a dense breast. In sum, mammograms only provide projected anatomical information of the breast, which is inherently poorer than that expected from 3D imaging.

To address this superimposition problem, investigators are developing 3D breast imaging modalities such as magnetic resonance imaging (MRI), 3D breast ultrasound (3D breast US), and dedicated breast computerized tomography (dedicated bCT). Researchers expect that 3D imaging modalities could retain more anatomical structure leading to more accurate interpretations and diagnoses. This dissertation work is focused on dedicated breast CT and 3D breast ultrasound which are described in the subsequent sections.

2. Dedicated Breast CT in Early Days

At the same time when screening mammography started to spread widely in the US, the General Electric (GE) company began to construct a prototype of dedicated breast CT scanner, which was called CT/M [2][6][7][8]. The GE CT/M scanner used fan-beam geometry to acquire 1-cm-thick CT slices in approximately 10s. Women were imaged in the prone position while lying on a table where there was an opening for the breast. It is reported that the absorbed dose of the central 6 slices (6 cm) was 1.75 mGy [2]. However, compared to conventional mammography, the resolution was very poor ($1.56 \text{ mm} \times 1.56 \text{ mm} \times 1 \text{ cm}$ for CT/M; $< 70 \text{ }\mu\text{m} \times < 70 \text{ }\mu\text{m}$ for mammography) which resulted in low specificity (70%) [7][5]. In addition, the need of iodine contrast infusion was invasive and led to high costs. Ultimately, Chang

et al. [7] concluded that CT/M scanner for screening was not desirable, which prompted GE to terminate the CT/M system in the market [2].

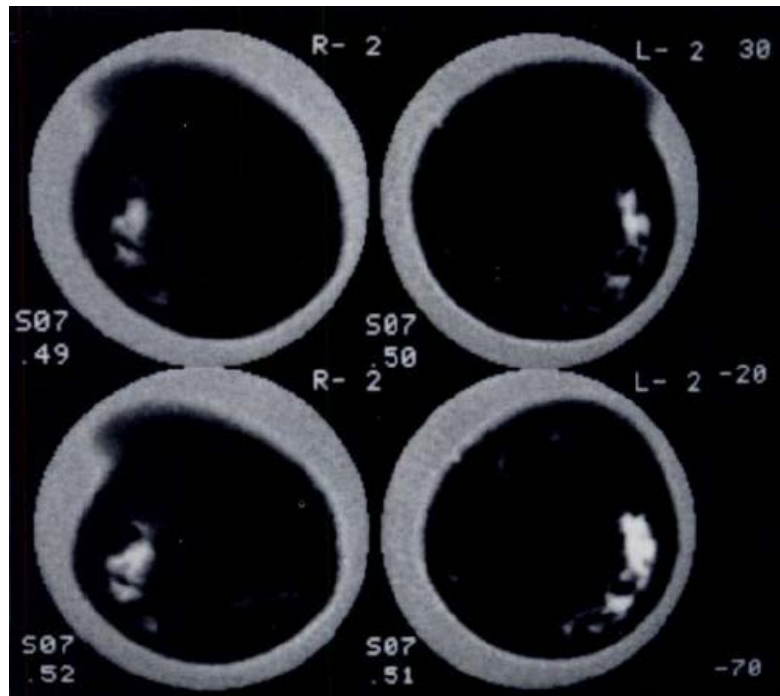


Figure 2. Example images of CT/M as facing the patient. Above row: both breasts imaged before contrast material injected. Below: both breasts imaged after contrast material injected. The bright area was diagnosed as grade 4 adenocarcinoma. [8] (Open access online)

3. Imaging of the Breast with a Conventional Whole-body CT Scanner

After the prototype GE CT/M dedicated breast scanner, some studies were conducted to investigate breast CT with a conventional whole-body CT scanner.

Patients were imaged in the prone position with the help of foam blocks to allow the breast to hang freely. In the 1990's, substantial improvements were made in CT technology. Since then, researchers used multidetector CT (MDCT) scanners with a protocol involving intravenous infusion of nonionic iodine contrast media to evaluate breast lesions. MDCT scanners can generate CT images in short time and thus provide the possibility of using dynamic CT to aid in breast lesion differentiation based on the uptake and washout rates of the contrast agent [2]. A recent study reported that the reconstructed projection based on this technique had resolution $1 \text{ mm} \times 1 \text{ mm} \times 3 \text{ mm}$, and achieved sensitivity of 90% but with low specificity of 55% [9]. For this reason, the primary application of MDCT in breast cancer has been a diagnostic tool for staging malignant tumors. Because of the low specificity, the possibility of the use of this imaging approach for differentiating breast lesions is very limited; especially given that image-guided needle biopsy, an alternate approach, has been shown to be very accurate in such tasks [2].

The radiation dose is another factor that limits this technique as a good screening tool. Miyake et al. [9] measured a breast radiation dose of 23.5 mGy, which is about 10 times that of conventional mammography. Even though other researchers attempted to use low-dose CT imaging as 6.51 mGy, 2.68 mGy, and 1.65 mGy, the results showed a penalty in diagnostic accuracy with reduction of the radiation dose [10]. It should be

also noted that by imaging breast with a conventional whole-body CT scanner, X-ray penetrates through the entire thorax, and thus a large amount of tissues other than breast is exposed to radiation as well.

4. Dedicated Breast CT with Cone Beam X-ray

Recently, the advent of digital flat-panel detectors for mammography prompted researchers to design and develop CT systems that are dedicated only for imaging the breast. There are a number of academic groups and small start-up companies investigating dedicated breast CT imaging with similar systems, including University of California (UC) at Davis, University of Rochester, Duke University, University of Massachusetts, University of Texas (UT) M.D. Anderson Cancer Center, Emory University, etc. In our studies, the images were acquired from UC Davis under an IRB(institution review board)-approved protocol. Hence here we use their system setup to demonstrate the imaging concepts.

To image the breast, patients lie prone on a table with an opening for the breast where the breast hangs in the pendant position through the hole in the table. Underneath the table an X-ray tube and a flat panel is equipped on a gantry that allows for rotation around the breast (Fig. 5) [11]. It should be noted that the X-rays

only penetrate the breast rather than the entire thorax as in conventional whole-body CT scanner.

Conventional whole-body CT scanners use detector arrays that are arranged in an arc. The arc usually spans an angle of about 60° , and the fan beam X-ray width in the z-axis direction typically spans from 20 to 40 mm. Unlike conventional whole-body CT scanners, dedicated breast CT systems generally use a flat panel detector with a cone beam X-ray source. Such setup covers the full extent in the z-dimension and allows for a complete CT dataset of the breast in one rotation (Fig. 6) [12]. The UC-Davis system uses the PAXSCAN flat panel detector (Varian Imaging Systems, Slat Lake City, UT, USA), which has a $40\text{ cm} \times 30\text{ cm}$ field of view and represents a 2048×1536 array of $194\ \mu\text{m} \times 194\ \mu\text{m}$ detector elements. Effective pixel size is $388\ \mu\text{m} \times 388\ \mu\text{m}$ due to projection images being acquired in a 2×2 acquisition mode with a readout array of 1024×768 . With 30 frames per second, the resulting projection contains 500 frames acquired over about 16.6 seconds. The reconstruction algorithm results in an isotropic 3D CT volume, consisting of 1 series of 512×512 images [12]. The radiation dose evaluated using a phantom showed that the dose is equal to that of 2-view mammography [13], which is substantially lower than conventional whole-body CT.

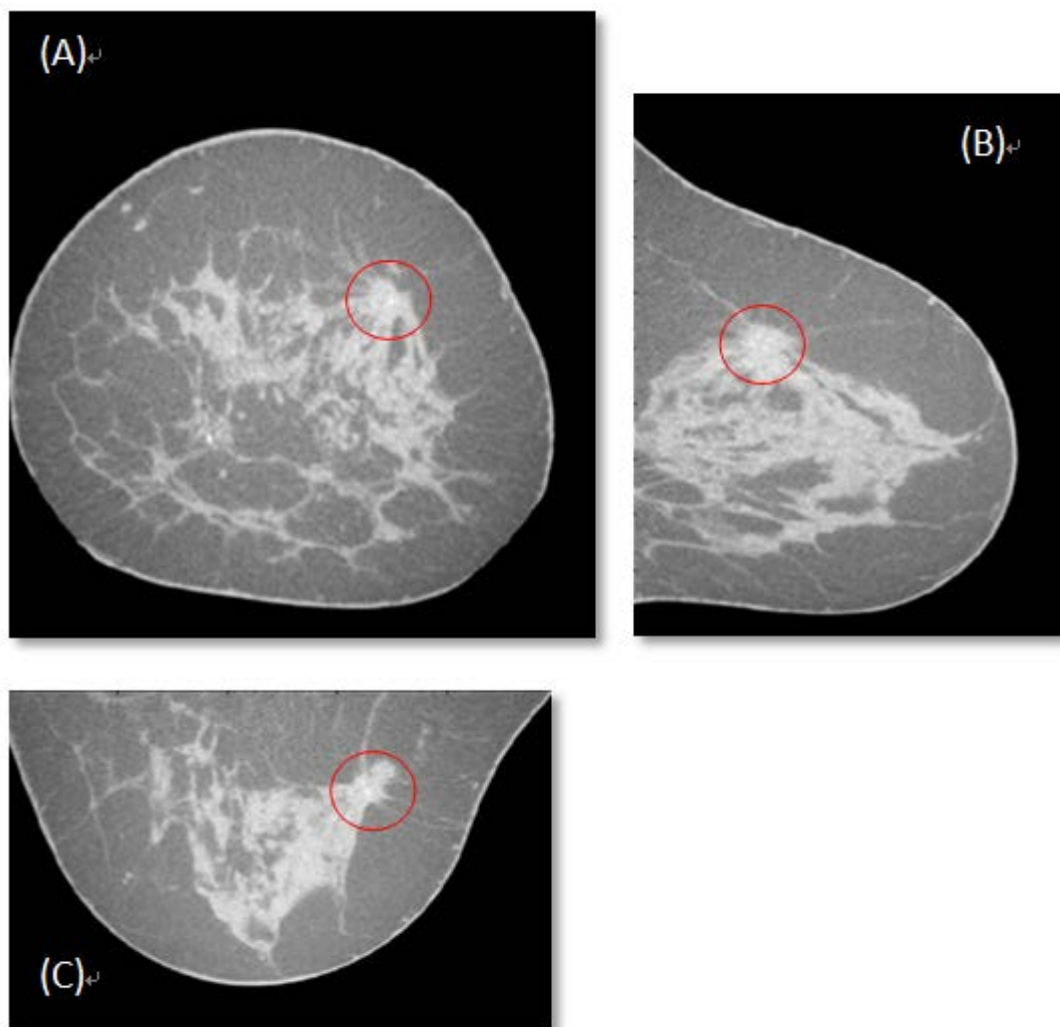


Figure 3. Example image of dedicated breast CT. The breast is viewed in 3 orthogonal directions. (A) is displayed in coronal plane, (B) Sagittal plane, (C) Transverse plane. Red circle indicates a malignant tumor labeled by the radiologist.

The first comparison of dedicated bCT with screen-film mammography was reported in 2008 [14]. This initial study showed that dedicated bCT was significantly better than mammography for visualization of masses ($p = 0.002$) whereas mammography outperformed dedicated bCT for visualization of microcalcifications ($p = 0.006$). No significant differences were found in the diagnosis of malignant or

benign between mammography and dedicated bCT. Volunteers and patients who participated in this study demonstrated a pronounced preference for dedicated bCT over mammography in terms of comfort ($p < 0.001$).

In 2010, another clinical study of dedicated bCT was conducted done with the use of contrast agent [15]. The patients were imaged both before and after the injection of contrast material, which was 100 ml of intravenous iodixanol (Visipaque 320; GE Healthcare, Waukesja, WI, USA). Malignant lesions enhanced 55.9 Hounsfield Unit (HU) while benign lesions enhanced 17.6 HU. Thus malignant lesions were seen significantly better at contrast-enhanced dedicated bCT than at unenhanced dedicated bCT ($p < 0.001$), and it was also superior to mammography ($p < 0.001$). Microcalcifications were seen better at contrast-enhanced dedicated bCT than at unenhanced dedicated bCT ($p < 0.001$), and similar to mammography. These results suggested that contrast-enhanced dedicated bCT may aid in detection and even diagnosis of breast cancer.

Dedicated bCT is an emerging technology that has many advantages over current breast imaging systems. The “perfect” breast imaging approach is required to meet with the following demands: 1) full 3D capability, 2) good soft-tissue differentiation,

3) dynamic contrast-enhanced imaging, 4) high isotropic spatial resolution of 100 μm , 5) low patient dose with average glandular dose (AGD) below 5 mGy, 6) patient comfort without breast compression, 7) integrated biopsy option, and 8) low cost [11], and thus dedicated bCT is a good candidate. Full 3D capabilities are ensured by the principle of this imaging technique. Dedicated bCT also provides good soft-tissue differentiation and can offer accurate tissue density values, according to those previous clinical reports. It is also noted that contrast-enhanced dedicated bCT may be able to help assess contrast material enhancement kinetics [15]. The imaging cost is considerably more reasonable than MRI [12]. With these potentials, dedicated bCT is expected to play an important role in future screening.

Even though dedicated bCT is thought to be appealing, reading the 3D image volumes will be a very challenging task due to the large amount of image data generated. In a typical dedicated bCT image acquired in this study, there are often over 300 slices in the z-dimension displayed in the coronal plane. Sagittal and transverse planes might also need to be reviewed. Therefore computer-aided detection/diagnosis (CAD) technology, which has been successful in digital mammography, is expected to provide benefit mitigating the radiologists' interpreting task on dedicated bCT.

5. 3D Breast Ultrasound

Although mammography has proved to be an effective tool, there are still a number of cancers that may not be perceived. The rate of false-negative mammograms has been reported to be 4% to 34% [16]. In clinical experience, these mammographically-occult cancers are often 1) small in size and not associated with calcifications, 2) presenting in dense breast where visualization is difficult [16][17].

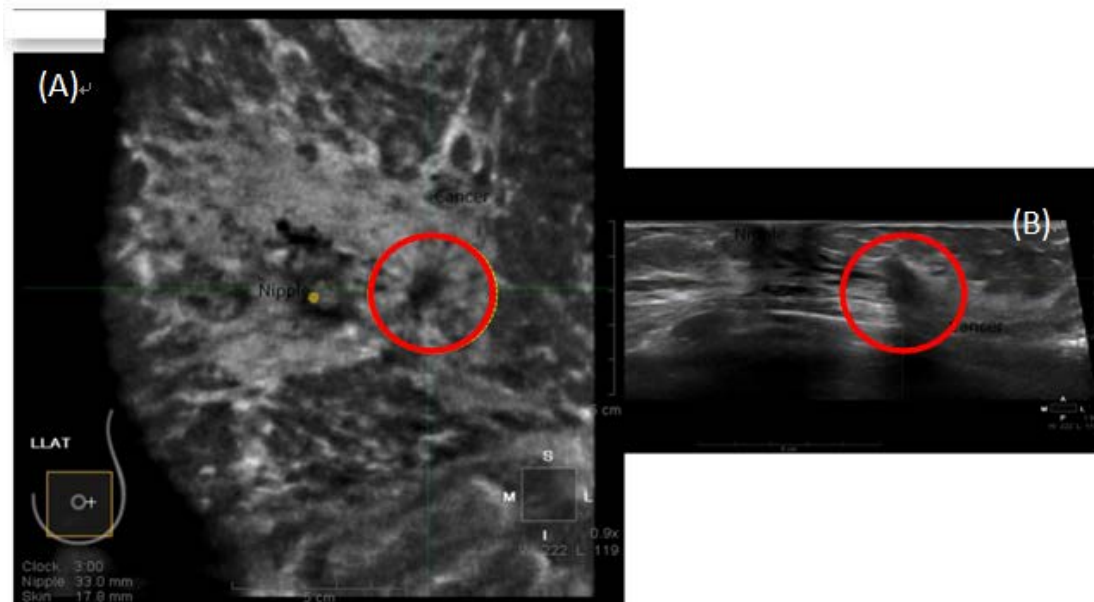


Figure 4. Example image of ABUS. (A) the coronal view of a left breast. The red dot is the nipple and the red circle indicates a cancer. (B) the cross section view as conventional handheld ultrasound. The red circle indicates the same cancer as indicated in (A).

Ultrasound (US), however, has been reported for its ability to depict occult cancers in mammography which are small and early-stage [18]. A clinical report also

showed that in dense breast US can detect smaller and lower-stage than mammographically-palpable cancers [18]. A number of studies have shown that by combining US with mammography, the detection of small size and lower stage cancers can be significantly increased by 7.4% than mammography alone, especially for dense breasts [19][20][21]. Thus, US has been recently indicated for use in breast cancer screening as an adjunct to screening mammography for women with dense breasts [22].

Nevertheless, US still has some disadvantages including operator-dependent handheld ultrasound in screening, long examination time, and the inability to acquire 3D volumetric images of the breast. Recently, researchers have used an automated scanning technique operated by technicians, generating 2D image sequences covering the entire breast [23]. This technique, called “automated 3D breast ultrasound (ABUS),” reconstructs 3D coronal breast ultrasound images providing not only transverse or sagittal views as conventional ultrasound images but also can displaying the coronal views of the breasts at different depths (Fig. 4).

Like dedicated bCT, interpreting 3D breast US can be very challenging. Not only because of large amount of image data that needs to be reviewed, the noise and

distortion resulting from having different spatial resolutions in three dimensions make the task even more difficult. Therefore, we expect CAD to also help alleviate the interpretation burden for 3D breast US. The 3D breast US images in this study were generated by an automatic breast ultrasound system which was developed by U-Systems, Inc. (Sunnyvale, CA). All data was anonymized and acquired under an IRB approved protocol.

B. Computer-Aided Detection/Diagnosis (CAD)

1. Introduction to CAD

In the mid 80s, a team at the University of Chicago started their research for computer-aided detection/diagnosis. The aim of their study was to use the computer output as an aid to radiologists, focusing on detection of lesions on chest radiographs and mammograms. In such usage, CAD is defined as “second opinion,” or a spellchecker in detecting lesions and making decisions [24]. Note that CAD’s role is not to replace the radiologist but instead to aid their image interpretation task. In the Joint FDA-MIPS Workshop on Methods for the Evaluation of Imaging and Computer-Assist Devices held on July 14, 2010, it was a consensus that the second-reader paradigm is the most appropriate way for using CAD systems in the clinic [25][26]. That is, the radiologist first reviews an image without CAD, then

immediately reviews the CAD output and finalizes the diagnosis. The schematic diagram is shown in Fig. 5.

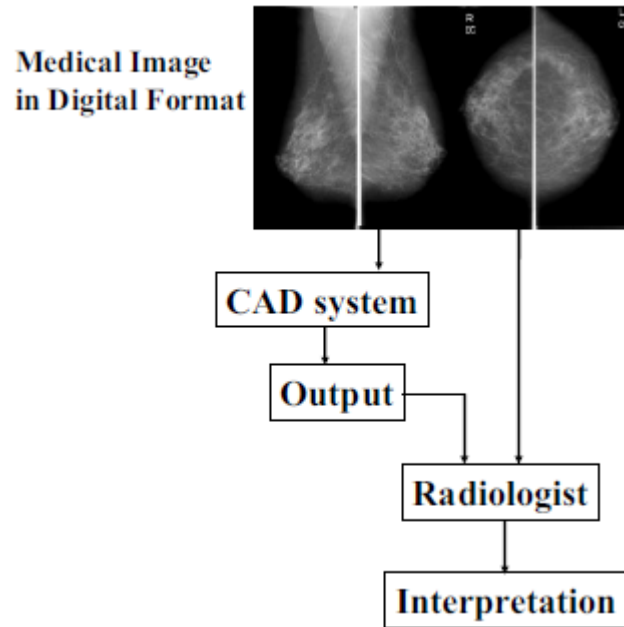


Figure 5. Schematic diagram of a CAD system for medical images interpretation. [24]

To understand images by digital computers is complicated. The process of a CAD system can be broken into various components as a step by step recipe. The flow chart of how CAD works is shown in Fig. 6. The first 4 boxes are considered part of computer aided detection, and the last 3 boxes are computer aided diagnosis.

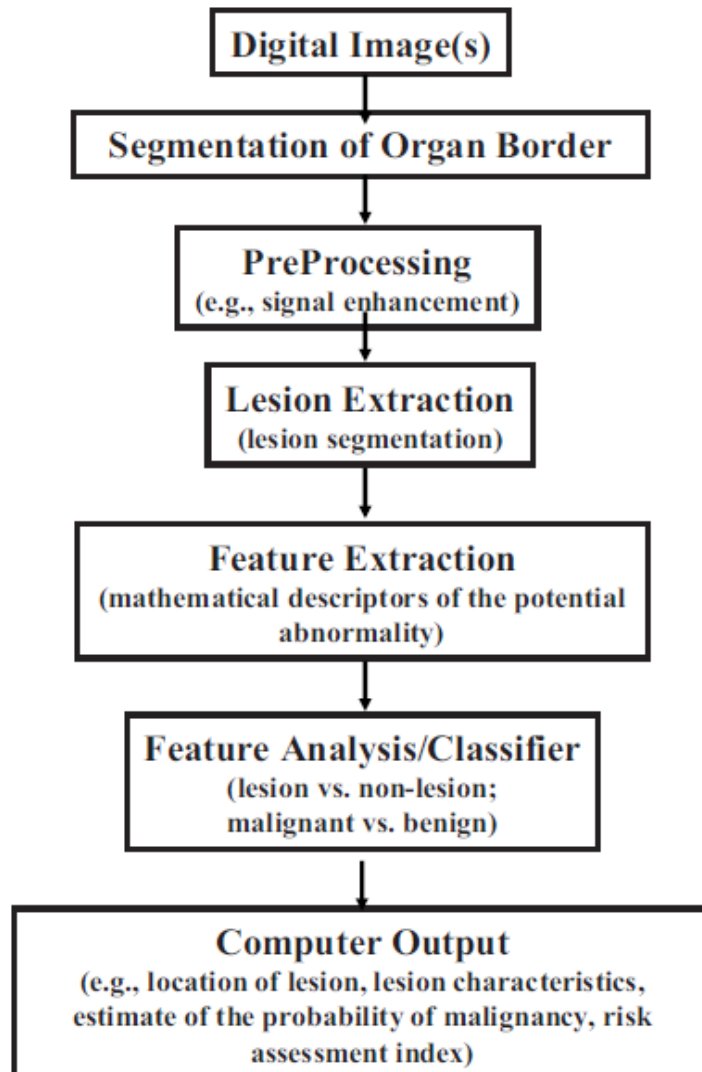


Figure 6. Components within a CAD system. [24]

a. Computer-Aided Detection (CADe)

In computer-aided detection, the computer output yields only the location of

suspect lesions. Although computer-aided detection does not output characterization and diagnosis of the abnormalities, such system is still useful for some clinical purpose, like screening mammography, low-dose thoracic CT for smokers, and colon cancer screening [24].

b. Computer-Aided Diagnosis (CADx)

Once a lesion is detected, further step of justifying subsequent patient management such as biopsy may be necessary. Computer-aided diagnosis aims to aid in the characterization of an already-found lesion in terms of its attributes, and in the estimation of disease state. The input to CADx system can be either a human-detected or a computer-detected lesion or region. Such a system is expected to aid in a radiologist's differential diagnosis and increase the positive predictive value of the image interpretation. Also it is expected to reduce variability between and within radiologists [24].

Computer-aided diagnosis generates output by dividing feature space into regions where normal and abnormal candidates are located with pattern recognition techniques. The features used for such classification task can be texture features based on image intensity, functional features such as contrast agent wash-out rate in MRI,

morphological features based on lesion size, shape, and anatomical properties. Among these features, morphological features highly rely on accurate segmentation. Only successful segmentation can lead to correct measure of morphological features. Thus, segmentation is an important step for computer aided diagnosis. In many cases, the performance of computer aided diagnosis reflects how accurate the segmentation step is.

2. CAD and Breast Cancer

There is a wide variety of CAD systems. In 1998, The US Food and Drug Administration (FDA) approved the first mammographic CAD device [26]. After then, more than a dozen of CAD systems have been approved including lung nodules on chest radiography and CT, colon polyps on CT colonography, and pulmonary emboli on chest CT [27]. By far the most widely used CAD systems are those for mammographic breast cancer screening. There are now about 10,000 CAD systems in use in the United States. Mammography CAD systems detect both masses and microcalcification clusters, and are doing well especially for the later. Clinical report suggests that computer-aided diagnosis can potentially help radiologists improve the diagnostic accuracy in breast cancer [28].

In a review paper, Cheng et al [29] outlined a flow chart of mammographic CAD procedure. The components are the same as shown in Fig. 11. They also listed and compared different approaches that have been used in mammographic CAD systems and studies for each component of the schematic flow chart.

In the image preprocessing step, commonly used techniques for enhancing image contrast include histogram equalization and local histogram equalization [30]. Other methods include enhancing digital mammograms with wavelet transform, highlighting edges by using Sobel filters, and removing noise with Gaussian filters [30].

In segmentation, many techniques have been investigated and developed. Global thresholding is a commonly used simple segmentation method based on histogram analysis [31]. Some researchers used local thresholding to refine the results of global thresholding [32]. Pixel based approaches include Markov random field (MRF) which seeks to maximize the posterior distribution of the given image [33], and a region growing algorithm that grows a set of seed pixels and aggregate pixels with similar properties [32]. Edge detection methods like Laplacian of Gaussian (LoG) filter and Difference of Gaussian (DoG) filter [30] are widely used. Aside from identifying

edges by applying operators, deformable model is another technique that has drawn much attention in medial image segmentation [34]. Initially proposed by Kass et al [35], the deformable model employs energy minimization to find the contour. Due to low contrast in mammography and lesion margin being vague, some studies presented fuzzy techniques to segment masses [36]. The algorithm initially assigns a fuzzy membership value to every pixel, and then an error value is calculated in each iteration until the error reaches zero, indicating that the optimized partition has been done.

The diagnostic stage of mammographic CAD contains feature extraction and classification as shown in Fig. 11. Features used in mammographic CAD includes intensity features, morphological features [37], and texture features [38]. To achieve better classification rate, feature selection is an essential step to select best feature combination for such goal. Step wise feature selection, which involves the analysis of the effect caused by removing one feature at a time from the feature pool, is a commonly used method [39]. Once the features are extracted and selected, the features are input into a classifier for differentiation. Some classifiers often seen in such task are 1) linear discriminant analysis (LDA) which classifies different categories by constructing a decision boundary in the feature space [40]; 2) artificial

neural networks which mimics biological nervous systems and uses many processing elements highly interconnected with weighted links to function as adaptive learning [40]; and 3) Bayesian network which uses probabilistic approach to divide a given database [41].

3. Future of CAD

Nowadays radiology is threatened by its own success: the number of images per study rise drastically; the workload of radiologists increases dramatically; the number of radiologists, however, is still limited; and health care costs related to imaging are fast increasing [27]. Therefore, a new way to handle such data explosion is needed. CAD might possess the key to solve the problem. Given that more new imaging modalities are generating 3D image volumes such as dedicated breast CT and automated 3D breast ultrasound, CAD holds the potential for speeding up the diagnostic process, reducing diagnostic errors, and improving quantitative analysis. With the continuing trend of growing computation power, CAD begins to be able to handle intensive computation and huge training data set. In some area like breast screening mammography, CAD is on a breakthrough and can even rival radiologists' performance. Although there are still some challenges that CAD development needs to overcome before it can widely sit in the reading rooms, such as limited image data

share for training software and insufficient readers for reader study [25][26], it is expected that CAD is likely to become a standard in medical imaging, more and more applications in the future.

C. Overview of Segmentation on Medical Images

As discussed in section B, segmentation is an important part both in CADE and CADx. Here we give an overview of commonly used segmentation methods on medical images.

1. Thresholding

The concept of thresholding is simple. Thresholding attempts to determine an intensity value which to be called a hreshold, and then uses the threshold to separate image pixels into different classes. This is often done by analyzing the histogram of a given image. The threshold is often identified at the valleys on a histogram. Although this method is simple and easy to be implemented, it can result in erroneous image partition if the image is noisy, or lacks of homogeneity within the object to be segmented. Due to medical images being often noisy and having vague boundaries for objects, segmentation on medical images with thresholding generally needs to be performed interactively [42] and thus becomes non-automatic.

For those more homogeneous images like brain MRI, some researchers have applied EM (expectation-maximization) algorithms to simulate an estimated gray-level distribution [43]. In this way, the valleys and peaks become clearer to be identified. Thus automatic segmentation with thresholding is more applicable.

2. Region Growing

Region growing is a technique for segmenting an image region that has similar predefined criteria. These criteria can be based on intensity and/or edge information. In this method, the input of seed point is required where the segmented region can start growing from. Like thresholding, region growing can be very sensitive to noise. To solve these problems, some additional algorithms have been developed to combine and refine region growing, such as fuzzy analogies [44]. Region growing is often used to delineate small and simple tumors [45].

3. Classifiers and Clustering

Classifiers methods seek to partition a feature space derived from the image by using data with known labels. This is a pattern recognition technique. A feature space is a space of any function of the image. In many cases, the feature space is often the

image intensities themselves. Classifiers are supervised methods because they need training data that are already labeled and then used as references for classifying incoming new data. Some commonly-used classifiers include k -nearest-neighbor classifier, Parzen window, and Bayes classifier [40].

Being noniterative, classifiers are more computationally efficient than region growing. In addition, they can be easily applied to multichannel images, which makes them superior to thresholding. However, the need of manual interaction to obtain training data is time consuming. The selection of training set can often lead to bias issues and result in errors.

In contrast with classifiers, clustering does not use training data and is termed an unsupervised method. Without training data, clustering iteratively modifies based on the change of properties of every class during each iteration. In sum, clustering uses available data to train itself. Three commonly used clustering algorithms are the K -means algorithm [40], the fuzzy c-means algorithm [46], and the EM algorithm [40]. Clustering methods have shown success in segmenting brain MRI [47].

4. Markov Random Field Models

Markov Random Field (MRF) model is not an actual segmentation model but more of a statistical method that can be incorporated into segmentation to obtain refined results. In principle, MRF analyzes the spatial interactions between neighboring or nearby pixels to evaluate local correlations. Therefore MRF methods are often incorporated into clustering methods, given that same cluster of pixels aggregate together and have high spatial correlations. This property is typically used in medical image segmentation since pixels from the same anatomical structure generally demonstrate similar intensity and are adjacent.

The difficulty in using MRF to aid in segmentation is the determination of parameters controlling the strength of spatial interactions. Also, MRF is usually computationally intensive. However, MRF has success in aiding correct segmentation on digital mammograms [33].

5. Artificial Neural Networks

Artificial neural networks (ANNs) use parallel networks of processing elements or nodes often called “perceptron” [30] to stimulate biological learning. Each perceptron performs elementary computations. With weighted links assigned to

connect different perceptrons, learning is achieved through the adaption of these links [30]. The most commonly used ANNs in medical image segmentation is as a classifier [48]. Due to that there are many interconnections in a neural network, spatial information can be easily incorporated into the classification process. However, the ordinary serial computer can reduce its computational advantage because ANNs are inherently parallel.

6. Deformable Models

Deformable model is a type of dynamic segmentation. Kass et al [35] first introduced such image segmentation technique in 1988. To segment an object in an image, a closed contour defined within an image domain is driven by the sum of external energy coming from image data and internal energy from the contour itself. The internal energy is designed to maintain the smoothness of the evolving contour during deformation. The external energy is defined to move the contour toward desired locations, such as object margins.

Although the theory of deformable first appeared in late 80's, there have been many modifications and improvements done in this field to make deformable models more applicable. Combining level set theory [49], deformable models nowadays can

naturally handle topologic changes, achieve good accuracy, and be implemented on the Cartesian coordinate system allowing for computation efficiency. Deformable models have become one of the most active and successful research fields in image segmentation. Because of its ability of handling complicated shapes, it is much favored in medical image application. Segmentation with deformable models on medical images can be widely seen on different image modalities on different organs, such MRI, CT, and ultrasound [50].

7. Other Approaches

Some other approaches used in medical image segmentation includes 1) atlas-guided approaches that could be a powerful tool when templates are available, like brain MRI; and 2) watershed algorithms that partitions an image into different homogeneous regions. However, watershed algorithm often suffers oversegmentation and thus post-processing steps for merging separate regions are usually required.

D. Hypothesis and Specific Aims

As described in the previous sections, medical imaging has come to a new era. The new imaging modalities which generate 3D images provide anatomical accuracy and could lead to improvement of image interpretation and diagnosis. However, it

also increases the amount of data that radiologists need to review. Such data explosion produces huge burden for radiologists. Furthermore, reviewing a 3D image volume on a 2D screen is difficult. One might need to construct the 3D structure in one's mind by reviewing many 2D slices. With the power of computation, CAD is expected to alleviate the burden by automatically detecting and even diagnosing suspicious areas embedded in the 3D image volumes.

Based on previous discussion, successful CAD relies much on accurate segmentation. Therefore, the purpose of this study is to develop breast mass segmentation technique that could be applied in dedicated bCT and 3D breast US. There are four specific aims in this study: (1) *Development of 3D lesion segmentation techniques for dedicated Breast CT*, (2) *Optimization of 3D lesion segmentation for Breast CT*, (3) *Task-based evaluation of lesion segmentation techniques*, (4) *Preliminary investigation of segmentation techniques on 3D breast ultrasound lesions*.

II. IMAGE DATABASE

The image database for this study contains contrast-enhanced bCT, non-enhanced bCT, and 3D breast ultrasound.

Contrast-enhanced and non-enhanced bCT images were acquired from University of California at Davis under an IRB approved protocol. The voxel dimension is equal in coronal plane ranging from 190 to 390 μm , and 200 to 700 μm in coronal slice spacing. Lesion centers were labeled by the radiologists, and lesion outlines were manually drawn in the coronal, sagittal, and axial planes by a research specialist with over 15 years of experience in mammography. Case numbers in the dedicated breast CT image database is listed in TABLE I.

TABLE I. IMAGE DATABASE OF DEDICATED BREAST CT

	Malignant	Benign	All cases
Contrast-Enhanced	25	13	38
Unenhanced	80	49	129

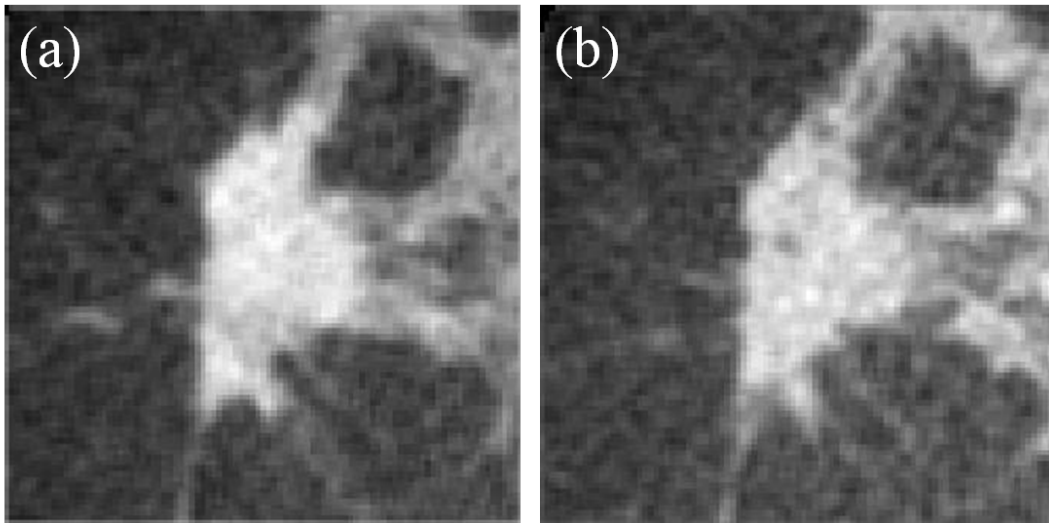


Figure 11. An example of dedicated breast CT image. (a) and (b) are the same coronal slice of the same lesion with and without contrast agent, respectively. Note that the breast lesion appears brighter in (a) than in (b). VOI size was $36 \times 35 \times 35.5$ mm.

The 3D breast US dataset includes 98 images containing different views on 64 cancers from 55 patients with breast density BI-RADS (Breast Imaging-Reporting and Data System) 3 or 4. They were imaged on an automatic breast ultrasound system (ABUS) developed by U-Systems, Inc. (Sunnyvale, CA). All data was acquired under an IRB approved protocol. Spatial resolution in the images was non-isotropic with spatial resolution in the axial plane of ~ 250 to $300 \mu\text{m}$ by $\sim 150 \mu\text{m}$ and slice spacing of $\sim 600 \mu\text{m}$. Lesion centers and margins were manually marked and outlined by an

expert breast radiologist with experience in breast ultrasound. Cancers in US images were divided into two groups: mammographically positive cancers and mammographically occult (TABLE II).

TABLE II. IMAGE DATABASE OF ABUS

Mammographically positive	Mammographically occult	All cases
44	54	98

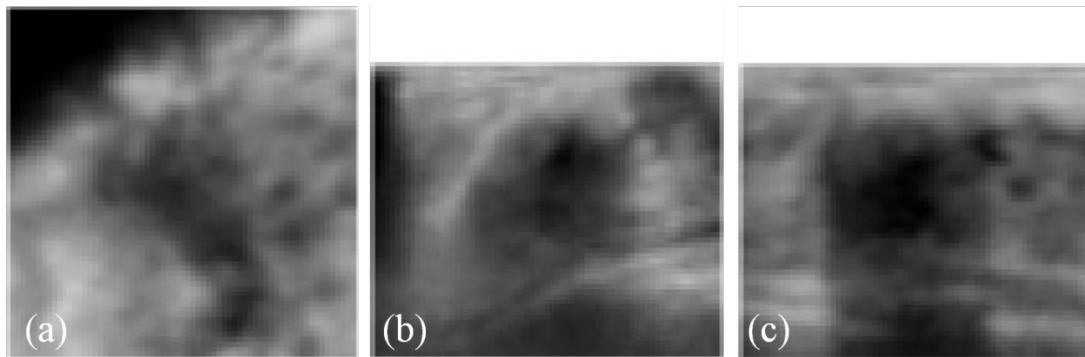


Figure 10. Example images of 3D breast ultrasound in the three central orthogonal planes. From (a) to (b): coronal, transverse, sagittal. The breast lesion appears dark region in the central area. Note that (b) and (c) demonstrate the depth (section) of the breast as conventional US does, and shadow is shown in the images as it appears under the lesion. In (b) and (c), and image size is larger than the depth of the breast, and the region out of the skin is cut out.

III. DEVELOPMENT OF 3D LESION SEGMENTATION FOR DEDICATED BREAST CT

The content of this chapter has been published on Proceedings of SPIE and e-published ahead of print on Journal of Digital Imaging.

- [68] **H. Kuo**, M. L. Giger, I. S. Reiser, J. M. Boone, K. K. Lindfors, K. Yang, and A. Edwards, "Evaluation of stopping criteria for level set segmentation of breast masses in contrast-enhanced dedicated breast CT," in *Proceedings of SPIE*, 2012, vol. 8315, pp. 83152C.
- [74] **H. Kuo**, M. L. Giger, I. Reiser, J. M. Boone, K. K. Lindfors, K. Yang, and A. Edwards, "Level Set Segmentation of Breast Masses in Contrast-Enhanced Dedicated Breast CT and Evaluation of Stopping Criteria," *J. Digit. Imaging*, vol. 27, pp. 237-247, 2014

A. Introduction

In an initial study, masses in bCT images were segmented using the radial gradient index (RGI) algorithm [51][52]. For 93% of the masses, the automated segmentation yielded an overlap ratio of 0.4 or greater. However, lesion segmentations tended to be undergrown and too spherical. Ray et al developed a semi-automated segmentation for masses in dedicated bCT based on the watershed algorithm [53][54]. Their method requires the user to input several markers to initialize the segmentation. The algorithm presented here requires only the lesion center as input, which is provided by a radiologist but could alternatively result from the output of a lesion detection (computer aided detection) algorithm. Other than Reiser et al's initial study [52], to the best of our

knowledge, this is the first algorithm for automated seeded lesion segmentation on dedicated bCT.

In a previous clinical report, Prionas et al found that lesion conspicuity was greater in contrast-enhanced bCT images than in unenhanced images due to higher HU for both malignant and benign lesions [15]. In a subset of our cases for which non-contrast bCT images were available, we found that the average lesion enhancement due to the contrast agent was 31.4 HU. Therefore, the lesion margin is expected to be better visualized in contrast-enhanced bCT images, and easier for the segmentation algorithm to capture. Hence we used contrast-enhanced dedicated bCT images to develop the segmentation algorithm. The strategy was to segment breast masses with a dual-stage segmentation procedure. The first stage of segmentation was done by RGI, which provided an initial contour for the second stage of segmentation -- active contour model.

Active contour (or “snake”) segmentation was originally proposed by Kass et al [35]. This model seeks an object margin that minimizes an energy functional consisting of internal energy and external energy along the deformable contour. Active contour segmentation has been used in medical imaging [55][56][57][58]. In breast

imaging, Brake et al used a discrete active contour method to segment mammographic mass lesions [59]. Sahiner et al incorporated edge and region analysis to help minimize the contour energy [60]. Both works express the contour as an N -points polygon, making the handling of topology changes difficult, as seen in split and merge segmentation methods. To solve this problem, Yuan et al [61] proposed a level set based approach [62][63][64] that can handle splitting and merging in a natural way for segmenting masses on mammogram. In this study, the level set approach was extended to 3D. This 3D level set based active contour model uses the initial contour generated by previously developed RGI and continues contour evolution until the desired lesion margin has been reached.

Contour leaking is a problem in lesion segmentation on medical images that needs to be addressed due to the presence of ambiguous margins. Therefore, a stopping criterion is required to terminate the iterative contour evolution process at the lesion margin. In this study, three stopping criteria were developed and compared: (1) the change of segmented region volume at each iteration, (2) the average intensity in the segmented region increase at every iteration, and (3) the rate of change of the average intensity inside and outside the segmented region [61].

B. Segmentation Methods

Figure 9 shows the flow chart of the proposed segmentation algorithm. The segmentation is performed in two stages: contour initialization with the RGI algorithm followed by a level set based active contour model.

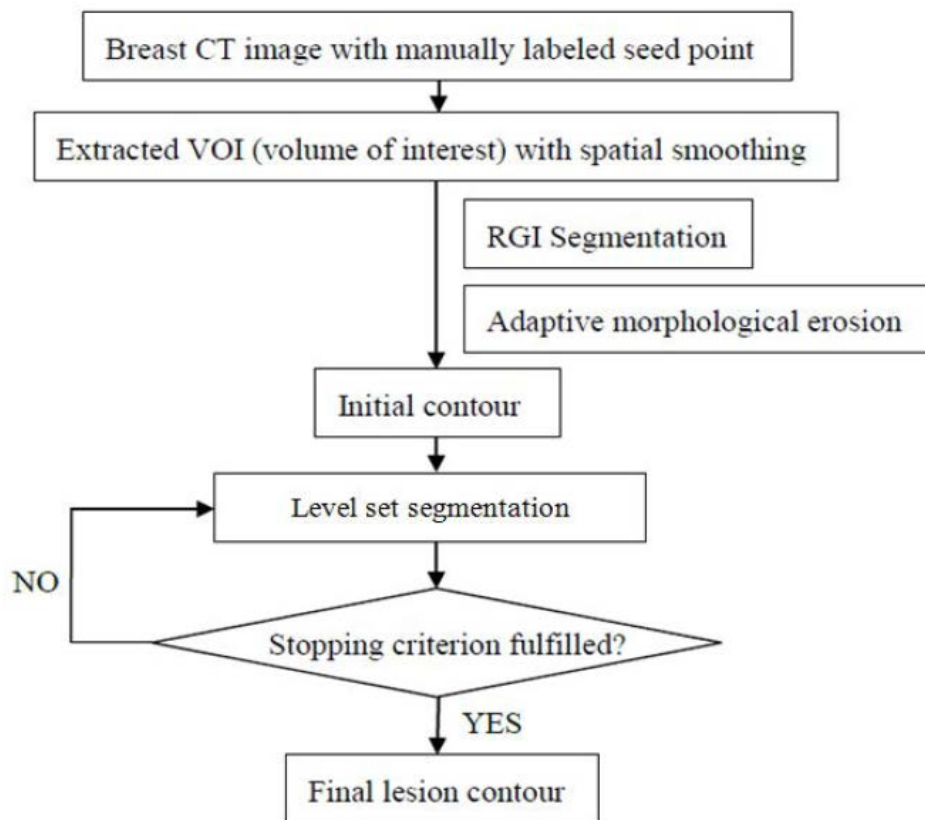


Figure 9. Schematic of the seeded breast CT lesion segmentation algorithm.

Although the level set based active contour algorithm can handle topologic changes in a natural way and is expected to be able to capture complicated

morphologic details, the way it minimizes the energy functional is complex and can result in errors on noisy and ambiguous images, such as medical images. Since breast lesions tend to exhibit local intensity variations, and lesions occur in a wide variety of sizes and shapes, it is not guaranteed that the active contour evolution equation always finds the global minimum that represents the optimized image partition. As a result, the evolving contour might become trapped in a local minimum of the energy functional. One way to guide contour evolution towards the global minimum is to initialize the active contour segmentation with an approximated lesion contour that is sufficiently enough to the true lesion margin to avoid local minima.

Based on a previous study [52], RGI can produce an approximate contour in a very short amount of time, with the limitation of the contours being too spherical and sometimes undergrown. While these limitations can produce unsatisfactory lesion outlines, they make the RGI algorithm well suited for contour initialization, which requires the contour to be entirely contained within the lesion. Thus, in the proposed segmentation algorithm, we used RGI segmentation to generate the initial approximate lesion outline, and used an active contour model to evolve the lesion contour towards the desired location and to capture morphologic details for greater segmentation accuracy.

Figure 10 shows the difference in segmentation results with and without use of a RGI-approximated initial lesion contour. As shown in Fig. 10, RGI segmentation not only increases the efficiency of the overall segmentation procedure, it also helps improve the accuracy for the second stage of segmentation.

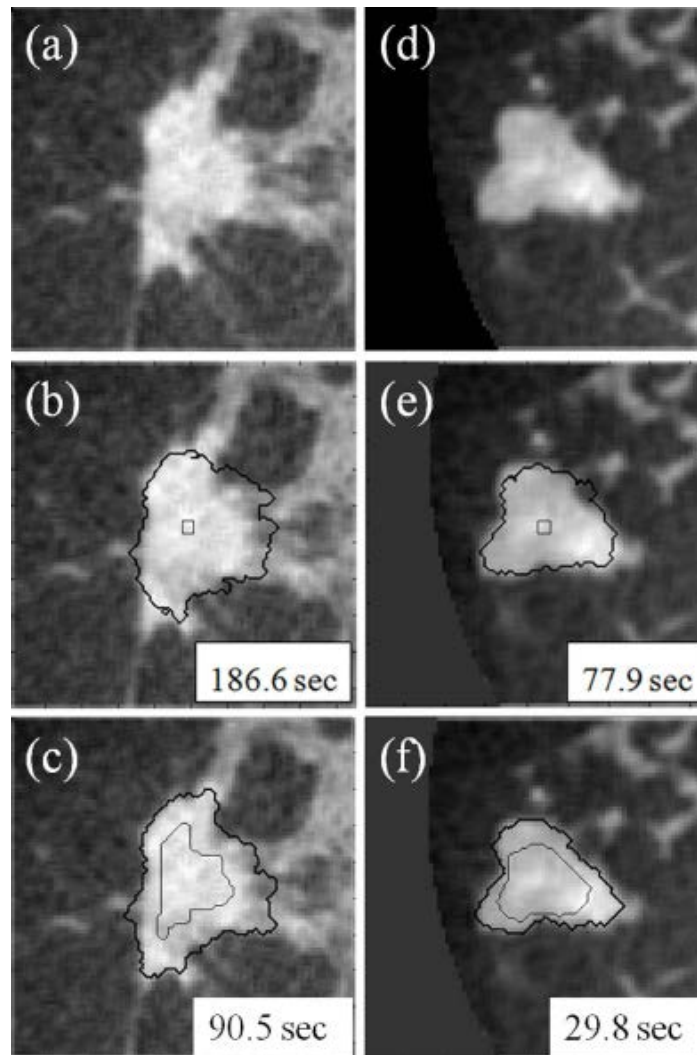


Figure 10. Comparison of active contour segmentation with different initial contours. (a) and (d): Coronal views of two dedicated breast CT lesions; (b) and (e): The initial contour was a cubic surface of 3^3 voxels; (c) and (f): The initial contour was, as included in our proposed overall segmentation method, an eroded RGI segmentation. Thin lines: initial contour; thick lines: final segmentation.

1. Contour Initialization

RGI segmentation is a seeded lesion segmentation technique [51]. Reiser et al extended it into 3D and showed that it can be applied on dedicated breast CT images [52]. For a given lesion contour $d\Omega$, the 3D RGI is given by

$$\text{RGI}_{3\text{D}} = \frac{\sum_{d\Omega} \vec{G}(x,y,z) \cdot \hat{r}(x,y,z)}{\sum_{d\Omega} |\vec{G}(x,y,z)|} \quad (\text{III.1})$$

where \vec{G} is the image gradient, and \hat{r} is a unit vector in the radial direction.

The volume of interest is multiplied by a 3D Gaussian constraint function, then a series of contours $d\Omega_i$ are generated by applying multiple gray-level thresholds to the constrained VOI. The resulting segmentation is the contour that maximizes RGI:

$$d\Omega_{\text{RGI}} = \arg \max_{d\Omega_i} \text{RGI}\{d\Omega_i\}, i=1, \dots, n \quad (\text{III.2})$$

In this algorithm, the standard deviation of the Gaussian constraint function was 10 mm, based on Reiser et al's study [52]. Further, to ensure that the initial contour is completely contained within the lesion before the second segmentation stage, morphological erosion is applied to shrink the RGI segmented lesion contour by using

the MATLAB function “imerode” with a cubic structuring element. The side length of the structuring element was one ninth of the cube root of the RGI segmented lesion volume. The resulting contour then served as the initial contour for the subsequent active contour segmentation. Figure 11 shows an example of a mass with a RGI segmented contour and the eroded contour, which is used to initialize the level set segmentation. Details about the active contour model are described in the following sections.

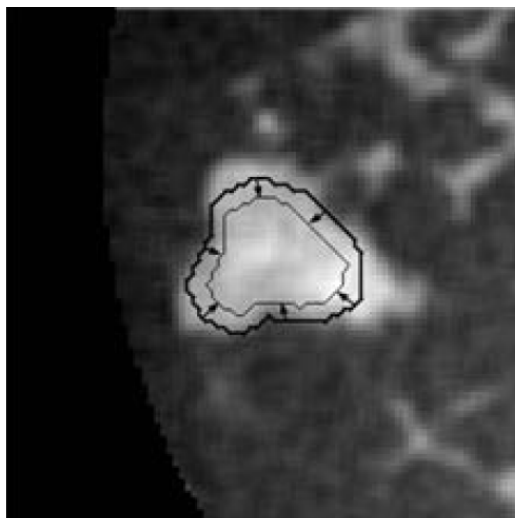


Figure 11. Demonstration of the RGI segmented contour (bold contour line) and the subsequently-eroded contour (thin contour line), which serves as the initial contour for input to the active contour segmentation stage.

2. Original Level Set Model

The level set based propagating fronts theory for delineating shapes on an image was introduced in 1988 [62]. The central idea of a level set method is to express the contour as the zero level set of a higher-dimensional function, the so-called level set function. The evolving contour is formulated through the evolution of the level set function; i.e. $d\Omega$ is the zero level set: $d\Omega = \{(x, y, z) \mid \varphi(\mathbf{x}, t) = 0\}$, $\varphi(\mathbf{x}, t)$ is the evolving level set function and t is the iteration. Let \mathbf{x} be a location vector $\in \mathbb{R}^3$ on the evolving hypersurface and $F(\mathbf{x})$ a speed function normal to the front at \mathbf{x} , and thus, the evolution equation for φ can be given as a basic formulation of a “Hamilton-Jacobi type” equation [62][63][64]:

$$\frac{\partial \varphi}{\partial t} + F|\nabla \varphi| = 0 \quad (\text{III.3})$$

In this classical level set front propagating equation, the level set function φ , however, can develop shocks, i.e., very sharp or flat shapes during evolution. Among different approaches to resolve this problem, Li et al proposed a regularization term given as [65]

$$\frac{\partial R(\varphi)}{\partial t} = \mu \left[\nabla^2 \varphi - \text{div} \left(\frac{\nabla \varphi}{|\nabla \varphi|} \right) \right] \quad (\text{III.4})$$

where $R(\varphi)$ is the regularization functional. The basic idea of this regularization term is to maintain the evolving level set function as a signed distance function with its intrinsic property $|\nabla\varphi| = 1$. This regularization term avoids contour re-initialization, which is computationally expensive [66][67].

Combining the Hamilton-Jacobi type equation (III.3) and the regularizing term (III.4) yields the level set evolution equation

$$\frac{\partial\varphi}{\partial t} = \varphi^{k+1} - \varphi^k = \tau \left\{ \mu \left[\nabla^2\varphi - \operatorname{div} \left(\frac{\nabla\varphi}{|\nabla\varphi|} \right) \right] + \nu g F |\nabla\varphi| \right\} \quad (\text{III.5})$$

where F is the speed function normal to \mathbf{x} ; ν is a scalar parameter that controls the direction of front propagation (negative value if evolving outward and positive if evolving inward); τ is the iteration step size; k is the iteration number; and g is the indicator function, given by

$$g = \frac{1}{1 + |\nabla G_\sigma \otimes I|^2} \quad (\text{III.6})$$

where G_σ is a Gaussian kernel and I is the image array. The indicator function was introduced by Castelles et al and is often seen in level set based curve evolution in

image processing and computer vision applications [63]. It incorporates geometrical information into the level-set function and ensures that the contour stops evolving in edge-like regions [63].

Since $|\nabla\phi| = 1$ is enforced by the regularizing term (i.e., the term in square brackets on the right hand side of III.5), the last, so-called fronts propagating term can be simplified as $v_g F$. In addition, by letting F be a delta function, the propagating front uniformly expands:

$$\delta_\varepsilon(x) = \begin{cases} 0, & |x| > \varepsilon \\ \frac{1}{2\varepsilon} \left[1 + \cos\left(\frac{\pi x}{\varepsilon}\right) \right], & |x| \leq \varepsilon \end{cases} \quad (\text{III.7})$$

where ε controls the sharpness of the delta function. Its value, $\varepsilon = 0.2$, was based on Li et al's settings [65].

For large lesions in our dataset, active contour segmentation could be very time consuming and therefore, the selection of τ had to be larger than 1000 to complete the segmentation task to reduce computation time for cases with large masses. For the purpose of stability, Li et al suggested that the product of τ and μ should be less than 0.25 [65]. To reach this, a small value of μ is often chosen which in turn

somewhat suppresses the effect of the regularization term. In this study, we found that the need of a large value of τ could yield undesired segmentation results even if $\tau\mu$ is less than 0.25 (Fig. 12(a) - 10(e)). This is because the strength of the regularization term, which is multiplied by τ , is comparatively larger than the fronts propagating term when it is significantly suppressed by g around the lesion margin. As a result, the regularization term can produce noise during contour evolution, cause erroneous termination, and might enable the contour to cross over the barrier set up by g , ultimately producing unsatisfying segmentation results. Figure 12(a) – 10(e) show segmentations obtained with $\tau = 1000$ and different values of μ .

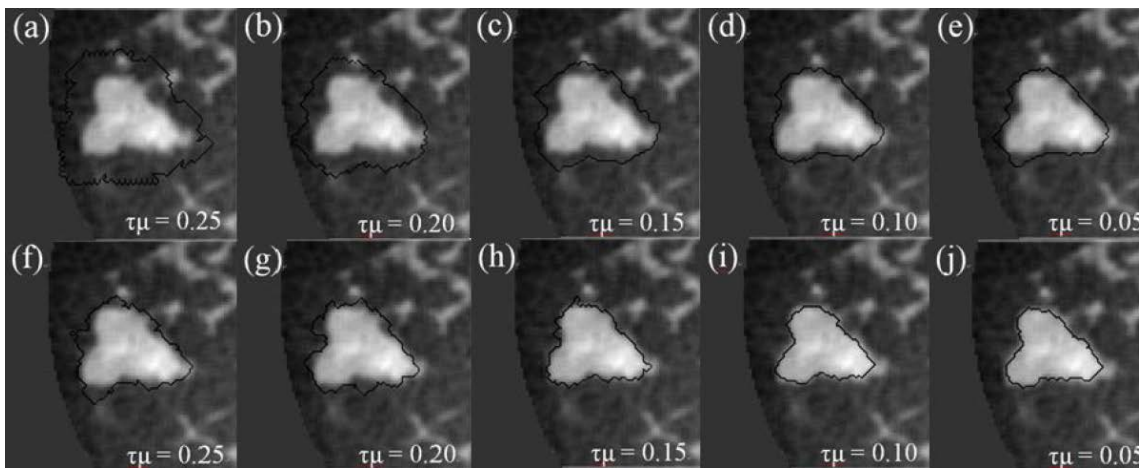


Figure 12. (a) to (e): Dedicated breast CT lesion segmentations obtained for different values of $\tau\mu$ using III. 5. (f) to (j): Dedicated breast CT lesion segmentations obtained for different values of $\tau\mu$ using III. 9. The coronal plane is shown. The stopping criterion was $\frac{d\bar{I}_L}{dt} - \frac{d\bar{I}_B}{dt} = 0$.

3. Proposed Level Set Model

Since the purpose of the regularization term is to maintain the signed distance function property only during the evolution process, the regularizing function becomes redundant when the evolving contour approaches the lesion margin where $\frac{\partial \phi}{\partial t} \rightarrow 0$. To solve this problem we propose to make the regularization term dynamic along with the contour evolution by incorporating the geometrical information into the regularization term using a “softened” indicator function g_s :

$$g_s = \frac{1}{1 + |\nabla G_\sigma \otimes \mathbf{I}|} \quad (\text{III.8})$$

Hence the level set evolution equation becomes

$$\frac{\partial \phi}{\partial t} = \phi^{k+1} - \phi^k = \tau \left\{ \mu g_s \left[\nabla^2 \phi - \text{div} \left(\frac{\nabla \phi}{|\nabla \phi|} \right) \right] + \nu g \delta_\epsilon(\phi) \right\} \quad (\text{III.9})$$

Note that compared to III.6, the power of $|\nabla G_\sigma \otimes \mathbf{I}|$ in the denominator of g_s is 1 rather than 2. From our experiments, we noticed that if g is used instead of g_s , the level set function can still produce subtle instability around the lesion margin because the regularization term is suppressed slightly too early. Fig. 12(f) - 10(j) show segmentation results from the new model that incorporates g_s , with $\tau = 1000$ and

different values of μ and for the same case as shown in Fig. 12(a) - 10(e). Here we suggest $\tau\mu < 0.15$ for 3D bCT images, because $\tau\mu > 0.15$ can still cause instabilities as shown in Fig. 12(f) and 10(g).

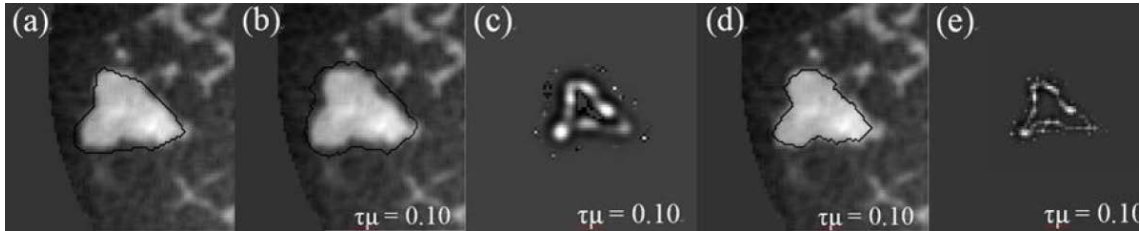


Figure 13. (a) Human-delineated lesion outline of the bCT lesion. (b) Segmentation result using Eq. 5. (c) Corresponding regularization map. (d) Segmentation result using III.9. (e) Corresponding regularization map. Examples are displayed in the coronal plane. Volume of interest size was $36\text{mm} \times 36\text{mm} \times 35.5\text{mm}$.

Figure 13 shows a comparison of the segmentation results from the model without and with the softened indicator function (Figs. 13(b) and 13(d)) and the corresponding human-delineated outline (Fig. 13(a)). In Fig. 13(d) the evolution stops automatically due to the stopping criterion, while the evolving contour shown in Fig. 13(b) has already crossed over the lesion margin at 60 iterations yielding poor segmentation performance. Figures 13(c) and 13(e) show the corresponding regularization term maps.

4. Stopping Criteria

In this study, we developed and compared three stopping criteria [68]:

1. The first stopping criterion is the minimum of $\Delta V/V$, and is based on the change of segmented region volume. Given the segmented volume V and the difference in region volume from the previous to the current iteration step ΔV , contour evolution is terminated when $\Delta V/V$ reaches a global minimum.

2. The second stopping criterion is the minimum of $d\bar{I}_{\Delta\Omega}/dt$, and is based on the average voxel intensity within the segmented region increase at each iteration. Here, \square denotes the segmented region and $\Delta\Omega = \Omega_{t+1} - \Omega_t$ is its increase in two consecutive iteration steps, and $\bar{I}_{\Delta\Omega}$ is the average voxel intensity in $\Delta\Omega$. When the contour approaches the lesion margin, $\bar{I}_{\Delta\Omega}$ is expected to decrease significantly. Therefore we select the 3D contour that corresponds to the global minimum of the derivative $d\bar{I}_{\Delta\Omega}/dt$ as the final lesion margin.

3. The third stopping criterion, $d\bar{I}_L/dt - d\bar{I}_B/dt = 0$, is based on comparing the rate of change (i.e., the slope) of the average voxel intensity as a function of iteration number inside and outside the segmented region, and was initially proposed by Yuan

et al [61]. Denoting the average voxel intensities inside the segmented region as \bar{I}_L , outside the segmentation as \bar{I}_B , and along the contour as $\bar{I}_{d\Omega}$, the difference of rates of change of average intensities inside and outside the segmented region are given as

$$\frac{d(\bar{I}_L)}{dt} - \frac{d(\bar{I}_B)}{dt} = \frac{1}{V_B} \cdot (\bar{I}_L - \bar{I}_B) \cdot [2 \cdot \bar{I}_{d\Omega} - 0.7(\bar{I}_L + \bar{I}_B)]^2 \quad (\text{III.10})$$

where V_B is the volume of the VOI excluding the segmented lesion and t refers to the iteration step. Note that parameters of this equation were adjusted for 3D bCT images. When the evolving contour crosses the lesion margin, the rate of change of the average intensity inside the segmented region increases, and will eventually match that outside the segmentation. Therefore the contour evolution is terminated when the rate difference, $[d\bar{I}_L/dt - d\bar{I}_B/dt]$, reaches zero. Since a numerical comparison against zero is difficult, for practical purposes, contour evolution was terminated when $[d\bar{I}_L/dt - d\bar{I}_B/dt]$ was less than 0.5.

5. Evaluation

Manual lesion outlines on 3 orthogonal planes, drawn by a research specialist in mammography, served as a reference for evaluating the segmentation algorithm.

Segmentation performance was assessed as the average overlap ratio (OR_{avg}),

computed as

$$\text{OR}_{\text{avg}} = \frac{1}{3} \left(\left(\frac{\Omega_{2\text{D}} \cap \omega_{\text{man}}}{\Omega_{2\text{D}} \cup \omega_{\text{man}}} \right)_{\text{cor}} + \left(\frac{\Omega_{2\text{D}} \cap \omega_{\text{man}}}{\Omega_{2\text{D}} \cup \omega_{\text{man}}} \right)_{\text{sag}} + \left(\frac{\Omega_{2\text{D}} \cap \omega_{\text{man}}}{\Omega_{2\text{D}} \cup \omega_{\text{man}}} \right)_{\text{ax}} \right) \quad (\text{III.11})$$

where $\Omega_{2\text{D}}$ is a cut through the 3D computer-segmentation that includes the lesion center, and (cor), (sag), and (ax) denote the orientation of the plane. ω_{man} is the human-delineated lesion outline in the same plane [52]. The computer outlines produced by the three stopping criteria were compared in terms of OR_{avg} , averaged over all cases. A *t*-test [69] was used to compare the performances across the three stopping criteria.

C. Results

Figure 14 shows examples of segmentation results by using the proposed active contour model with the three stopping criteria, for four masses. The leftmost column shows the manual outline of each mass. This figure also illustrates the variability of size, shape, and intensity variations within and in the neighborhood of breast masses imaged with 3D bCT.

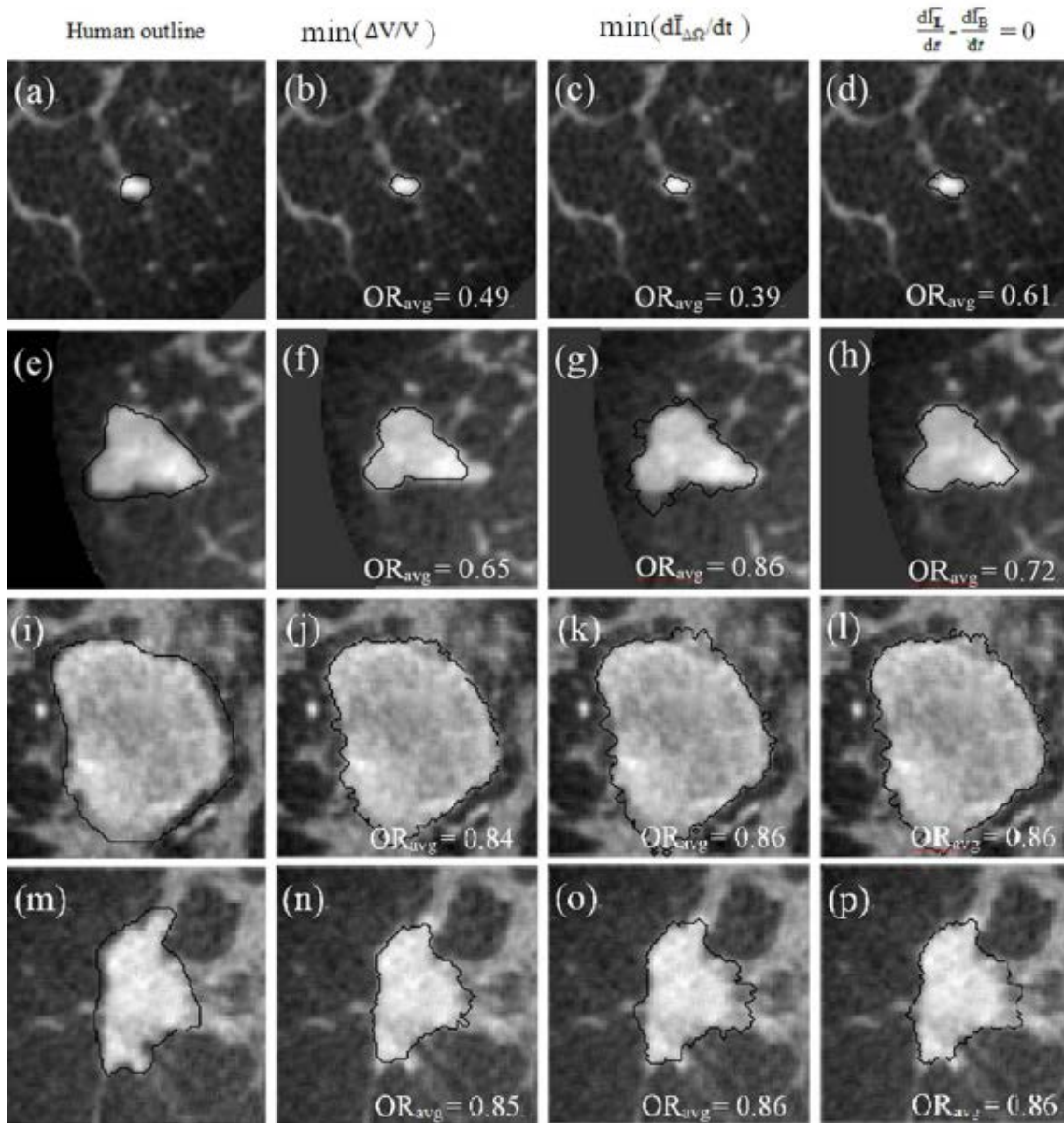


Figure 14. Segmentation examples for the three stopping criteria. $\tau\mu = 0.10$.

Figure 15 plots the proportion of correctly segmented masses, as a function of OR_{avg} threshold. For all three stopping criteria, OR_{avg} was greater than 0.4 for 96% of all masses. Overall, all stopping criteria produced similar curves, but for much of the range of OR_{avg} thresholds, the $\min(\Delta V/V)$ criterion resulted in a smaller proportion of correctly segmented masses, compared to the other two stopping criteria.

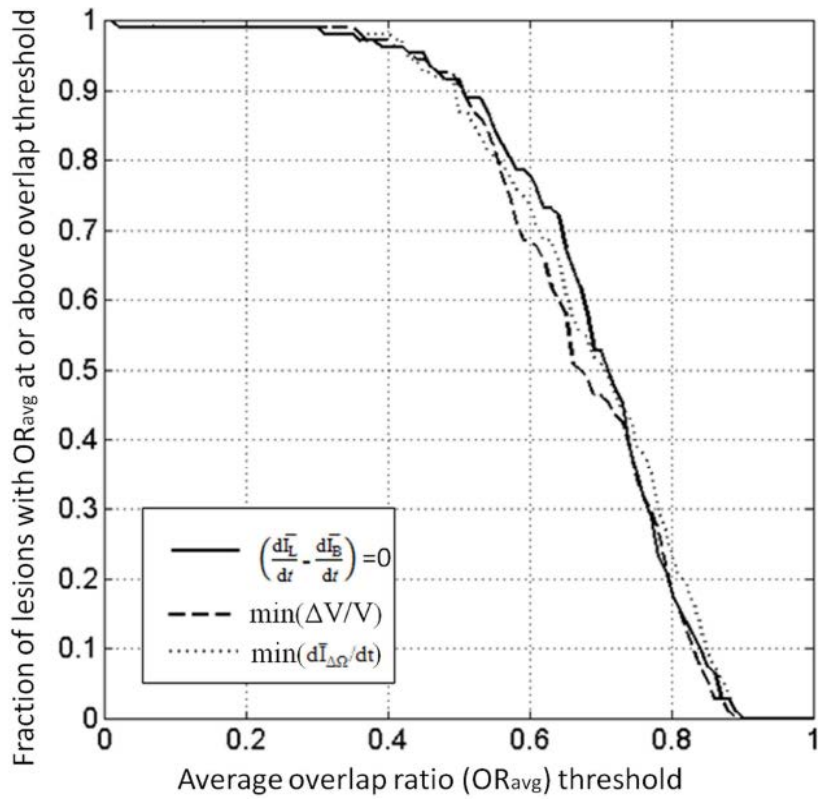


Figure 15. Segmentation performance as a function of OR_{ave} threshold, for the three stopping criteria.

TABLE III presents the performance of the proposed automated segmentation scheme for the three stopping criteria in terms of $\langle \text{OR}_{\text{avg}} \rangle$, where $\langle \cdot \rangle$ indicates average across all cases. For all stopping criteria, $\langle \text{OR}_{\text{avg}} \rangle$ was 0.66 or greater. The similarity of the lesion segmentations was assessed using a pairwise t -test. No statistically significant differences were found.

TABLE III. SEGMENTATION PERFORMANCE IN TERMS OF AVERAGE OVERLAP RATIO FOR THE THREE STOPPING CRITERIA AND COMPARISON RESULTS IN TERMS OF P -VALUES FROM THE T-TEST.

Stopping criterion	Average overlap ratio $\langle \text{OR}_{\text{avg}} \rangle$	p -values	
Minimum of $(\Delta V/V)$	0.66 ± 0.14	} 0.12 } 0.91 }	} 0.06
Minimum of $(d\bar{I}_{\Delta\Omega}/dt)$	0.68 ± 0.14		
$\frac{d\bar{I}_L}{dt} - \frac{d\bar{I}_B}{dt} = 0$	0.68 ± 0.14		

D. Discussion and Conclusion

Figures 12 and 13 demonstrate the effect of multiplying the regularization term with a “softened” indicator function (III.9), which not only ensures that $|\nabla\phi| = 1$ during contour evolution, but also prevents the regularization map from developing

undesired results when the driving force is being suppressed and the evolving contour approaches the stopping point (Fig. 13).

Overall, the proposed segmentation algorithm produces satisfactory lesion outlines for all stopping criteria in the sense that surrounding glandular tissues are not included in the segmented region (Fig. 14(i) - 12(l)). As shown in Figure 6, the active contour model evolves contours smoothly without generating shocks. The regularization term plays an important role in maintaining the stability. When $|\nabla\phi| > 1$, the regularization term $[\nabla^2\phi - \text{div}(\nabla\phi/|\nabla\phi|)]$ becomes positive and tends to allow for faster expansion of the evolving contour. If $|\nabla\phi| < 1$, then $[\nabla^2\phi - \text{div}(\nabla\phi/|\nabla\phi|)]$ becomes negative and the contour evolves more slowly, bringing ϕ back toward $|\nabla\phi| = 1$. This mechanism ensures that the level set function maintains its intrinsic property of a signed distance function during the evolution, $|\nabla\phi| = 1$, mitigating the need for re-initialization.

Of the three stopping criteria that were investigated, $\min(d\bar{I}_{\Delta\Omega}/dt)$ was found to be the least consistent. For small lesions, the average intensity within the grown region, $\bar{I}_{\Delta\Omega}$, is reduced substantially during early iterations due to the small size of the segmented region. This can cause contour evolution to be terminated prematurely, as

shown in Fig. 14(c). For larger lesions, on the other hand, the $\min(d\bar{I}_{\Delta\Omega}/dt)$ stopping criterion tended to be satisfied at a higher iteration number, compared to the other stopping criteria, producing slightly larger lesion segmentations. In turn, these resulted in a higher overlap ratio because the manual outlines were also drawn loosely, overestimating the lesion margin (see Figs. 14(g) and 14(e)). Thus, segmentations resulting in a higher overlap ratio were not necessarily closer to the lesion margin, judging by visual inspection. Furthermore, the “redundantly” grown parts (see protuberances in Fig. 14(g)) occurred because a large portion of background needed to be included in $\Delta\Omega$ to produce a global minimum in $d\bar{I}_{\Delta\Omega}/dt$.

Although contours from stopping criteria based on $\min(\Delta V/V)$ and $[d\bar{I}_L/dt - d\bar{I}_B/dt=0]$ generated similar overlap ratios, $\min(\Delta V/V)$ tended to produce tighter lesion outlines than the other two criteria. This can be seen in Table 1, in which $\min(\Delta V/V)$ produces the smallest average overlap ratio. Also, the p -values of comparisons between OR_{avg} from segmentations with the $\min(\Delta V/V)$ criterion and that using the other two stopping criteria might indicate such a trend as well.

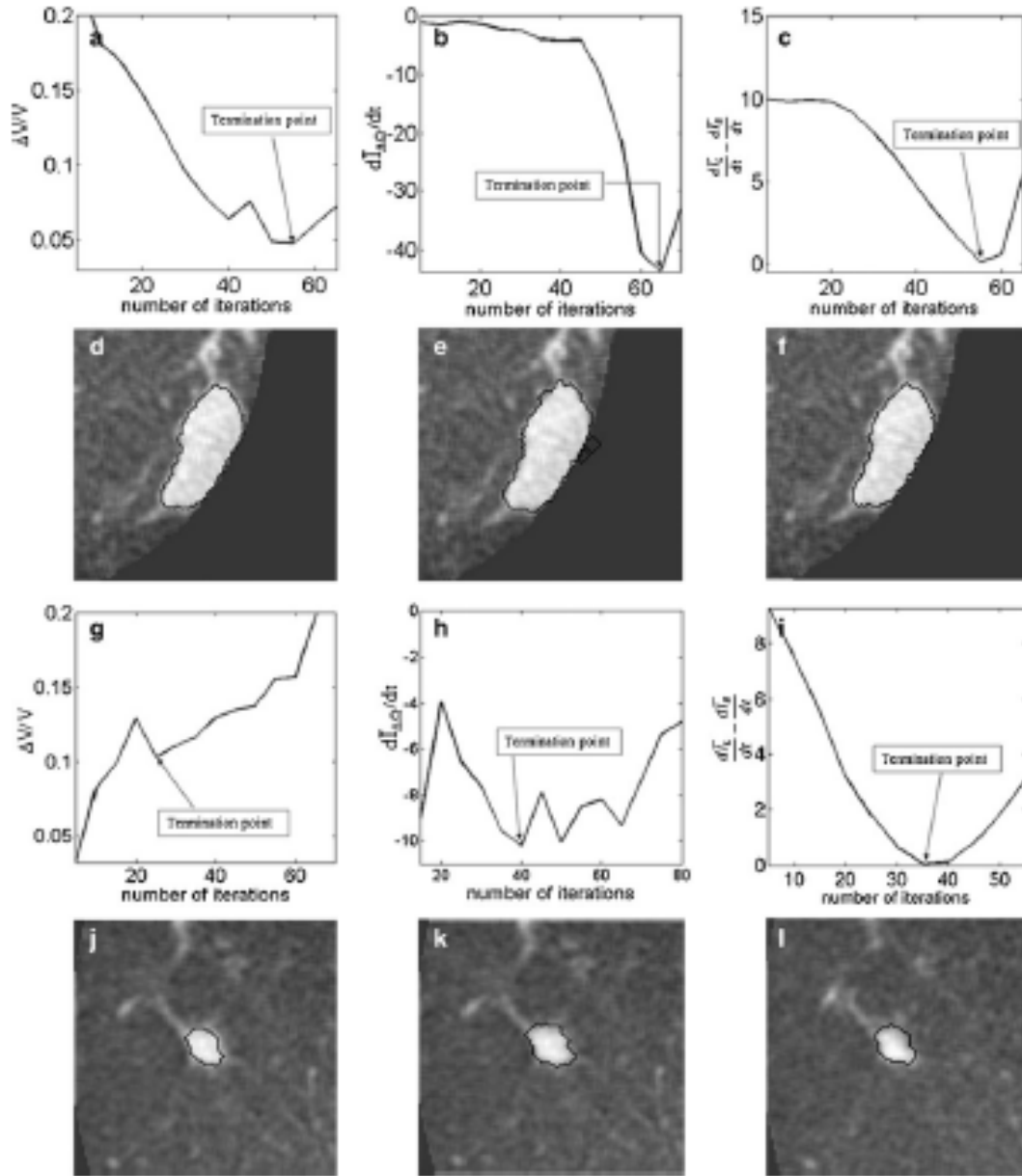


Figure 16. Stopping conditions as a function of iteration number, illustrated for two different masses (top two rows, bottom two rows). (a,g) $\Delta V/V$, (b,h) $d\bar{I}_{\Delta\Omega}/dt$, and (c,i) $\frac{d\bar{I}_L}{dt} - \frac{d\bar{I}_B}{dt}$. The segmentations corresponding to the termination point are shown (d,j), (e,k), and (f,l), respectively.

A drawback of the stopping criteria $\min(\Delta V/V)$ and $\min(d\bar{I}_{\Delta\Omega}/dt)$ is the need to let the contour evolve for many iterations past the actual stopping point in order to identify the minimum, as demonstrated in Figs. 16(a), 16(g) and 16(h). If the curve is noisy, curve fitting can help to determine a reliable minimum. As shown in Fig. 16(a), the segmentation will automatically cease at a local minimum if no curve fitting is used similar to what is seen for the stopping criterion $\min(d\bar{I}_{\Delta\Omega}/dt)$. Due to curve fluctuations, the global minima of $\Delta V/V$ and $d\bar{I}_{\Delta\Omega}/dt$ were selected after monitoring the contour evolution for many iterations beyond the actual stopping point (Fig. 16). In contrast, $[d\bar{I}_L/dt - d\bar{I}_B/dt]$ compares the average intensity inside the entire segmented region and the background and is therefore less sensitive to the intensity variations that might occur in a certain local region. As a result, $[d\bar{I}_L/dt - d\bar{I}_B/dt]$ is a monotonically decreasing curve that allows for easier identification of the stopping point (Fig. 16(c) and 16(i)).

Some researchers tend to use Dice coefficient (DICE) to evaluate the computer segmentation performance. DICE is defined as [70]:

$$\text{DICE} = \frac{2(\Omega \cap \omega_{\text{man}})}{\Omega + \omega_{\text{man}}} \quad (\text{III.12})$$

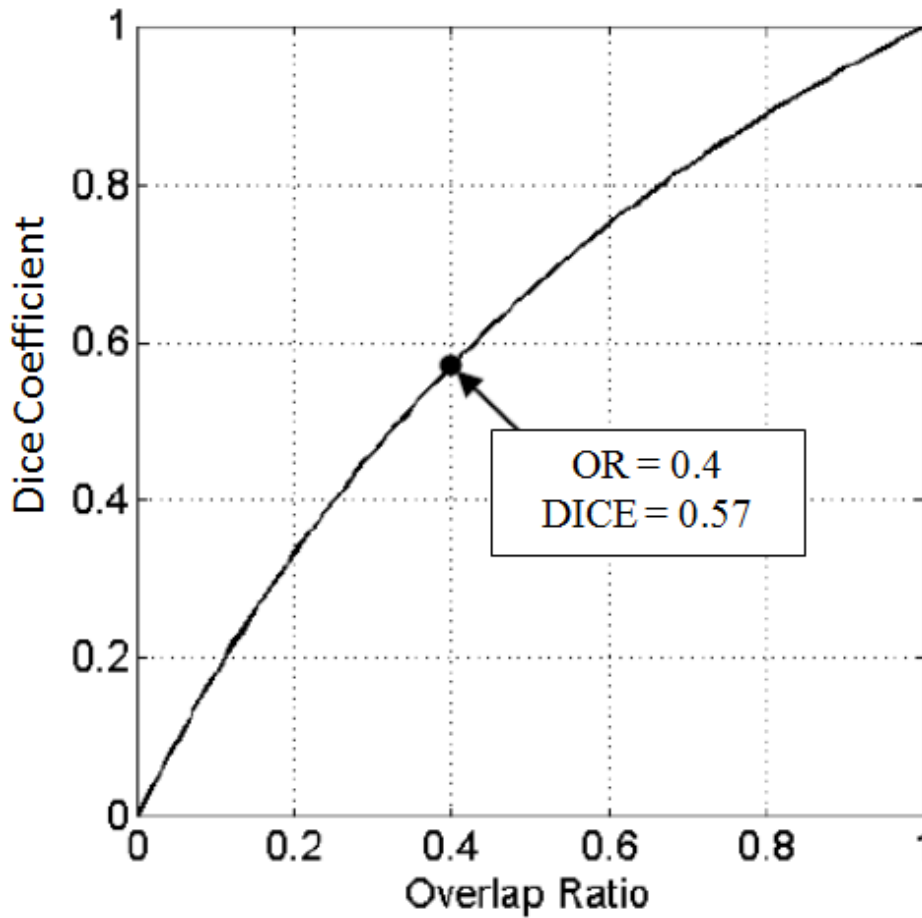


Figure 17. The relationship between OR and DICE.

where Ω is the computer-segmentation and ω_{man} is the human-delineated lesion outline. In terms of DICE, Zijdenbos et al suggested that a good overlap occurs when $\text{DICE} > 0.7$ in their literature of image validation [71]. Kuo et al showed the relationship between OR and DICE in their work of automated 3D breast ultrasound segmentation, and accordingly, an OR of 0.66 is equivalent to a DICE of 0.79 [72],

which is still well above 0.7. In fact, Sahiner et al compared classification of breast masses in mammography based on outlines by radiologists, and computer segmentations [60]. They found similar performance for an average overlap ratio of 0.62, which supports the use of overlap ratio to assess computer segmentations.

Limitations of this study are that the data set is small (33 patients; 38 contrast-enhanced masses). This might have affected the observed p -values when comparing OR_{ave} from the three stopping criteria. In a larger data set, one might expect to see smaller p -values for the comparisons of $\min(\Delta V/V) - [d\bar{I}_L/dt - d\bar{I}_B/dt = 0]$ and $\min(\Delta V/V) - \min(d\bar{I}_{\Delta\Omega}/dt)$ in a larger data set, since the results in Table I indicate such a trend. Further, manual outlines from one expert served as “ground truth” for the evaluation of the computer segmentation. Automated lesion segmentation is a central step in most CAD and quantitative analysis schemes and therefore, the segmentation performance ultimately needs to be evaluated in that context. However, as an intermediate step, lesion segmentation is often evaluated by comparing computer segmentations to human outlines, particularly in mammography [60][73].

To sum up, a two-stage 3D lesion segmentation method combining RGI

segmentation with an active contour model is developed. The RGI segmentation generates an approximate contour, which serves as initial contour for the subsequent contour evolution. The automated lesion segmentation algorithm was evaluated by computing the overlap ratio with manually drawn lesion outlines. Three stopping criteria were evaluated, which all yielded overlap ratios greater than 0.65 (corresponding to a Dice coefficient of 0.7). This suggests that the segmentation algorithm proposed in this paper can be successfully applied to masses imaged with contrast-enhanced dedicated breast CT. Among the stopping criteria that were investigated, $\min(d\bar{I}_{\Delta\Omega}/dt)$ was found to be the least consistent and the use of either $\min(\Delta V/V)$ or $[d(\bar{I}_L)/dt - d(\bar{I}_B)/dt = 0]$ is suggested, where the latter holds the advantage of not requiring curve fitting to identify the stopping point.

IV. APPLICATION OF THE PROPOSED SEGMENTATION MODEL ON UNENHANCED bCT IMAGES

The content of this chapter has been published on IWDM 2012.

- [75] H. Kuo, M. L. Giger, I. Reiser, J. M. Boone, K. K. Lindfors, K. Yang, and A. Edwards, "Level Set Breast Mass Segmentation in Contrast-Enhanced and Non-contrast-Enhanced Breast CT," in *11th International Workshop, IWDM, 2012*, vol. LNCS 7361, pp. 697-704

A. Introduction

In the previous chapter, we have shown that the segmentation method proposed in chapter III can be applied on contrast-enhanced dedicated bCT. However, unenhanced dedicated bCT would be more favored in future screening application because of no contrast agent injected into the patient body. Thus the purpose in this chapter is to test the applicability of the proposed segmentation procedure for unenhanced dedicated bCT.

B. Materials and Methods

The dataset included 23 contrast/non-contrast breast CT image pairs (13 malignant masses and 10 benign masses, see chapter II). The segmentation procedure is the same as described in chapter III, and the stopping criterion is $[d(\bar{I}_L)/dt - d(\bar{I}_B)/dt = 0]$.

C. Results

The average OR in contrast-enhanced bCT images was 0.69 (DICE = 0.82) while the average OR in unenhanced bCT images was 0.62 (DICE = 0.77). Figure 18 shows the cumulative overlap ratios for all lesions. Segmentation performance on contrast images is better than on non-contrast images in terms of their respective OR.

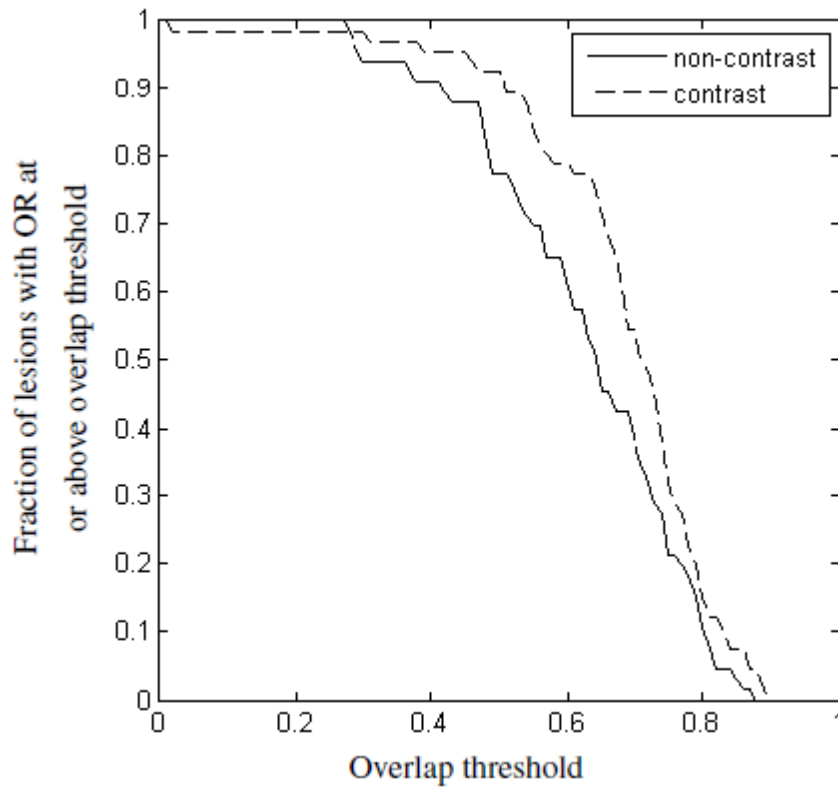


Figure 18. Comparison of segmentation performance between contrast and non-contrast images with radiologist's outlines.

Figure 19 shows the relationship between segmented lesion volumes in the non-contrast and contrast-enhanced bCT images. Each data point represents one lesion. Overall, lesion volume for both segmentations is similar except for two outliers. Examining segmentation results for the two outliers, which are circled in Fig. 18, revealed that segmentation in the unenhanced bCT images had failed. To assess the differences in lesion volume, a paired t -test was performed. Excluding these two failed segmentations, a p -value of 0.09 was found.

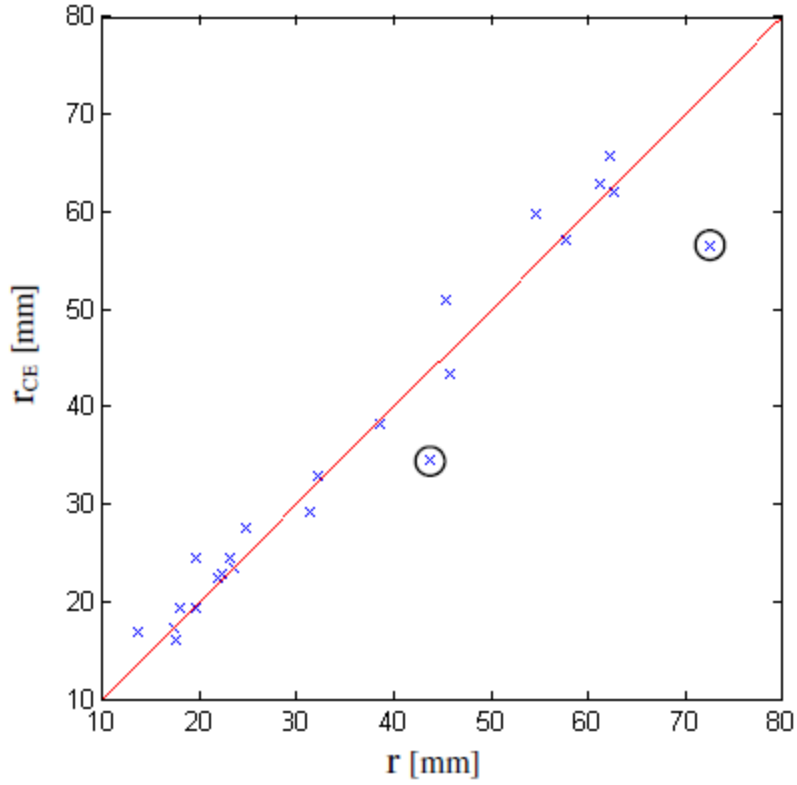


Figure 19. Comparison of lesion volume obtained from lesion segmentation in non-contrast or contrast-enhanced breast CT images. Plotted here is the radius of the equivalent sphere. The 2 circled data points represent failed segmentation cases on non-contrast images. $r_{CE} = \sqrt[3]{\frac{3V_{CE}}{4\pi}}$ and $r = \sqrt[3]{\frac{3V_{NCE}}{4\pi}}$. (V_{CE} : contrast-enhanced volume; V_{NCE} : non-contrast-enhanced volume)

D. Discussion and Conclusion

Shown in Fig. 20B and 20D, the overlap ratio of the human outlined regions is 0.99 (DICE \approx 1). When comparing with the computer segmentation, the OR_{avg} still differs: 0.7 (DICE = 0.82) for contrast and 0.6 (DICE = 0.75) for non-contrast. This

demonstrates that the proposed segmentation method might tend to stop evolving earlier without contrast agent because the lesion is less emphasized. Although the p -value of 0.09, yielded by t -test for contrast and non-contrast segmented volumes, might not be strongly significant, this still indicates the trend that segmentation in non-contrast bCT images tends to produce smaller lesion volumes than when segmenting the lesion in contrast-enhanced images.

Overall, the similar results of segmentation between contrast-enhanced and unenhanced bCT images demonstrate that our segmentation method can be applied on unenhanced images. However, this modified level set segmentation method might need some modification due to the tendency of segmenting smaller volume on unenhanced images. If the segmentation fails to segment the lesion completely, it will lose important shape details, which is a significant feature for classifying malignancy. Therefore, this examination suggests that the segmentation procedure proposed in chapter III needs a further improvement in order to be able to segment shape details as much as possible on unenhanced bCT images.

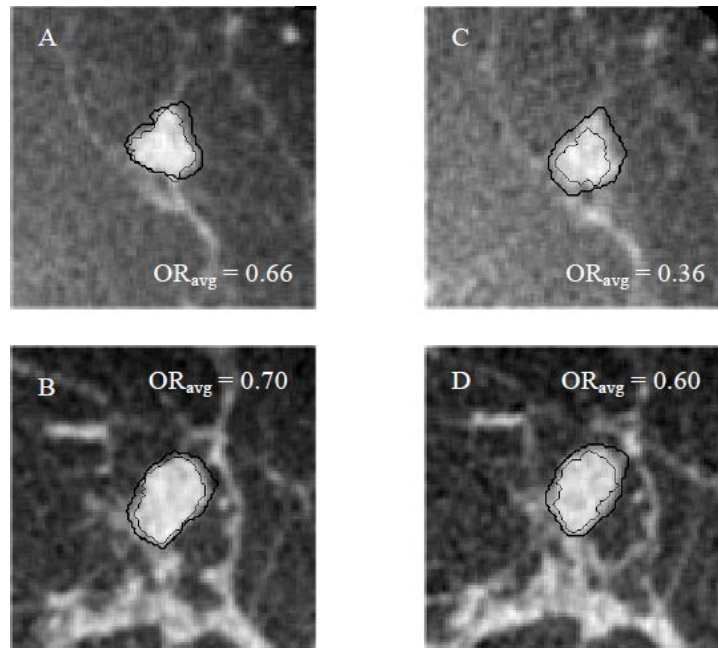


Figure 20. Examples of lesion segmentation in contrast-enhanced bCT images (A, B), and non-contrast-enhanced bCT images (C, D). Bold: human outline. Thin: computer-segmented outlines.

V. OPTIMIZATION OF THE SEGMENTATION MODEL

The content of this chapter has been accepted by Journal of Medical Imaging for publication.

A. Introduction

In chapter III, we present a two-stage 3D lesion segmentation model [74] which combines the radial-gradient index (RGI) [51][52] and the level-set based active contour algorithm [64][65]. This model yielded good segmentation performance of lesions in *contrast-enhanced* bCT images based on the overlap ratio between computer segmentation and human outline of 0.68, which is equivalent to a DICE value of 0.80. (Note that a value for the Dice coefficient larger than 0.7 has been suggested as indicative of a good overlap [71]). However, the resulting segmentations tended to segment lesion volumes smaller on *non-contrast* images compared to *contrast-enhanced* ones [75] as shown in chapter IV. Such conservative lesion outlines could miss important morphological margin indicators, such as spiculations, for diagnosis. Therefore, in this chapter, we address this problem on non-contrast-enhanced bCT images with optimization to our previous model.

The optimized segmentation model is still a two-stage method that uses a radial

gradient index segmentation method [51][52] to first delineate the initial contour of the lesion, and an modified active contour model to evolve the initial contour toward the lesion margins. As lesion margins are often ambiguous, we employed a dynamic stopping criterion [61] suggested in chapter III which is based on global information of the given image to terminate the segmentation procedure automatically. Moreover, we also evaluated the relationship between the amount of presenting breast fibroglandular tissues and the segmentation performance on bCT. This was conducted in order to investigate whether the proposed method would yield acceptable results when a lesion was surrounded by a large proportion of fibroglandular tissues, i.e., when a lesion was located in dense parenchyma.

B. Segmentation Methods

1. Contour Initialization

As introduced in chapter III, the initial contour was generated by using RGI-segmentation, which finds the lesion margin that maximizes the average proportion of gradients pointing radially outward from the lesion center [51][52]. In addition, to ensure that the initial approximation of the lesion contour was entirely inside the actual lesion, morphological erosion was performed with an adaptive cubic structuring element, that had a side length of $1/9$ of the cube root of the RGI

segmented lesion volume. We have found RGI segmentation combined with the erosion process to be a reliable and fast method to generate initial contours that serve as input to the active contour model in order to speed up and increase the robustness of the contour evolution. Details can be found in chapter III and Kuo *et al* [74].

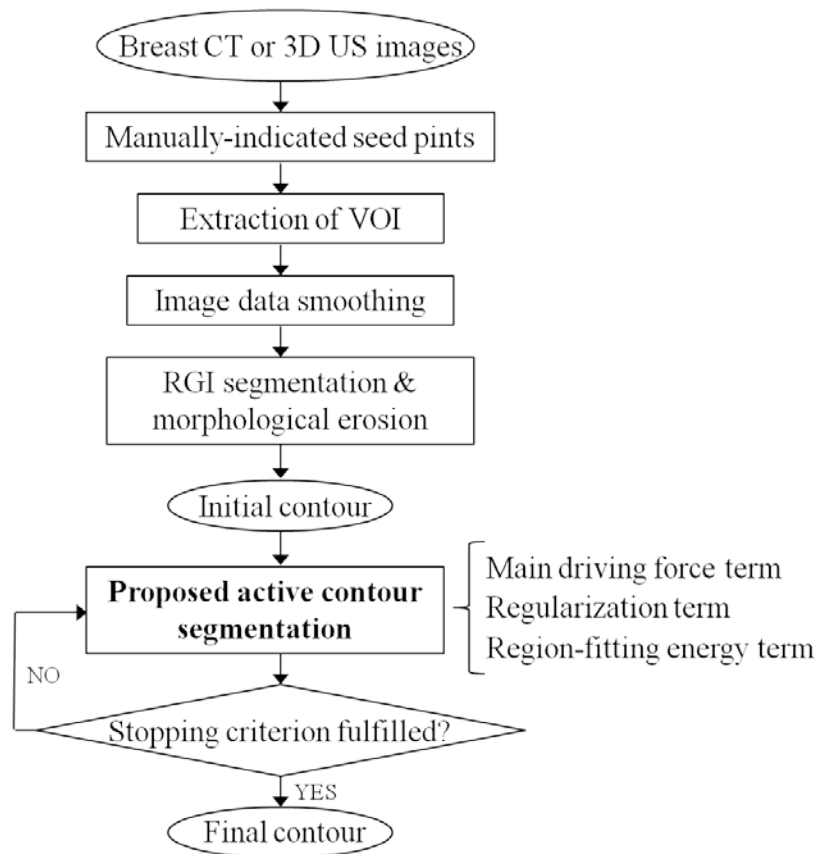


Figure 21. Flowchart of the optimized automated breast lesion segmentation Scheme.

2. Modified Active Contour Model with Local Energy Term

Active contour model (snake) was first proposed by Kass *et al* in 1988 [35]. The basic idea is to seek an object margin that minimizes an energy functional consisting of internal energy and external energy along the deformable contour. The internal energy controls the smoothness of the contour under the influence of the external energy, which attracts the contour to deform toward the object boundaries, e.g., the margin of a mass. The energy functional was calculated from a parameterized integral:

$$\varepsilon_{snake} = \int_0^1 \varepsilon_{internal}(\mathbf{r}(s)) ds + \int_0^1 \varepsilon_{external}(\mathbf{r}(s)) ds \quad (V.1)$$

where \mathbf{r} is the location vector on the evolving contour that $\mathbf{r}(s) = (x(s), y(s))$. This classical model, however, has difficulty handling topology changes of the contour [76], and the parameterization of the evolving contour also hinders implementation in 3D. In order to address topology problems, geometry-based level set active contour methods [62] have been used because they allow for region splitting and merging in a natural way. Moreover, they can be implemented on Cartesian grids, improving numerical computation efficiency. Since then, active contour algorithms with level set formulation have drawn much attention in image segmentation techniques. Malladi *et al* [64] and Caselles *et al* [63] proposed a level set based active contour model driven

by curvature-dependent speed functions, F , with an edge indicator g as a stopping function. Caselles *et al* [77] later proposed the geodesic active contour model with a level set formulation that merges the classical energy minimization concept with geometric level set active contour models. They showed that the level-set based contour evolution function can be derived from the contour energy functional by calculating the corresponding Euler-Lagrange equation.

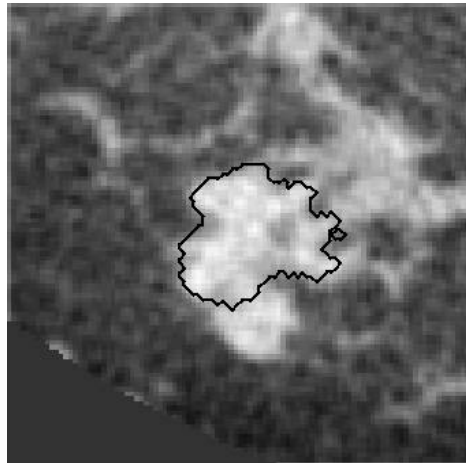


Figure 22. Shown in the figure is a contour generated by the proposed segmentation model in chapter III. This model can fail to segment lesions that are embedded in fibroglandular tissue, or lesions with a complex shape.

In chapter III, the proposed active contour model is purely a level-set based algorithm [74] modified from Malladi *et al* and Caselles *et al*'s approaches [64][63].

The results show that this model can yield satisfying segmentation performance on contrast-enhanced bCT when the lesions are highlighted and better visualized. However, it tends to segment smaller lesion contours on non-contrast bCT, as shown in chapter IV. In addition, malignant masses often have irregular shapes and present with vague lesion margins on breast CT (and other imaging modalities). The proposed model in chapter III tended to yield a coarse outline if a breast lesion lacked a clear margin (Fig. 22). In this chapter, we aim to solve this problem and capture more lesion shape details by introducing a region-fitting energy term [78], which was originally proposed by Li *et al.* We added the region-fitting energy term to the corresponding energy functional of the active contour model proposed in chapter III, and then calculated the associate Euler-Lagrange equation to derive the level-set based contour evolution function.

a. **Derivation of Level-Set Evolution Function from the New Energy**

Functional

The corresponding energy functional \mathcal{E}_{global} of the level set active contour model in chapter III is given as

$$\mathcal{E}_{global} = \int_{\phi} v g H(\phi) d\mathbf{r} + \mu g_s \cdot \frac{1}{2} \int_{\Omega} (|\nabla\phi| - 1)^2 d\mathbf{r} \quad (\text{V.2})$$

where ν and μ are parameters that controls the direction of evolving surface (negative for evolving outward and positive for inward) and the strength of the second term [74] in Eq. (V.1) (regularization term [65]), respectively; φ is the level set function such that the evolving surface $S = \{\mathbf{r} \mid \varphi(\mathbf{r}) = 0\}$; \mathbf{r} is the location vector (x,y,z) , H is the Heaviside function:

$$H(x) = \frac{1}{\pi} \arctan\left(\frac{x}{\alpha}\right) \quad (\text{V.3})$$

α is a parameter controlling the steepness of H . In Eq. (V.2), g is the edge indicator function proposed by Caselles *et al* [63] same as shown in Eq. (III.6). g_s the same as shown in Eq. (III.8). The first term in Eq. (V.2) is the main driving term that expands the surface uniformly. The second term in Eq. (V.2) is the regularization term first introduced by Li *et al* [65]. This term allows for expression of the evolving surface as a signed distance function without re-initialization, which is more efficient.

The new optimized contour energy functional is modified by adding a region-fitting energy term, as originally proposed by Li *et al* [78]. The region-fitting energy term is based on the approximated intensity inside and outside of the evolving surface in a local region. In general, the region-fitting energy functional seeks optimal

partitions of the lesion and background within the local region as determined by the size of a kernel mask, G_σ . The region fitting energy is defined as:

$$\mathcal{E}_{local} = \sum_{i=1}^2 \int G_\sigma(\mathbf{a}-\mathbf{r}) |I(\mathbf{r}) - f_i(\mathbf{a})|^2 M_i(\varphi(\mathbf{r})) d\mathbf{r} \quad (\text{V.4})$$

where G_σ is a Gaussian kernel with standard deviation σ , and \mathbf{a} is the location of the kernel center. M_1 and M_2 are defined as $(H(\varphi) + 0.5)$ and $(0.5 - H(\varphi))$, respectively, where H is the Heaviside function given in Eq. (V.3) and f_i are the approximated intensities inside and outside the local region. The energy functional \mathcal{E}_{snake} of the optimized active contour model is the sum of Eq. (V.2) and (V.4):

$$\mathcal{E}_{snake} = \mathcal{E}_{global} + \mathcal{E}_{local} \quad (\text{V.5})$$

Now we provide the derivation of the corresponding level set evolution function from Eq. (V.5). We start with the need to determine the level set function φ that minimizes the energy functional by $d\mathcal{E}_{snake}/d\varphi = 0$. For convenience, we denote the main driving term (the first term of right hand side of Eq. (V.2)) as A , the regularization term (the second term of right hand side of Eq. (V.2)) as B , and the region fitting energy term (right hand side of Eq. (V.4)) as C . To derive the corresponding level set evolution equation from Eq. (V.5), one needs to compute the

associated Euler-Lagrange equation using the first variation of calculus [79]. The minimum of Eq. (V.5) occurs when the following condition is satisfied:

$$\frac{d}{dx} \left(\frac{\partial(A+B+C)}{\partial \varphi_x} \right) + \frac{d}{dy} \left(\frac{\partial(A+B+C)}{\partial \varphi_y} \right) + \frac{d}{dz} \left(\frac{\partial(A+B+C)}{\partial \varphi_z} \right) - \frac{\partial(A+B+C)}{\partial \varphi} = 0. \quad (\text{V.6})$$

We address A , B , and C separately. For term A :

$$\begin{aligned} & \frac{d}{dx} \frac{\partial \text{vg}H(\varphi)}{\partial \varphi_x} + \frac{d}{dy} \frac{\partial \text{vg}H(\varphi)}{\partial \varphi_y} + \frac{d}{dz} \frac{\partial \text{vg}H(\varphi)}{\partial \varphi_z} - \frac{\partial \text{vg}H(\varphi)}{\partial \varphi} \\ & = \text{vg}H'(\varphi) = \text{vg}\delta(\varphi) \end{aligned} \quad (\text{V.7})$$

where δ is the derivative of H with respect to φ :

$$\delta = \frac{1}{\pi} \cdot \frac{\alpha}{\alpha^2 + x^2}. \quad (\text{V.8})$$

For term B :

$$\frac{\partial \mu g_s \left(\frac{1}{2} (|\nabla \varphi| - 1)^2 \right)}{\partial \varphi} = 0, \quad (\text{V.9})$$

$$\frac{d}{dx} \frac{\partial \mu g_s \left(\frac{1}{2} (|\nabla \phi| - 1)^2 \right)}{\partial \phi_x} = \mu g_s \frac{d}{dx} \left(\phi_x - \frac{\phi_x}{\|\nabla \phi\|} \right), \quad (\text{V.10})$$

and similarly using partial differentiation with respect to ϕ_y and ϕ_z . Combining together, we have

$$\begin{aligned} \mu g_s \left[\frac{d}{dx} \left(\phi_x - \frac{\phi_x}{\|\nabla \phi\|} \right) + \frac{d}{dy} \left(\phi_y - \frac{\phi_y}{\|\nabla \phi\|} \right) + \frac{d}{dz} \left(\phi_z - \frac{\phi_z}{\|\nabla \phi\|} \right) \right] \\ = \mu g_s \left(\nabla^2 \phi - \text{div} \left(\frac{\nabla \phi}{|\nabla \phi|} \right) \right) \end{aligned} \quad (\text{V.11})$$

For term C , we employ the steepest descent method [80] to derive the associated Euler-Lagrange equation. By fixing the approximated intensity $f_1(\mathbf{a})$ and $f_2(\mathbf{a})$, the minimum of the region fitting energy term C occurs when

$$-\delta_{\alpha}(\phi)(a_1 - a_2) = 0 \quad (\text{V.12})$$

where

$$a_i = \int G_{\sigma_2}(\mathbf{a} - \mathbf{r}) |I(\mathbf{r}) - f_i(\mathbf{a})|^2 d\mathbf{r}, \quad i=1,2. \quad (\text{V.13})$$

Using steepest descent method and assembling Eq. (V.7), Eq. (V.11), and Eq. (V.13),

we reach the level set formulation of the contour evolution function Eq. (V.14) with an added iteration step constant τ on the first two terms:

$$\begin{aligned} \frac{\partial \varphi}{\partial t} = \varphi^{k+1} - \varphi^k = \tau \left\{ \nu g \delta_\alpha(\varphi) + \mu g_s \left(\nabla^2 \varphi - \operatorname{div} \left(\frac{\nabla \varphi}{|\nabla \varphi|} \right) \right) \right\} \\ - \delta_\alpha(\varphi) \left(\int G_\sigma(\mathbf{a}-\mathbf{r}) |I(\mathbf{r}) - f_1(\mathbf{a})|^2 d\mathbf{r} - \int G_\sigma(\mathbf{a}-\mathbf{r}) |I(\mathbf{r}) - f_2(\mathbf{a})|^2 d\mathbf{r} \right). \end{aligned} \quad (\text{V.14})$$

where k refers to iterations. Now we give the derivation of the approximated intensities a_1 and a_2 . It is also obtained by using the steepest descent method to minimize the region fitting energy functional with the level set function φ fixed. Given this condition, one can find the minimum of the energy functional C with respect to $f_1(\mathbf{a})$ and $f_2(\mathbf{a})$ when the following satisfies:

$$\int G_{\sigma_2}(\mathbf{r}-\mathbf{a}) M_i(\varphi(\mathbf{r})) |I(\mathbf{r}) - f_i(\mathbf{a})| d\mathbf{r} = 0, \quad i=1, 2., \quad (\text{V.15})$$

From (Eq. (V.15)), we can obtain $f_i(\mathbf{a})$ as:

$$f_i(\mathbf{a}) = \frac{G_{\sigma_2}(\mathbf{a}) \otimes (M_i(\varphi(\mathbf{r})) I(\mathbf{r}))}{G_{\sigma_2}(\mathbf{a}) \otimes M_i(\varphi(\mathbf{r}))}, \quad i=1, 2. \quad (\text{V.16})$$

Throughout the remainder of this paper, we will refer to Eq. (V.2) as ‘the model

proposed in chapter III' and Eq. (V.5) as 'the optimized model.' The parameter settings are as follow: $\tau = 1000$, $\nu = -10$, $\mu = 0.001$, $\alpha = 0.2$, maximum number of iterations = 300. The parameter settings are listed in TABLE IV.

TABLE IV. OPTIMIZED ACTIVE CONTOUR MODEL PARAMETER VALUES FOR SEGMENTATION OF BCT LESIONS.

	τ	ν	μ	α	Maximum number of iterations
bCT	1000	-10	0.001	0.2	300

b. Dynamic Stopping Criterion

As mentioned in the previous chapters, lesion margins are often ambiguous in medical images, it is necessary to use a stopping criterion for the active contour model. In this chapter, we adopted the dynamic stopping criterion proposed by Yuan *et al* [61], which is defined as $(d\bar{I}_L/dt - d\bar{I}_B/dt) = 0$. For details, please refer to section III.B.4.

3. Segmentation Evaluation

a. Segmentation Performance in terms of DICE

The computer-segmented margins were evaluated on three orthogonal slices through the lesion center in comparison to the manually-delineated lesions. Segmentation performance was presented in terms of the Dice coefficient (DICE), an overlap measure between the manually-delineated margins and computer-segmented margins on the three orthogonal slices (Eq. (V.17))

$$\text{DICE} = \frac{1}{3} \left(\left(\frac{2(\Omega \cap \omega_{\text{man}})}{\Omega + \omega_{\text{man}}} \right)_{xy} + \left(\frac{2(\Omega \cap \omega_{\text{man}})}{\Omega + \omega_{\text{man}}} \right)_{yz} + \left(\frac{2(\Omega \cap \omega_{\text{man}})}{\Omega + \omega_{\text{man}}} \right)_{xz} \right) \quad (\text{V.17})$$

where Ω is the computer-segmentation and (xy) , (yz) , (xz) denote the orientations of each slice through the lesion center. ω_{man} is the human-delineated lesion margin in the same orthogonal slice. Note that the DICE value for a given lesion is the average of the DICE values over the 3 orthogonal planes. According to Zijdenbos *et al* [71], a Dice coefficient ≥ 0.7 indicates ‘good’ overlap between computer and human outlines for medical images.

We compared segmentation performance between the model Eq. (V.2) and the optimized model Eq. (V.5) by assessing using paired *t*-tests of Dice coefficients.

b. Segmentation Performance and Presenting Fibroglandular Tissue

on bCT

Since fibroglandular tissue has an x-ray attenuation coefficient similar to that of tumor tissue, the presence of fibroglandular tissue adjacent to a lesion poses challenges for segmentation. To investigate the dependence of lesion segmentation quality on the presence of fibroglandular tissue in the immediate vicinity of lesions, we used a fuzzy c-means-based segmentation scheme to identify fibroglandular tissue [81]. The proportion of fibroglandular tissue in a lesion's vicinity was calculated from a 50 mm \times 50 mm square region on each of the three central slices on which the manual lesion delineations were performed, and was defined as the area of the fibroglandular tissue (as identified by the fuzzy c-means method) relative to the area of the 3 slices excluding the manually-outlined lesion area. Based on the work of Yaffe *et al* [82], 95% of women have breast density of lower than 45% when imaged with bCT, with mean glandular fraction of 19.3%. Therefore we used 20% and 40% as thresholds to divide our database into three 'local fibro-density classes': $\leq 20\%$ as the lower local density, 20% \sim 40% as medium local density, and $\geq 40\%$ as extremely high local density.

C. Results

1. Impact of the New Modification to the Active Contour Method: An

Example

In this study, a new term \mathcal{E}_{local} (Eq. (V.4)) was added to the original active contour model. To illustrate the impact of this term, Fig. 23 shows both contrast-enhanced and non-contrast breast CT images, manual delineations, and computer-determined segmentations (using the original model (Eq. (V.2)) and the optimized model (Eq. (V.5))) of a lesion with a complicated shape.

For this example, the DICE values of the original model were satisfactory, but improved by including the new term \mathcal{E}_{local} in the segmentation model for both contrast and non-contrast images. As this example illustrates, the proposed segmentation method was able to capture more shape detail.

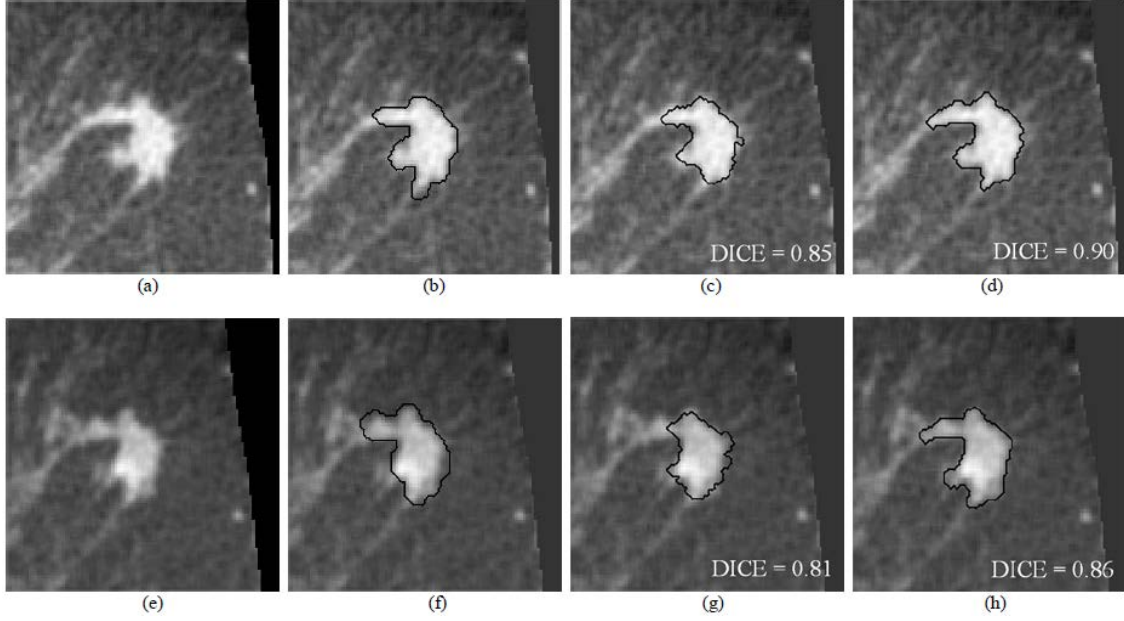


Figure 23. (a)-(d): non-contrast-enhanced images. (e)-(h): contrast-enhanced images. (b) and (f): research specialist’s outlines. (c) and (g) segmentations by our previous model (d) and (h): segmentations by the proposed model. Note that these eight images are of the same patient (case), and they are displayed in the central coronal plane through the lesion seed point. For this case, the proportion of fibroglandular tissue in the lesion neighborhood is 12%.

2. Comparison of Original and Optimized Segmentation Models

We compared the optimized segmentation model, Eq. (V.5), to the original model, Eq. (V.2) (TABLE V). For the non-contrast bCT images, the optimized segmentation model obtained significantly better segmentation with respect to our previous model, ($p \ll 0.05$) for both malignant and benign lesions (TABLE V). It appeared to slightly improve the performance for contrast bCT but this improvement failed to reach statistical significance ($p = 0.30$). Figure 24 show the fraction of lesions correctly

segmented at various overlap (Dice coefficient) thresholds in bCT with several segmentation examples shown in Fig. 26, 27.

TABLE V. SEGMENTATION RESULTS FOR CONTRAST-ENHANCED AND NON-CONTRAST-ENHANCED BREAST CT

	Segmentation Model	Performance in DICE (mean \pm std)	Percentage of ≥ 0.7 DICE	<i>p</i> -value of paired <i>t</i> -test between the two models
Contrast-enhanced bCT	Benign cases (<i>N</i> = 13)	Original Model 0.81 \pm 0.07	93%	0.24
		Optimized Model 0.84 \pm 0.09	93%	
	Malignant cases (<i>N</i> = 25)	Original Model 0.80 \pm 0.11	88%	0.65
		Optimized Model 0.81 \pm 0.08	92%	
Total cases (<i>N</i> = 38)	Original Model 0.80 \pm 0.10	90%	0.30	
	Optimized Model 0.82 \pm 0.10	93%		
Non-contrast bCT	Benign cases (<i>N</i> = 49)	Original Model 0.80 \pm 0.10	89%	0.005
		Optimized Model 0.83 \pm 0.08	96%	
	Malignant cases (<i>N</i> = 80)	Original Model 0.76 \pm 0.10	73%	0.04
		Optimized Model 0.78 \pm 0.12	85%	
Total cases (<i>N</i> = 129)	Original Model 0.77 \pm 0.10	79%	0.0016	
	Optimized Model 0.80 \pm 0.11	89%		

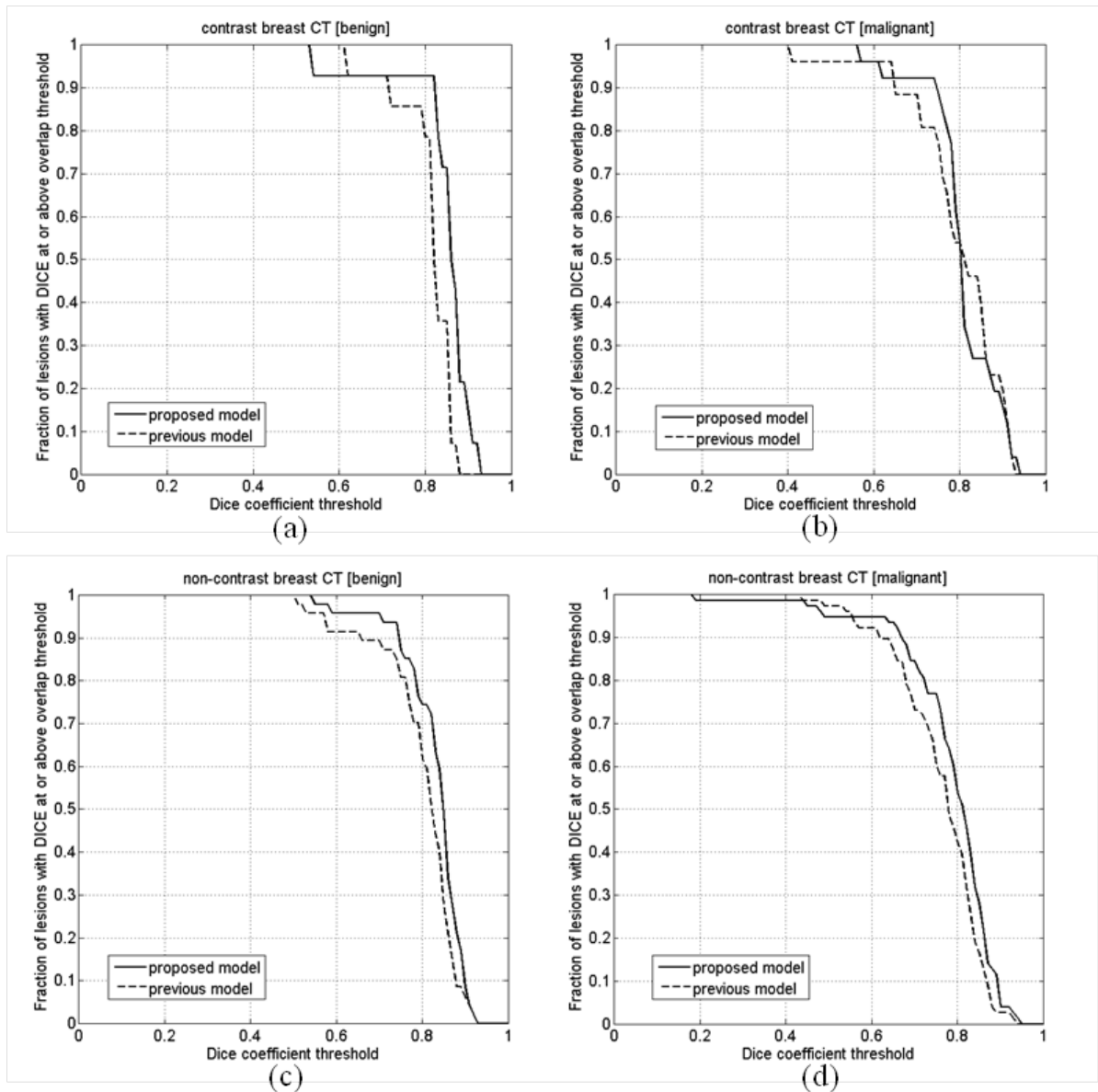


Figure 24. (a) is the comparison of segmentation between the proposed and previous segmentation methods on contrast bCT images benign dataset ($N = 13$). (b) is the comparison of segmentation between proposed segmentation and previous segmentation contrast bCT images malignant dataset ($N = 25$). (c) is the comparison of segmentation between proposed segmentation and previous segmentation on non-contrast bCT images benign dataset ($N = 49$). (d) is the comparison of segmentation between proposed segmentation and previous segmentation on non-contrast bCT images malignant dataset ($N = 80$).

3. Segmentation Performance and Presenting Fibroglandular Tissue

The relationship between segmentation performance and the proportion of fibroglandular tissue in the lesion vicinity on bCT images is shown in Fig. 25 and TABLE VI. For non-contrast bCT, the segmentation performance decreases when the proportion of fibroglandular tissue exceeds 40%, but the DICE is still above 0.7. Segmentation examples for different ‘local fibro-density classes’ are shown in Fig. 26.

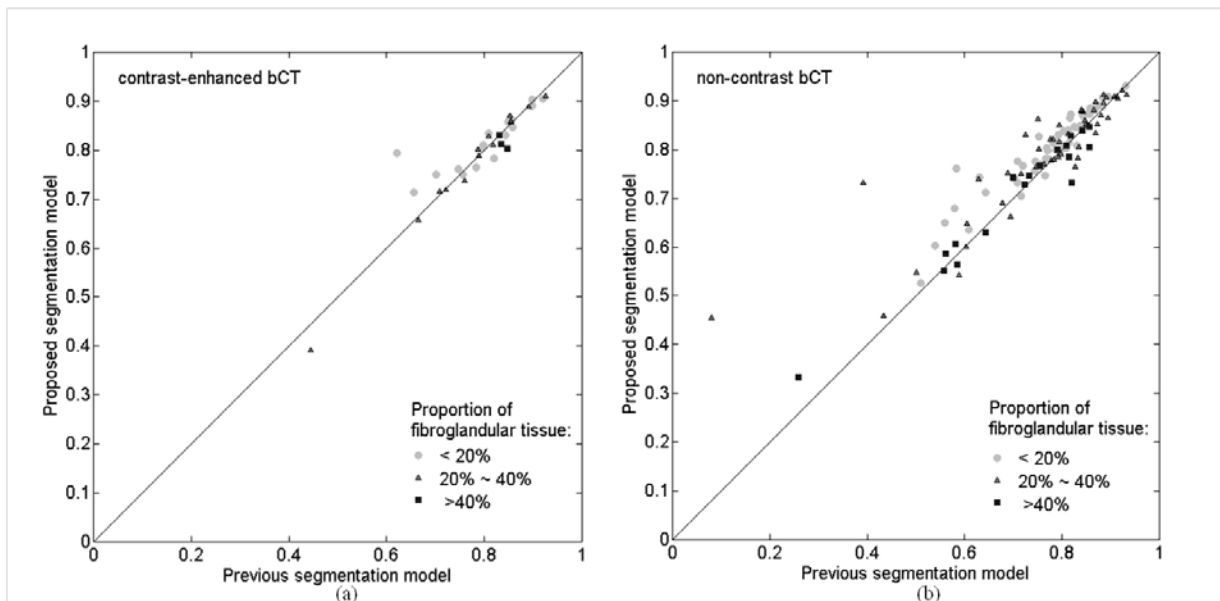


Figure 25. Comparison of lesion DICE coefficients for the original and optimized segmentation models.

TABLE VI. SEGMENTATION PERFORMANCE WITH DIFFERENT FIBROGLANDULAR CATEGORIES ON BCT

Proportion of fibroglandular tissue in lesion neighborhood		< 20%		20% ~ 40%		> 40%	
		DICE \pm std	Paired <i>t</i> -test <i>p</i> -value	DICE \pm std	Paired <i>t</i> -test <i>p</i> -value	DICE \pm std	Paired <i>t</i> -test <i>p</i> -value
Contrast-enhanced bCT	Original model	0.81 \pm 0.08	0.15	0.78 \pm 0.12	0.57	0.84 \pm 0.01	0.23
	Optimized model	0.82 \pm 0.06	(<i>N</i> = 20)	0.77 \pm 0.13	(<i>N</i> = 15)	0.82 \pm 0.01	(<i>N</i> = 3)
Non-contrast bCT	Original model	0.77 \pm 0.09	\ll 0.05	0.77 \pm 0.16	0.01	0.71 \pm 0.15	0.98
	Optimized model	0.80 \pm 0.08	(<i>N</i> = 56)	0.79 \pm 0.12	(<i>N</i> = 55)	0.71 \pm 0.14	(<i>N</i> = 18)

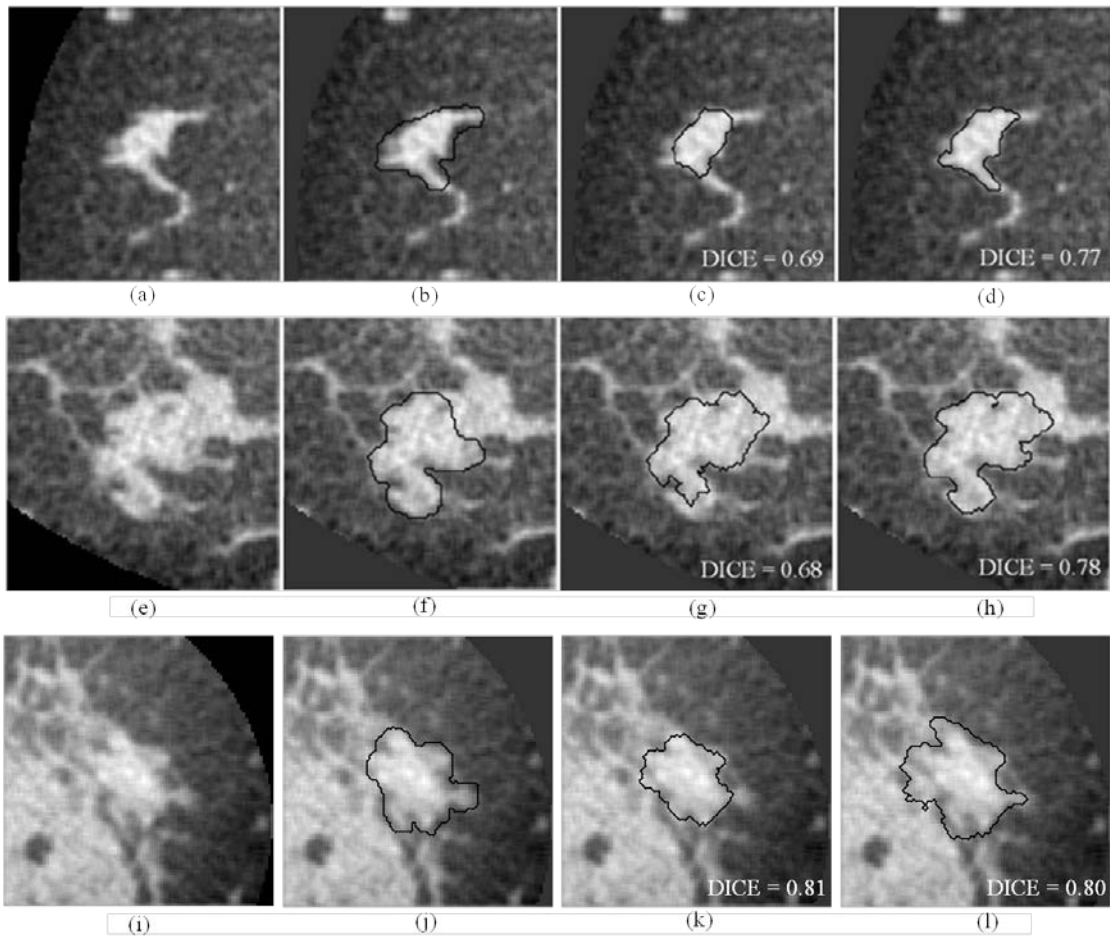


Figure 26. Three different Non-contrast bCT segmentation examples for each of the fibroglandular density classes. (a)-(d): 8% of fibroglandular proportion (low density). (e)-(h): 29% fibroglandular proportion (intermediate density; this lesion is also depicted in Fig. 11). (i)-(l): 46% fibroglandular proportion (high density). (b), (f) and (j): research specialist's outlines. (c), (g) and (k): segmentation results by original model. (d), (h) and (l): segmentation results by optimized model.

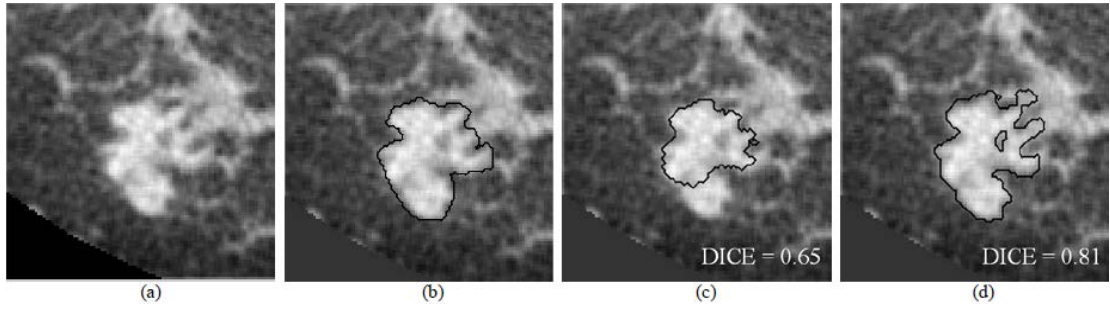


Figure 27. A contrast-enhanced bCT image example. (a): original VOI. (b): research specialist's outline. (c): segmentation result by using original model. (d): segmentation result by using optimized model. The proportion of fibroglandular tissue in the lesion vicinity is 29%.

D. Discussion and Conclusion

In this chapter, we modified our original 2-stage 3D lesion segmentation algorithm proposed in chapter III to allow for the inclusion of more shape detail. The region-fitting energy term introduced in the new model not only improved the delineation of shape detail, but also helped smooth the lesion contour and correct the contour evolution if the main driving term caused errors.

The optimized model did obtain statistically improved segmentation performance for the non-contrast bCT images ($p \ll 0.05$). The original model often missed shape details when a lesion presented with a complex margin (eg Fig. 27(c) and Fig. 26(g)). The improved ability to capture shape and margin characteristics should be useful

clinically since such morphological information plays an important role in diagnosis . Improvement in diagnosis on non-contrast bCT images is important, since contrast-enhanced bCT carries a risk of allergic reaction. Hence, the improved ability of the proposed method to capture shape details may have an impact on future implementations in CAD and allow for more accurate lesion classification. The optimized segmentation model failed to yield significant improvement over our original segmentation model on contrast-enhanced bCT images, likely because the conspicuity of cancers is significantly higher on contrast enhanced bCT [15] and reasonable segmentation performance with our original methods was facilitated by this conspicuity.

Breast density is a risk factor for breast cancer [83][84][85]. The masking effect of dense tissue reduces the sensitivity of imaging modalities in breast cancer diagnosis. Therefore, it is important to successfully segment lesions within dense tissue. In contrast-enhanced bCT, the segmentation performance appeared to decrease with higher volume glandular fraction (TABLE VI). However, the DICE for higher density breasts is still above 0.75 (TABLE VI, note that there are only 3 cases in the high-density class for contrast-enhanced bCT). In non-contrast bCT, the segmentation performance was affected when the proportion of fibroglandular tissues was

extremely high, but the DICE was still above 0.7 for both segmentation models (TABLE VI). According to TABLE VI, there is not much improvement for the $> 40\%$ category. Due to the similar X-ray attenuation of tumor masses and fibroglandular tissues, the optimized segmentation model could yield slightly oversegmented results and lead to a decrease in DICE since the original model possesses better ability to capture edge details (Fig. 26 (i)-(l)). Overall, both segmentation models behaved similarly with respect to the volume glandular fraction.

There is a limitation to this study. For each imaging modality, only a single expert outlined the lesions which defined the reference standard for segmentation. To conclude, in this chapter we presented a 3-dimensional segmentation method adapted and refined from our original model developed for contrast-enhanced breast CT [74], and evaluated the methods on dedicated breast CT (both contrast-enhanced and non-contrast bCT). We obtained promising results that warrant future implementation within computer-aided diagnosis software platforms and quantitative imaging.

VI. TASK-BASED EVALUATION OF LESION SEGMENTATION:

FEATURE ANALYSIS AND LESION CLASSIFICATION

A. Introduction

The diagnosis of masses in mammography relies on characterization of mass shape, margin, and density [86][87]. D’Orsi and Kopans reported that masses with irregular shapes, indistinct or spiculated margins, and higher density are considered highly suspicious [86]. Among different morphological features, spiculation, defined as fine lines radiating from its margins, is said to be the strongest sign for malignancy [86]. Several types of breast cancer are associated with spiculations [88], including infiltrating ductal carcinoma (IDC), tubular carcinoma, infiltrating lobular carcinoma (ILC), and ductal carcinoma in situ (DCIS). Except for DCIS, most spiculations indicate tumor infiltration. Computer-aided diagnosis (CADx) can also employ such criteria to extract features in distinguishing different lesion categories. In CADx for mammography, Brzakovic *et al* [31] classified detected abnormalities by using size, shape, and intensity change. Kegelmeyer [89] analyzed edge orientation histograms to detect stellate lesions. Kilday *et al* [90] measured circularity and merged several shape-related features to classify fibroadenomas, cysts, and carcinomas with linear discriminant analysis. Giger *et al* [91] calculated the standard

deviation of the margin fluctuation to measure the degree of spiculation. Huo *et al* [92] developed a spiculation-sensitive pattern-recognition technique by analyzing radial edge-gradient. Sahiner *et al* [93] extracted spiculation feature with the analysis of the gradient direction of the pixels on or close to the spiculation.

In mammography, where complex 3D tissue structures are being projected onto a 2D plane, the superimposition of fibroglandular tissues and tumor masses may hinder the characterization of lesions. This is the main reason that the PPV (positive predictive value) of biopsy performed based on diagnostic mammography is only 31.5% [94]. To address this limitation, dedicated breast CT (bCT) is being developed to generate high-resolution 3D images of the breast. This emerging technology not only retains 3D morphological details, but also provides higher tumor contrast with improved conspicuity of masses, compared to mammography [14][15], and thus, is likely to play an important role in future breast imaging [12]. On the other hand, large amounts of image data are generated by bCT for the radiologist to review. In our dataset, an image volume of one breast includes 512 slices in transverse and sagittal directions. For coronal planes, there are over 300 slices. Slices in 3 views might all need to be reviewed. Therefore, CADe is expected to improve the efficiency of the bCT reading task.

In chapter III to V, we have developed and optimized an automated lesion segmentation algorithm for dedicated bCT, which only requires labeled seed points as the input (Note that the labeled seed points can be either manually labeled or computer-labeled.). The segmentation algorithm yielded satisfactory results in terms of DICE value when measuring the overlap of manually-drawn and computer-segmented lesion outlines. Here we aim to utilize the computer-outlined lesion contours generated by our segmentation algorithm for feature extraction and lesion classification.

By using both texture features and morphological features, Ray *et al* [53] evaluated the performance of their CADx method on bCT and obtained area under the ROC curve (AUC) of 0.80 for their non-contrast bCT dataset ($N = 39$). However, their morphological features did not include a spiculation feature. To better utilize the advantages provided by this 3D imaging modality, we evaluated the degree of spiculation by analyzing the lesion surface and its relationship to the surrounding fibroglandular tissues in a VOI (volume of interest), and developed a new 3D lesion spiculation feature. In this chapter, we first compare the classification performance between the original and optimized segmentation algorithms, and then we aim to improve the CADx performance for breast masses on non-contrast bCT by including a

new spiculation feature in a classifier with other morphological features and texture features.

B. Methods

In this chapter, we used the unenhanced bCT image database for feature analysis and lesion classification based on the segmentation results generated by the algorithm proposed in chapter V. $N = 129$ masses, i.e., cases (80 benign, 49 malignant), from 116 image volumes. The median lesion size based on the optimized segmentation results was approximately 756 mm^3 (effective diameter 11.3 mm).

1. Morphological and Texture Features

The mathematical descriptions of the morphological and texture features used in this work are described in previously reported studies. We used 10 morphological features [51][81][95] and 14 texture features [38][96] based on the gray level co-occurrence matrix.. We calculated texture feature values both for the segmented lesions and background and the differences between them. Thus the total number of features was 63 (14 texture features for segmented lesions, 14 texture features for the background, and 10 morphological features plus the proposed spiculation feature “spiculation index”). Details for 3D texture features can be found in Chen *et al* [96].

2. Feature Selection and Analysis

The most dominant feature set was selected from a leave-one-case-out loop. In each step of the leave-one-case-out loop, stepwise feature selection was performed on $N - 1$ cases using multilinear regression ("stepwisefit", Matlab®, MathWorks, Inc) at a significance level of 0.05. After completion of all N feature selection steps in the leave-one-case-out loop, the most frequently selected feature *combination* was used in another leave-one-case-out loop using linear discriminant analysis (LDA) [40] for lesion classification [40]. LDA classifier output served as input to ROC analysis for performance assessment [97]. In this study, we used a Metz ROC software package (ROCKIT) to generate binormal ROC curves, with associated area under the curve, and compare different ROC curves (<http://metz-roc.uchicago.edu/>).

In order to gain a better insight into the effect of lesion size, we also performed the above analysis after dividing the lesion set in half, with lesions with a smaller effective diameter than the median value (11.3 mm) in one set and lesions with a larger diameter than the median in the other set.

3. Development of the New Spiculation Feature

The basic idea of computing of the new proposed spiculation feature, “spiculation index,” is to measure the number of connected regions of fibroglandular tissue and lesion surface. Thus, to compute the spiculation index, one needs to identify the fibroglandular tissues and adipose tissues first. Note that the identification of fibroglandular tissues and the computation of spiculation index were based on the results of the optimized segmentation model.

a. Automated Identification of Fibroglandular and Adipose Tissues

Identification of fibroglandular and adipose breast tissues was accomplished using a previously-developed fuzzy-c-means (FCM) based tissue segmentation scheme [81]. Tissue segmentation was performed in coronal slices of the breast images individually. First, to remove non-uniformity, which might be caused by incomplete scatter correction, a 3rd order polynomial surface fit was subtracted from each slice. Next, pixels were clustered into four FCM classes. The classes with the lowest and the second lowest average gray values were classified as adipose. The class with the highest average gray value was labeled as fibroglandular. The remaining class, with the third highest average gray value, was labeled as fibroglandular if its mean was more than 30 HU greater than that of the 2nd class,

otherwise it was labeled as adipose. This tissue segmentation was performed on cubic regions (50mm × 50mm × 50mm) centered on the lesion center.

b. Spiculation Index Computation

The scheme for extracting the proposed new feature from non-contrast bCT is shown in Fig. 28. The computation of spiculation feature needs both results of lesion segmentation and fibroglandular tissue identification.

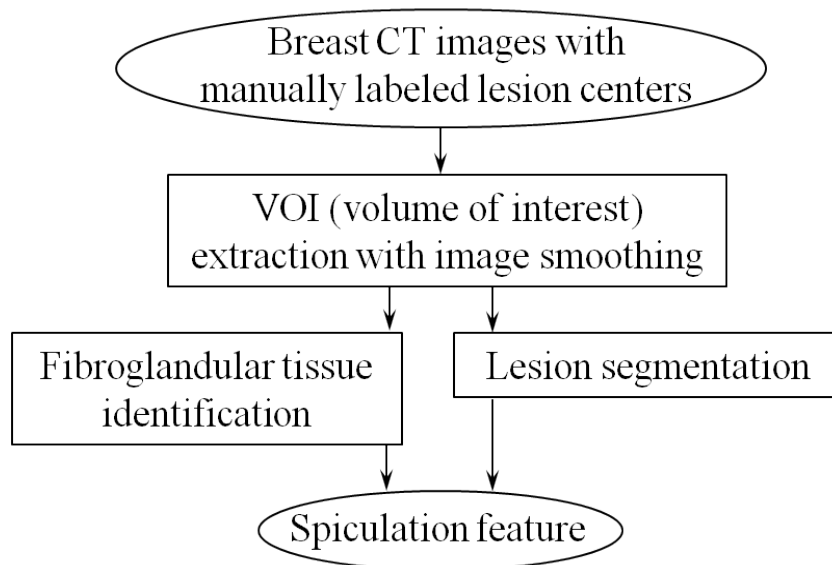


Figure 28. Flowchart of the computation of the spiculation feature for bCT images. Note that all steps except the first one are completely automated.

In mammography, spiculations appear as several thin fine lines growing outward from the lesion. In our dedicated breast CT image database, malignant lesions with spiculations tend to have a similar appearance (Fig. 27).

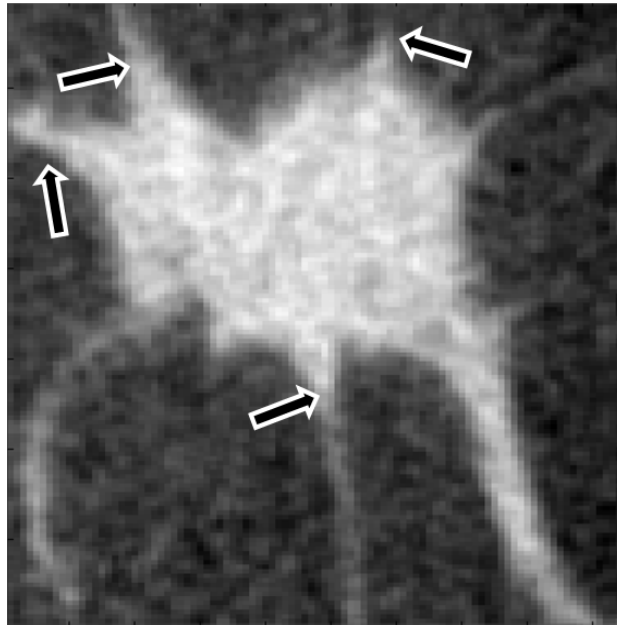


Figure 29. A cross section of a spiculated malignant mass imaged on breast CT. The arrows indicate the spiculations.

The spiculation feature was developed based on the observation that, while spiculations appear similar to fibroglandular tissue, there are differences in the structure of spiculations and normal fibroglandular tissue. Normal fibroglandular tissue tends to appear in larger regions, which could have any shape and occur in any region of the breast (i.e., anywhere with respect to the tumor). We also observed that, in our dataset, a large portion of the segmented lesion surface appeared connected to neighboring fibroglandular tissues (Fig. 30). Unlike normal fibroglandular tissue, spiculations are only associated with a tumor. If present, they appear as multiple, either long or short thin lines growing from the lesion surface.

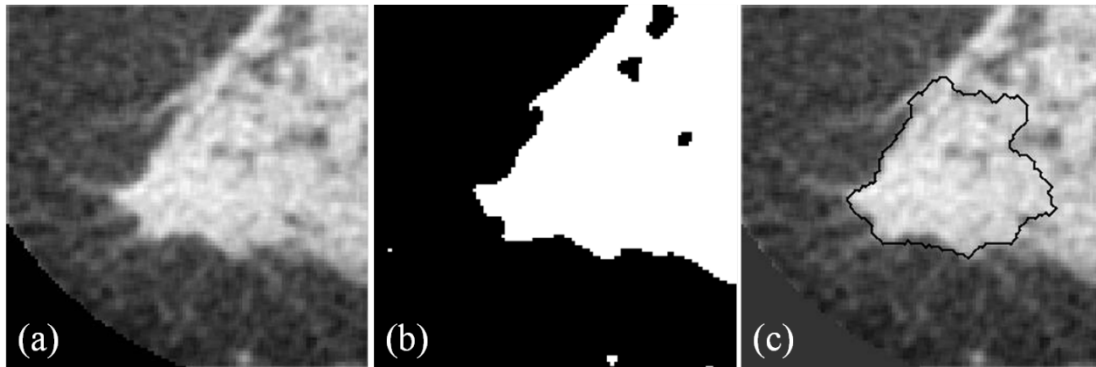


Figure 30. Example of a malignant lesion partially surrounded by, and connected to, fibroglandular tissue. (a) image, (b) tissue mask of fibroglandular tissue (including lesion), and (c) image with computer segmentation superimposed (solid black line)

Thus, by inspecting the relationship of fibroglandular tissue to the segmented lesion surface, we found that the intersection of fibroglandular tissue regions and the segmented lesion surface tended to be a single compact connected region, even if the lesion surface was connected to complex shaped fibroglandular tissues. On the other hand, when the segmented lesion surface intersected with tissue regions corresponding to spiculations, there tended to be multiple small separated regions that appeared to be randomly distributed on the lesion surface. Based on this observation, we counted the number of surface intersections of the segmented lesion surface with tissue regions as an index of spiculation. For a given lesion, the total number of connecting regions yields the spiculation index (Fig. 31).

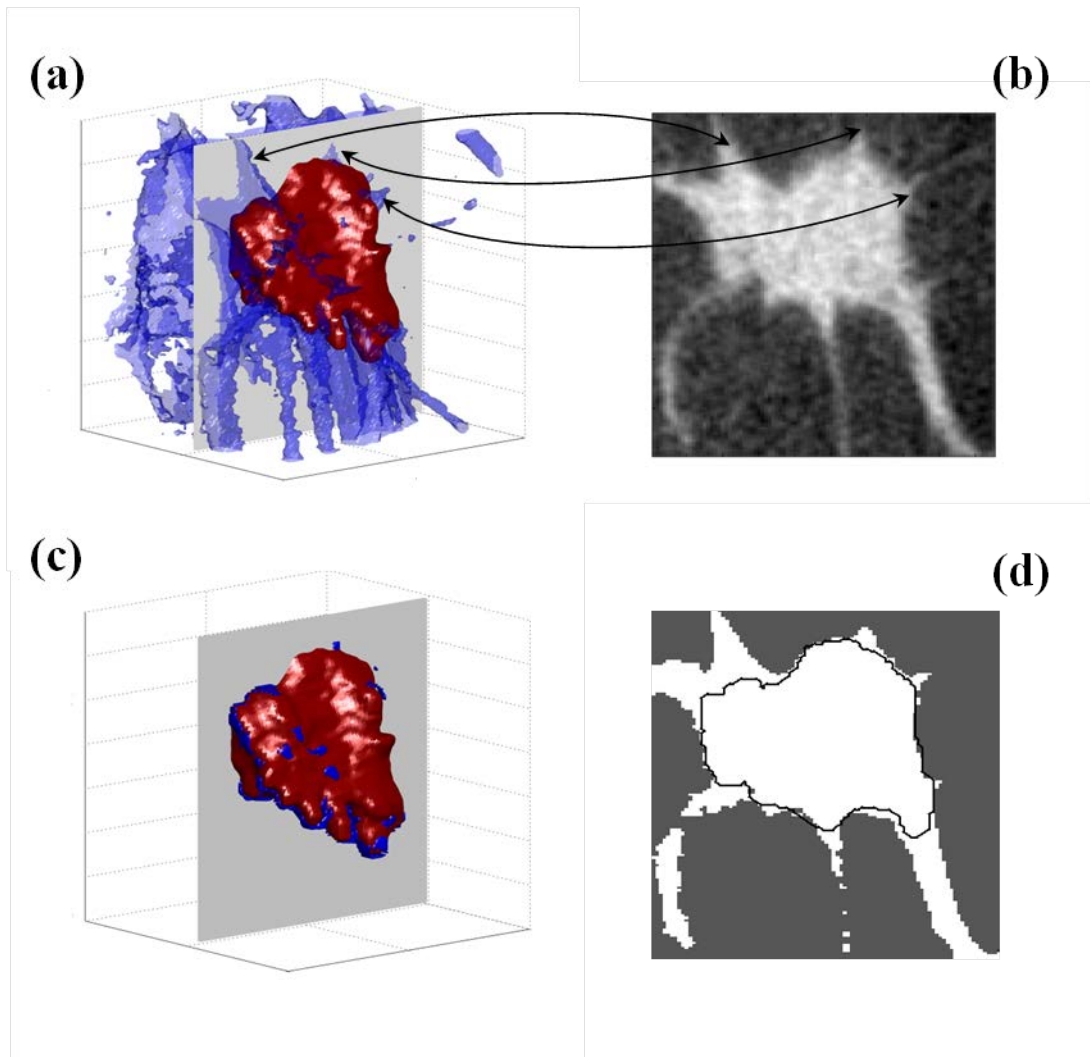


Figure 31. Illustration of the concept of the spiculation index feature. (a) 3D rendering of lesion (red) and tissue mask (blue), (b) 2D slice (image) through lesion, (c) 3D rendering of lesion (red) and the spiculations connected to fibroglandular tissue (blue), and (d) tissue mask of (b) with segmented lesion outline. Gray planes in (a) and (c) refer to the corresponding slice shown in (b) and (d). Arrows in (a) and (b) indicate spiculations.

C. Results

1. Comparison of Classification Performance between the Two Segmentation Models

We first compare the classification performance between the original and optimized segmentation algorithms without the new spiculation feature in the feature pool. Among 62 features without spiculation index, there was only one single feature, “difference of the sum average between the lesion and background” (termed as “DSumAverage”, see “Sum Average” in [38]), selected as the most frequently selected feature set for ROC analysis. For the optimized segmentation algorithm, the most frequently selected feature set from the feature pool without spiculation index included 5 features: irregularity2 [95], irregularity1 [81], entropy [38], ellipsoid axes ratio [81], and variance [38] (see TABLE VII). The AUC values of ROC analysis for the original and optimized segmentation algorithms are 0.62 ± 0.05 and 0.81 ± 0.04 , respectively. Figure 32 shows the comparison of each individual feature performance between the original and optimized segmentation algorithms. Note that the features shown in Fig. 32 are those included in the most dominant features set for the original and optimized segmentation algorithms.

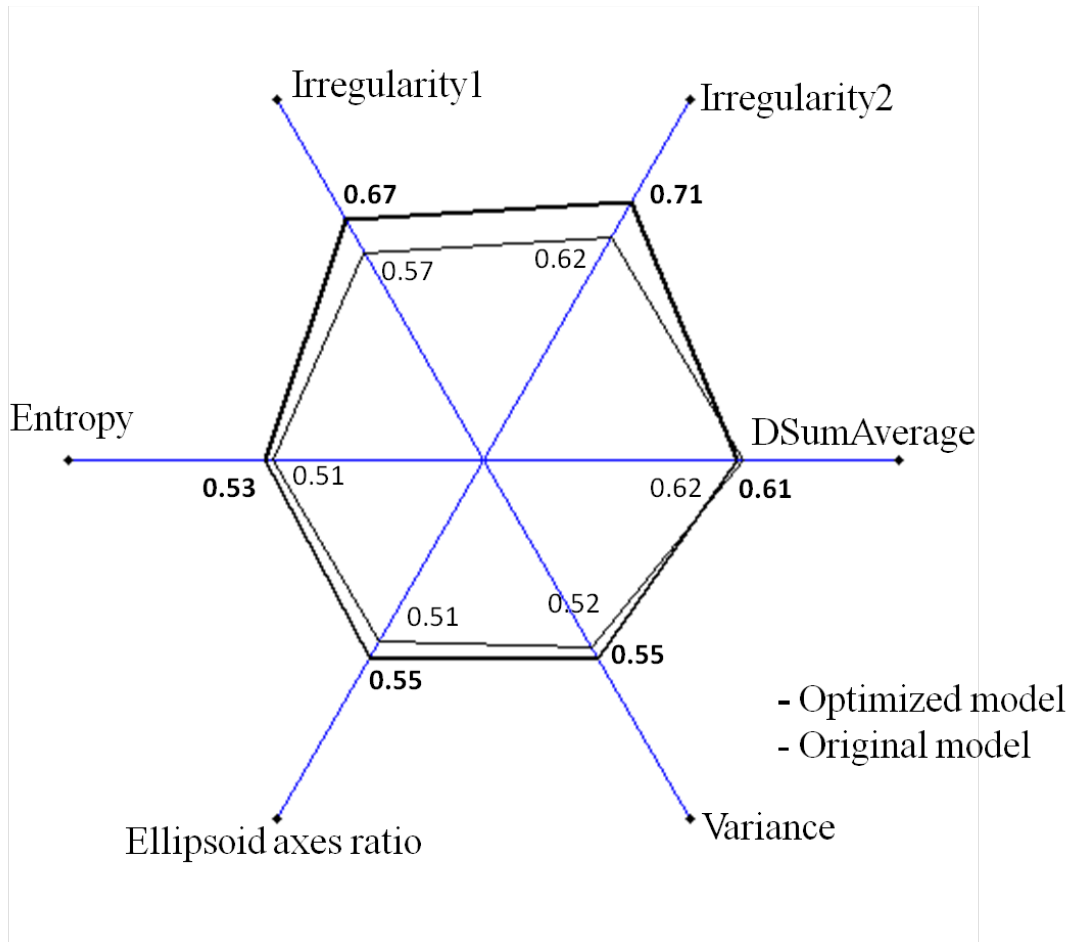


Figure 32. Comparison of individual feature classification performance in terms of AUC values between the two segmentation algorithms. Note that features shown in the figure are selected features contained in most dominant feature set for the original and optimized segmentation model.

2. Feature Analysis with and without Spiculation Index on the Optimized

Segmentation Model

Feature analysis with and without the new proposed spiculation feature was performed on the segmentation results generated by the optimized segmentation algorithm. Based on our studies, fibroglandular tissues connected to the segmented lesion surface tend to result in a larger region, regardless of any shape. Identified connected locations resulting from spiculation tend to present as multiple small regions. For our dataset, the average spiculation index value was substantially smaller for benign lesions than for malignant lesions. (TABLE VII). Other than the spiculation index, only irregularity2 and irregularity1 performed strongly as individual features with p -values < 0.05 and AUC greater than 0.65. Note that p -values of individual features are provided to illuminate trends rather than to provide a statistical comparison of the performance of individual features (for which correction for multiple comparisons would be necessary).

TABLE VII. FEATURE VALUES AND AREA UNDER THE ROC CURVE (AUC) OF INDIVIDUAL FEATURE AND COMBINED FEATURES. * AND † REFER TO FEATURES SELECTED FROM THE FEATURE POOL WHEN SPICULATION INDEX WAS AND WAS NOT INCLUDED, RESPECTIVELY.

Feature	Feature values (mean \pm std)		p -values [‡]	AUC \pm std
	Benign (N = 49)	Malignant (N = 80)		
^{**†} Irregularity2[95]	0.53 \pm 0.07	0.57 \pm 0.06	\ll 0.05	0.71 \pm 0.05
^{**†} Irregularity1[81]	0.83 \pm 0.06	0.81 \pm 0.05	0.01	0.67 \pm 0.05
^{**†} Entropy[38]	6.34 \pm 1.78	6.54 \pm 1.65	0.52	0.53 \pm 0.05
[*] Spiculation index	4.83 \pm 3.34	6.96 \pm 3.93	0.02	0.64 \pm 0.05
^{**†} Ellipsoid axes ratio[81]	0.63 \pm 0.14	0.65 \pm 0.11	0.29	0.55 \pm 0.06
^{**†} Variance[38]	592.71 \pm 1569.68	528.38 \pm 750.01	0.75	0.55 \pm 0.05
[*] Circularity[95]	0.73 \pm 0.09	0.72 \pm 0.07	0.51	0.54 \pm 0.06
[†] Connected area ratio	0.38 \pm 0.18	0.43 \pm 0.22	0.13	0.60 \pm 0.05
	Merging only features labeled with *			0.85 \pm 0.03
	Merging only features labeled with †			0.81 \pm 0.04

[‡] p -values were obtained from 2-sided t-tests

TABLE VII shows the most dominant feature combinations. The most frequently-selected combination occurred 48% of the time, and included a total of seven features (labeled with * in TABLE VII). Note that the spiculation index was part of all selected feature combinations, when it was included in the feature selection process. The spiculation index demonstrated only weak correlation with the irregularity features (TABLE VIII). The spiculation index differentiates malignant from benign lesions even when they have similar irregularity measures (Fig. 33). It is also interesting to note that, although both irregularity features (irregularity1 and irregularity2) were highly correlated, they were both selected in combination in the leave-one-case-out feature selection loop (TABLE VIII). The LDA classifier using all seven features yielded an AUC of 0.85 ± 0.03 (Fig. 34) using leave-one-case-out analysis.

TABLE VIII. CORRELATION COEFFICIENTS AND STATISTICAL SIGNIFICANCE BETWEEN EACH TWO SELECTED FEATURES

	Irregularity2	Irregularity1	Entropy	Spiculation index	Ellipsoid axes ratio	Variance	Circularity	Connected area ratio
Irregularity2	-	R=-0.92 $p \ll 0.001$	R=0.58 $p \ll 0.001$	R=0.13 $p=0.06$	R=-0.13 $p=0.13$	R=0.27 $p=0.002$	R=-0.35 $p \ll 0.001$	R=0.46 $p \ll 0.001$
Irregularity1	-	-	R=-0.47 $p \ll 0.001$	R=-0.16 $p=0.15$	R=0.23 $p=0.009$	R=-0.18 $p=0.04$	R=0.53 $p \ll 0.001$	R=0.26 $p=0.002$
Entropy	-	-	-	R=0.10 $p=0.28$	R=0.23 $p=0.008$	R=0.41 $p \ll 0.001$	R=0.15 $p=0.08$	R=0.58 $p \ll 0.001$
Spiculation index	-	-	-	-	R=0.02 $p=0.85$	R=0.19 $p=0.03$	R=0.06 $p=0.51$	R=-0.26 $p=0.003$
Ellipsoid axes	-	-	-	-	-	R=0.33 $p \ll 0.001$	R=0.76 $p \ll 0.001$	R=0.35 $p \ll 0.001$
Variance	-	-	-	-	-	-	R=0.28 $p=0.001$	R=0.27 $p=0.002$
Circularity	-	-	-	-	-	-	-	R=0.26 $p=0.003$

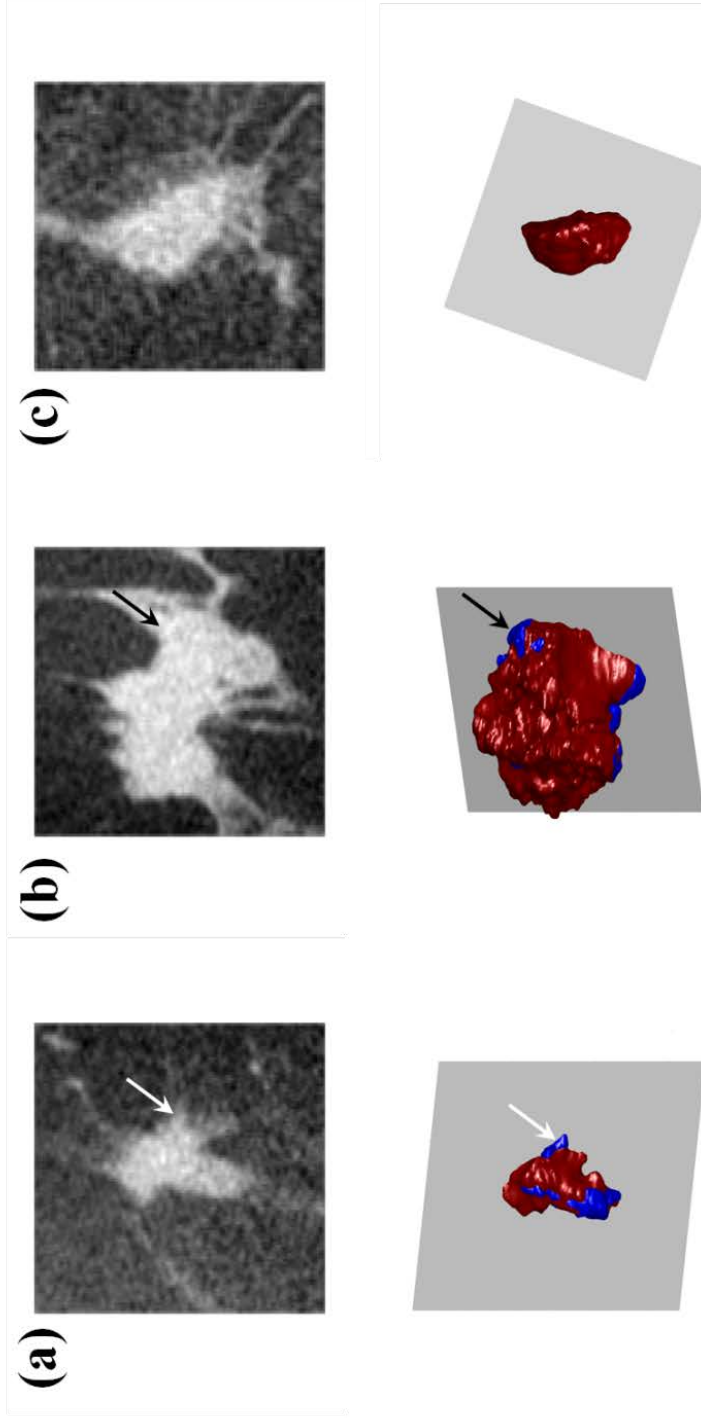


Figure 33. Illustration of the low correlation between the spiculation index and irregularity features. The top row shows the image slice through 3 lesions at the location of the gray plane in the corresponding 3D rendering of each lesion (red) (with the parts connected to fibroglandular tissue in blue) in the bottom row. (a) malignant lesion with spiculation index = 9 and irregularity2 = 0.56, (b) malignant lesion with spiculation index = 7 and irregularity2 = 0.65, (c) malignant lesion with spiculation index = 1 and irregularity2 = 0.55. Arrows indicate some of the spiculations.

When the spiculation index was not included in the feature selection leave-one-case-out analysis, the most dominant feature combination (appeared 72%) included only six features (labeled † in TABLE VII), which were selected by leave-one-case-out stepwise feature selection. The LDA classifier with these six features, yielded an AUC of 0.81 ± 0.04 (Fig. 34). The improvement in AUC value upon including the spiculation feature, from $AUC = 0.81$ to 0.85 , was statistically significant with a p -value $\ll 0.001$.

We found that the classification performance was higher for larger lesions than for smaller lesions with the features used in this study (Fig 35 and 36). Irregularity2 was selected for both lesion groups, but spiculation index and ellipsoid axes ratio were only selected when analyzing the ‘larger lesion’ group.

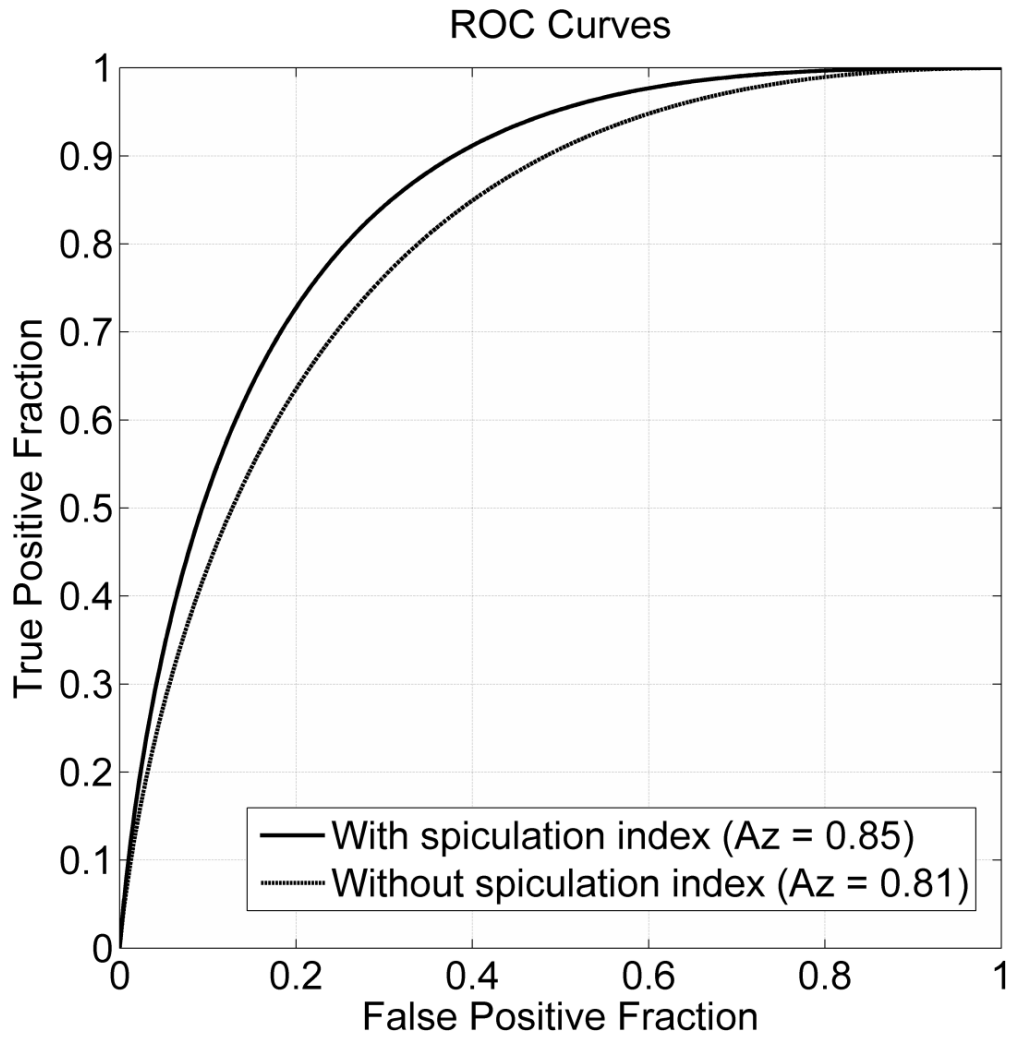


Figure 34. ROC curves indicating performance of merged selected features with and without the spiculation index in the task of distinguishing between malignant and benign bCT lesions. (The results are based on the optimized segmentation)

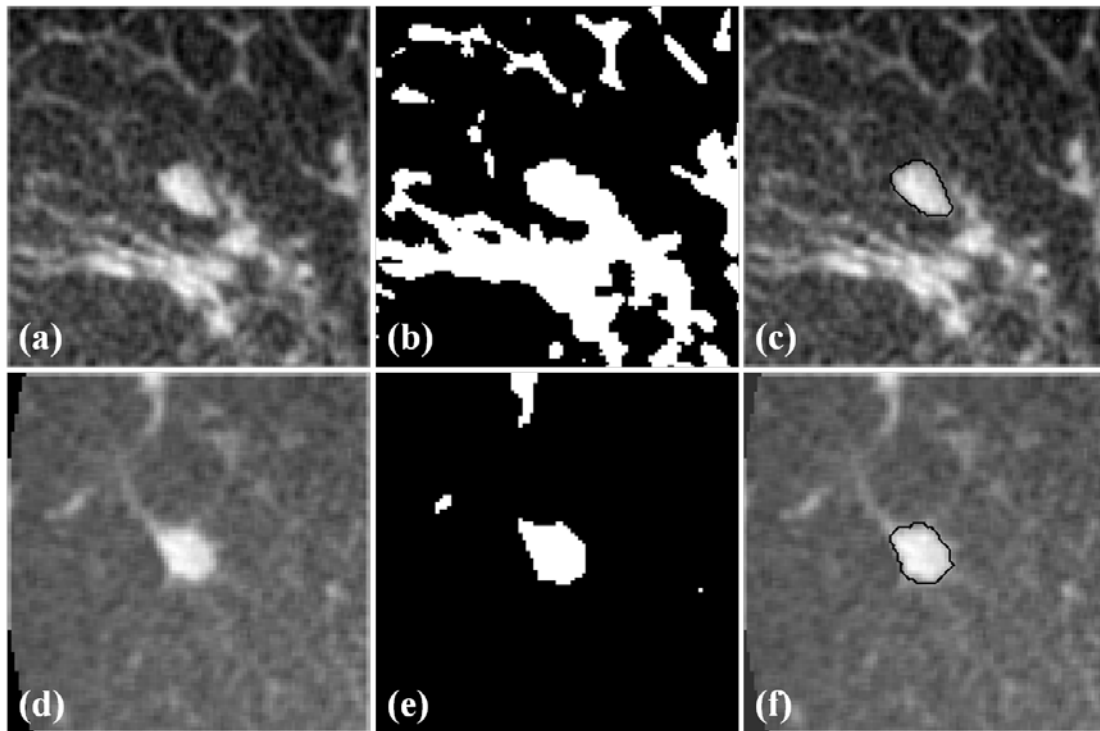


Figure 35. Examples of small lesions. (a) image of benign lesion, size: 79.1 mm^3 , [irregularity2] = 0.49, (b) corresponding fibroglandular tissue mask, (c) image with computer segmentation superimposed (solid black line), (d) image of malignant lesion, size: 59.4 mm^3 , [irregularity2] = 0.46, (e) fibroglandular tissue mask, and (f) image with computer segmentation superimposed (solid black line)

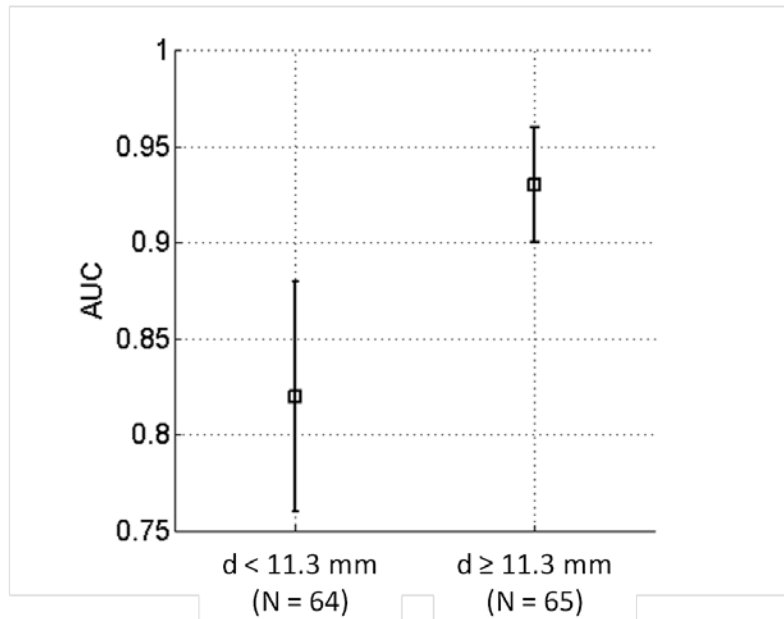


Figure 36. The CAD performance in terms of AUC for lesions with effective diameter $d < 11.3$ mm and $d \geq 11.3$ mm. Error bars are the standard errors of AUC.

D. Discussion and Conclusion

In this chapter, we evaluate the two segmentation models with feature analysis. To further improve the classification performance, we investigated the features extracted based on the lesion contour generated by our optimized segmentation algorithm, and a new lesion spiculation feature, the ‘spiculation index’, which measures the degree of spiculation on non-contrast-enhanced breast CT lesions by taking advantage of the 3D structural details retained in bCT image volumes. As shown in Fig. 32, the performances of irregularity features show that our optimized

segmentation model can more successfully capture lesion shape details than the original model. Thus irregularity features became the strongest among our feature pool when the segmented lesions from the optimized model were used. When the original segmentation model was used, none of the morphological features were selected, indicating that the original model failed to capture sufficient shape details for lesion classification.

The spiculation index measures the total number of connected regions, indicating the connection of the segmented lesion surface with glandular tissue. The usefulness of the new spiculation index was demonstrated in breast lesion classification – with and without inclusion of the spiculation index – resulting in a statistically improved performance when the spiculation index was included (p -value $\ll 0.001$) (Fig. 34).

The issue masks of fibroglandular tissue (versus adipose tissue) were calculated by a method originally developed for lesion detection in bCT [81]. The results in this study indicate that the method to determine the fibroglandular tissue mask is robust and useful for applications other than lesion detection. It may be possible to further optimize this method for lesion classification in future studies.

In our study, the LDA classifier obtained an AUC of 0.81 for lesion classification *without* the spiculation index, which is consistent with the work of Ray *et al* [53]. Also consistent with the work of Ray *et al.* is that texture features did not appear to contribute much to the classification performance. In their report, the area under the curve for classification using only texture features was 0.64. For the two texture features selected in our study (entropy and variance), we failed to demonstrate a significant difference between benign and malignant lesions, suggesting that these texture features, which are based on gray-level changes of voxels, might not be appropriate for tumor mass classification on bCT.

As shown in Fig. 35, the lack of information within the limited number of voxels in very small lesions might cause difficulties classifying lesions for ‘smaller’ lesion group (Fig. 36). In Fig. 35(d), there are still some slight spiculations visualizable. The performance for ‘smaller’ lesion group could be improved by increasing the sensitivity of fibrolandular-identification algorithm.

There were several limitations to this study. The first limitation was the rather modest size of the dataset and the fact that we developed and tested our new spiculation feature on the same dataset. Another limitation of this study was that we

performed a ‘double loop’ leave-one-case-out analysis: one leave-one-case-out analysis for feature selection and another subsequent loop for classification using the most frequently selected feature combination. This is expected to bias the overall results somewhat in terms of achieved AUC value, Since we are comparing two methods (with and without the new spicualtion index), however, this bias is expected to cancel in the performance comparison.

In sum, the optimized segmentation model can capture essential shape details which are important for lesion classification. It made irregularity2 and irregularity1 substantially contribute to lesion classification task. Since the texture features failed to contribute to classification and is not so relevant to the segmented lesion shape, the ability to capture the shape information makes the optimized segmentation model much more favored, and is suggested as a desirable method for breast lesion segmentation on bCT. In addition, we developed a new lesion feature that takes advantage of the 3D structures retained in breast CT image volumes and measures the degree of spiculation infiltrating into surrounding fibroglandular tissue. This spiculation index proved very useful for the task of distinguishing between benign and malignant breast lesions and significantly improved classification performance. Our findings on the performance of the 3D quantitative spiculation feature, as an

independent and strong discriminating characteristic, is consistent with clinical observation. Given that breast CT, without the problem of superimposition, has clearer 3D structural details over 2D mammograms of both the lesion and the surrounding parenchymal background, further investigation and inclusion of lesion-background characteristics may aid in developing new features for CADx on breast CT.

VII. PRELIMINARY INVESTIGATION OF SEGMENTATION TECHNIQUES

ON 3D BREAST ULTRASOUND LESIONS

The content of this chapter has been accepted by Journal of Medical Imaging for publication, and partially published on Proceedings of SPIE,

[72] **H. Kuo**, M. L. Giger, I. Reiser, K. Drukker, A. Edwards, and C. a. Sennett, “Automatic 3D lesion segmentation on breast ultrasound images,” in *Proceedings of SPIE*, 2013, vol. 8670, pp. 867025.

A. Introduction

Recently, interest in 3D automated breast ultrasound (ABUS) was revived after initial attempts failed decades ago due to poor ultrasound technology. The advantage of ultrasound in general is that it does not involve ionizing radiation, but for hand-held ultrasound disadvantages include operator dependency and non-reproducibility. The advantages of ABUS over hand-held ultrasound are not only that it is reproducible, but also that it can visualize images in the coronal plane in addition to the traditional axial and sagittal planes. It was recently shown that ABUS is capable of depicting small early stage mammographically-occult cancers [18][98][19]. In a reader study [98][99], statistically significant improvement in readers’ performance and reduction in interreader variability in the detection of mammographically-occult cancers were demonstrated for a combination of screening digital X-ray mammography and ABUS as compared to screening mammography

alone.

It is likely that ABUS (as well as bCT) will play a crucial role in future breast cancer diagnosis, screening of high risk populations, and perhaps even as an adjunct screening modality for the general population. However, just like bCT, interpreting these 3D image volumes could be a very challenging and time consuming task for radiologists. As an initial and essential step towards developing a computer-aided diagnosis (CADx) scheme for ABUS, a sufficient segmentation procedure is necessary.

In this chapter we aim to test the two segmentation algorithms proposed in chapter III and V on ABUS images. As an additional robustness analysis for 3D ABUS, a comparison of segmentation performance on mammographically-positive and mammographically-occult lesions was conducted.

B. Methods

We separately segmented 98 images by using the segmentation model of Eq. (III.9) and Eq. (V.14). Segmentation results were evaluated by Eq. (V.17). We also assessed segmentation performance whether there were any differences in performance between lesions that were occult on mammography and those that were

visible on mammography. Note that all lesions in this 3D US dataset were malignant. Since US is known for its ability to detect mammographically-occult cancers and has recently been approved in the U.S. as an adjunct screening modality for women with dense breasts, it is important to assess performance of our segmentation methods for mammographically-negative and mammographically-positive lesions separately.

C. **Results**

As shown in TABLE IX, the p -values suggest that there is no difference between the two models. Fig. 37 show the fraction of lesions correctly segmented at various overlap (Dice coefficient) thresholds in bCT and 3D ABUS, with several segmentation examples shown in Fig. 38. The value of the correlation coefficient of DICE and tumor size was also calculated and yielded a value of 0.038 [72].

TABLE IX SEGMENTATION RESULTS FOR 3D BREAST ULTRASOUND

	Average Size	Segmentation Model	Performance in DICE (mean \pm std)	Percentage of ≥ 0.7 DICE	p -value of paired t -test between the two models
Mammographically occult ($N = 54$)	16.79 \pm 13.20 (mm)	Original Model	0.73 \pm 0.15	77%	0.57
		Optimized Model	0.72 \pm 0.18	71%	
Mammographically positive ($N = 44$)	19.41 \pm 12.31 (mm)	Original Model	0.69 \pm 0.15	61%	0.57
		Optimized Model	0.71 \pm 0.13	63%	
Total images ($N = 98$)	17.97 \pm 12.80 (mm)	Original Model	0.72 \pm 0.13	70%	0.93
		Optimized Model	0.71 \pm 0.16	68%	

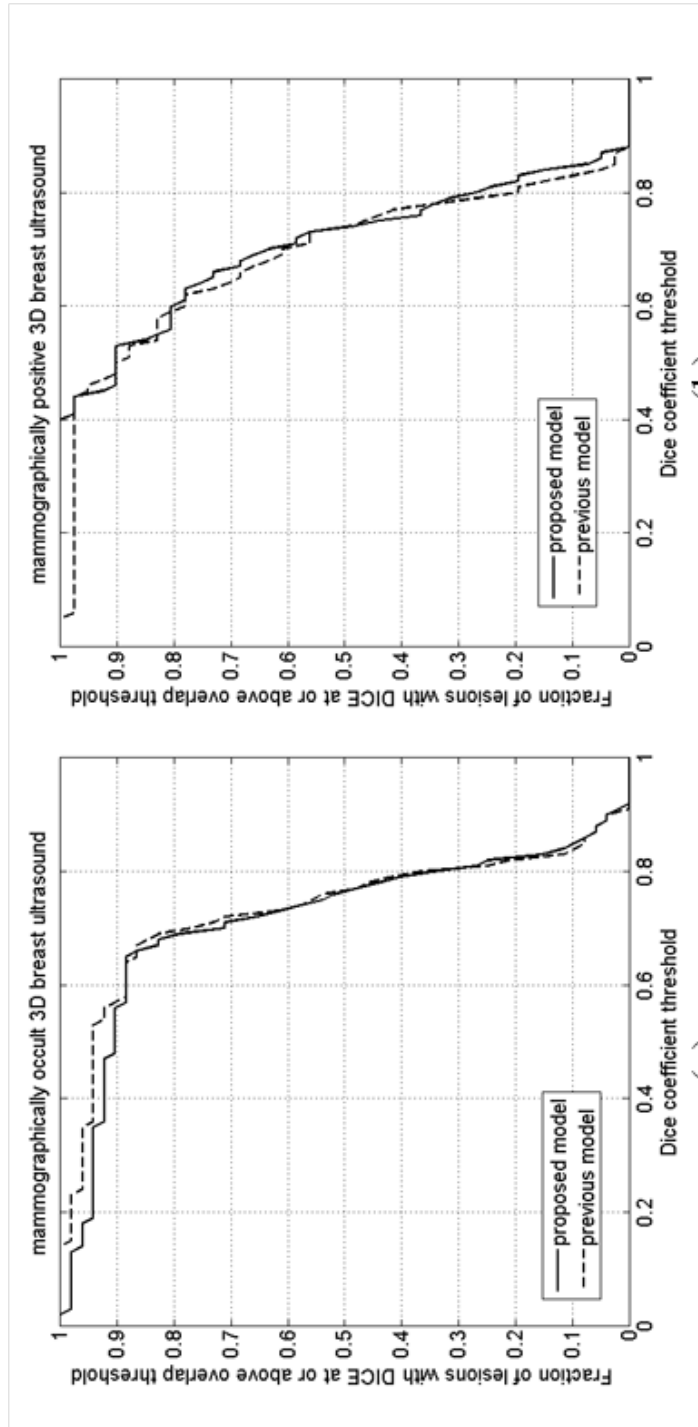


Figure 37. Segmentation performance in 54 mammographically occult (a), and 44 mammographically positive (b) 3D breast US images.

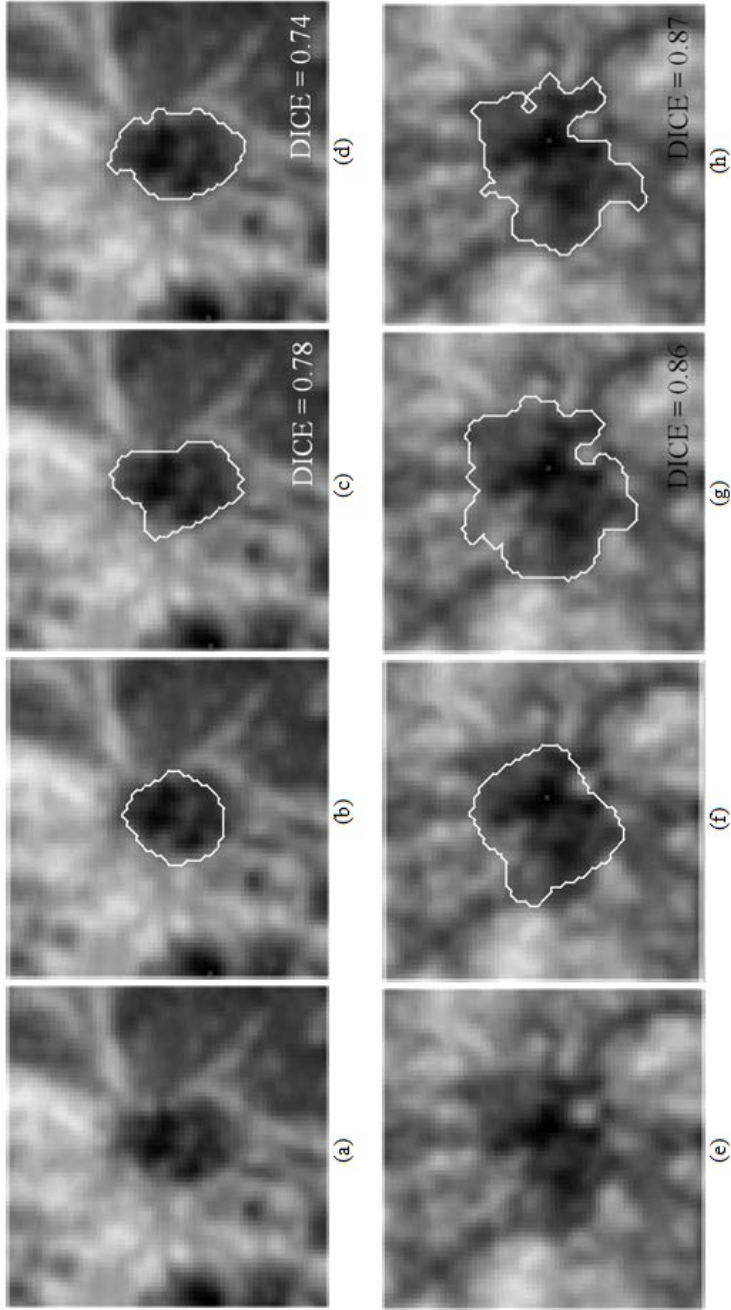


Figure 38. Two cancer examples of 3D breast ultrasound segmentation. (a)-(d): mammographically occult example. (e)-(h): mammographically positive example. (b) and (f): medical doctor's outlines. (c) and (g): segmentation results by previous procedure. (d) and (h): segmentation results by proposed procedure. Unlike traditional ultrasound images displaying in axial or sagittal planes, the images shown in this figure are displayed in coronal planes.

D. Discussion and Conclusion

Based on our results, there were even slightly more fraction of mammographically-occult cancers yielded sufficient segmentation with $DICE \geq 0.7$. It is desirable for US segmentation since US is used as an adjunct to screening mammography for the purpose of detecting mammography-occult lesions. And this property is also consistent with that the US has the ability of detecting small-sized and mammography-negative lesions [18]. The value of the correlation coefficient of DICE value and tumor size (0.038) shows that the segmentation is not influenced by tumor size and can also handle segmentation for small lesions on 3D ABUS images well. The results showed similar performance for the original and optimized segmentation models (TABLE IX). Both models yielded sufficient segmentation results in terms of $DICE \geq 0.7$ (average value), which is deemed ‘good’ [71], as a measure of the overlap of manually-drawn and computer-segmented outline (TABLE IX), The presence of ultrasound speckle and anisotropic image resolution may be the cause of the lack of improvement. It should be noted, however, that performance of both models was quite satisfactory, demonstrating the robustness of our segmentation methods across 3D imaging modalities, holding promise for potential future application to other 3D breast images. The limitation includes that we did not attempt to optimize our methods for the ABUS images, and further

ultrasound-modality-specific improvements to the segmentation model may be possible.

VIII. DISCUSSION AND CONCLUSION

There were four aims to be achieved in this research project: 1) Development of 3D segmentation techniques for dedicated breast CT; 2) Optimization of 3D lesion segmentation of dedicated breast CT; 3) Task-based evaluation of lesion segmentation; 4) Preliminary investigation of segmentation techniques on 3D automated breast ultrasound lesions.

The first aim was completed by proposing a dual-stage segmentation procedure, which combines RGI segmentation for lesion contour initialization and a modified level set-based active contour algorithm for finalizing the segmentation task. This technique was developed on dedicated breast CT, and the results were satisfactory in terms of a measure of overlap of manually-drawn and computer-segmented outline [74]. In a test of this segmentation algorithm applying to unenhanced image pairs, the results showed that the segmentation tend to be conservative which lead to be smaller lesion contours. This suggested that, for unenhanced bCT, the originally developed segmentation algorithm might lose important lesion shape details which are often used as indicators for classifying malignant lesions form benign. Thus, the optimization of the originally segmentation model was developed. By adding a local region fitting energy term to the corresponding energy functional of the original

segmentation model, the optimization was completed by computing the corresponding Euler-Lagrange equation of this new energy functional. Although this optimized segmentation model did not show significant improvement on contrast-enhanced bCT (mainly because of sufficiently highlighted lesions in contrast-enhanced images), the performance on unenhanced bCT images were significantly improved and was robust for different fraction of fibroglandular tissues existing in the lesion neighborhood.

In order to reach the goal of CADx (computer-aided diagnosis), a task-based evaluation of the optimized segmentation algorithm was also performed. A number of texture features and morphologic features were extracted from the segmented lesions, and the results showed that irregularity feature was the most dominant and strong feature among the whole feature pool and yielded $AUC > 0.7$ for a single irregularity feature. This also indicates that the optimized segmentation algorithm can successfully capture essential shape information for classification task. Moreover, a new independent spiculation feature that utilized 3D structural information and fibroglandular tissue identification algorithm was developed. By adding this new feature, the classification performance was significantly improved from 0.81 to 0.85 with $p \ll 0.001$. One limitation of this new feature is that we developed and tested the spiculation feature on the same dataset due to that the size our image database is

not very large. However, the results still indicate a new idea of developing features not only based on the lesion but also utilizing the information gathered from the lesion neighborhood. Since the 3D structure is well retained in emerging 3D imaging modalities, 3D features such as spiculation features could have great potential for future screening.

In our 3D ABUS images, all cases were cancers. Although this limited us to proceed to classification on 3D ABUS, the segmentation results showed that our segmentation models are robust for both dedicated bCT and 3D ABUS, indicating that the segmentation on 3D ABUS images might only need minor adjustment to be optimized. This also suggests that our segmentation algorithm could be cross imaging modalities, and is worth further investigation for wider future applications. Furthermore, the segmentation performance was not affected whether the lesion was mammographically-occult or not, making it as a much favored property for potential future screening application.

As conclusion, a segmentation algorithm that has the potential to be applied across different 3D breast imaging modalities was developed. This segmentation algorithm captures sufficient shape details of the lesion, which is an important

indicator for differentiating malignant from benign. To further improve the classification task, an independent feature that utilizes the 3D structural information in lesion neighborhood was developed. With this new feature, the classification performance was significantly improved. This result indicates that new features which incorporate 3D structural information from the surrounding parenchymal patterns should be further investigated for future CAD application.

CITED LITERATURES

- [1] American Cancer Society, *Cancer Facts & Figures*. Atlanta: American Cancer Society, Inc., 2013.
- [2] S. J. Glick, “Breast CT.,” *Annu. Rev. Biomed. Eng.*, vol. 9, pp. 501–526, 2007.
- [3] C. J. D’Orsi and E. a Sickles, “To seek perfection or not? That is the question.,” *Radiology*, vol. 265, pp. 9–11, 2012.
- [4] K. Jørgensen, J. Keen, and P. Gøtzsche, “Is mammographic screening justifiable considering its substantial overdiagnosis rate and minor effect on mortality?,” *Radiology*, vol. 260, pp. 621–627, 2011.
- [5] A. Fischmann, K. C. Siegmann, A. Wersebe, C. D. Claussen, and M. Müller-Schimpfle, “Comparison of full-field digital mammography and film-screen mammography: image quality and lesion detection.,” *Br. J. Radiol.*, vol. 78, pp. 312–315, 2005.
- [6] S. A. Reese, David F., Carney Aidan, J., Gisvold, John J., Karsell, Philip R., Kollins, “Computerized reconstructive tomography applied to breast pathology,” in *76th Annual Meeting of the American Roentgen Ray Society*, 1976, pp. 406–412.
- [7] C. H. J. Chang, J. L. Sibala, S. L. Fritz, J. H. Gallagher, S. J. Dwyer III, and A. W. Templeton, “Computed tomographic evaluation of the breast,” *Am. J. Roentgenol.*, vol. 131, pp. 459–464, 1978.
- [8] J. J. Gisvold, D. F. Reese, and P. R. Karsell, “Computed tomographic mammography (CTM).,” *Am. J. Roentgenol.*, vol. 133, pp. 1143–1149, 1979.
- [9] K. Miyake, K. Hayakawa, M. Nishino, Y. Nakamura, T. Morimoto, Y. Urata, H. Ueda, M. Tanikake, S. Kanao, T. Shiozaki, and A. Yamamoto, “Benign or malignant?: differentiating breast lesions with computed tomography attenuation values on dynamic computed tomography mammography.,” *J. Comput. Assist. Tomogr.*, vol. 29, pp. 772–779, 2005.
- [10] B. K. Seo, E. D. Pisano, K. R. Cho, P. K. Cho, J. Y. Lee, and S. J. Kim, “Low-dose multidetector dynamic CT in the breast: preliminary study.,” *Clin. Imaging*, vol. 29, pp. 172–178, 2005.

- [11] W. A. Kalender, M. Beister, J. M. Boone, D. Kolditz, S. V Vollmar, and M. C. C. Weigel, "High-resolution spiral CT of the breast at very low dose: concept and feasibility considerations.," *Eur. Radiol.*, vol. 22, pp. 1–8, 2012.
- [12] K. K. Lindfors, J. M. Boone, M. S. Newell, and C. J. D'Orsi, "Dedicated breast computed tomography: the optimal cross-sectional imaging solution?," *Radiol. Clin. North Am.*, vol. 48, pp. 1043–1054, 2010.
- [13] J. Boone, T. Nelson, K. Lindfors, and J. Seibert, "Dedicated Breast CT: Radiation Dose and Image Quality Evaluation," *Radiology*, vol. 221, pp. 657–667, 2001.
- [14] K. Lindfors, J. Boone, T. Nelson, K. Yang, A. Kwan, and A. Miller, "Dedicated Breast CT: Initial Clinical Experience," *Radiology*, vol. 246, pp. 725–733, 2008.
- [15] N. D. Prionas, K. K. Lindfors, S. Ray, L. A. Beckett, W. L. Monsky, and J. M. Boone, "Contrast-enhanced Dedicated Breast CT : Initial Clinical Experience," *Radiology*, vol. 256, pp. 714–723, 2010.
- [16] P. T. Huynh, A. M. Jarolimek, and S. Daye, "The false-negative mammogram," *RadioGraphics*, vol. 18, pp. 1137–1154, 1998.
- [17] D. D. Dershaw, "Breast disease missed by mammography," *Appl. Radiol.*, vol. 26, pp. 24–28, 1997.
- [18] T. M. Koib, J. Lichy, and J. H. Newhouse, "Occult Cancer in Women Dense Breasts : Detection with Screening US - Diagnostic Yield and Tumor Characteristics," *Radiology*, vol. 207, pp. 191–199, 1998.
- [19] T. M. Kolb, J. Lichy, and J. H. Newhouse, "Comparison of the performance of screening mammography, physical examination, and breast US and evaluation of factors that influence them: an analysis of 27,825 patient evaluations," *Radiology*, vol. 225, pp. 165–175, 2002.
- [20] H. M. Zonderland, E. G. Coerkamp, J. Hermans, M. J. Van De Vijver, and A. E. Van Voorthuisen, "Diagnosis of breast cancer: contribution of US as an adjunct to mammography.," *Radiology*, vol. 213, pp. 413–422, 1999.
- [21] I. Leconte, C. Feger, C. Galant, M. Berlière, B. Vande Berg, W. D'Hoore, and B. Maldague, "Mammography and subsequent whole-breast sonography of

- nonpalpable breast cancers: the importance of radiologic breast density.,” *Am. J. Roentgenol.*, vol. 180, pp. 1675–1679, 2003.
- [22] W. A. Berg, J. D. Blume, J. B. Cormack, E. B. Mendelson, D. Lehrer, M. Böhm-Vélez, E. D. Pisano, R. A. Jong, W. P. Evans, M. J. Morton, M. C. Mahoney, L. H. Larsen, R. G. Barr, D. M. Farria, H. S. Marques, and K. Boparai, “Combined screening with ultrasound and mammography vs mammography alone in women at elevated risk of breast cancer.,” *J. Am. Med. Assoc.*, vol. 299, pp. 2151–2163, 2008.
- [23] K. M. Kelly, J. Dean, W. S. Comulada, and S.-J. Lee, “Breast cancer detection using automated whole breast ultrasound and mammography in radiographically dense breasts,” *Eur. Radiol.*, vol. 20, pp. 734–742, 2010.
- [24] M. L. Giger, H.-P. Chan, and J. Boone, “Anniversary Paper: History and status of CAD and quantitative image analysis: The role of Medical Physics and AAPM,” *Med. Phys.*, vol. 35, pp. 5799–5820, 2008.
- [25] B. D. Gallas, H.-P. Chan, C. J. D’Orsi, L. E. Dodd, M. L. Giger, D. Gur, E. A. Krupinski, C. E. Metz, K. J. Myers, N. A. Obuchowski, B. Sahiner, A. Y. Toledano, and M. L. Zuley, “Evaluating imaging and computer-aided detection and diagnosis devices at the FDA.,” *Acad. Radiol.*, vol. 19, pp. 463–477, 2012.
- [26] R. M. Summers, “Evaluation of computer-aided detection devices: consensus is developing.,” *Acad. Radiol.*, vol. 19, pp. 377–379, 2012.
- [27] B. van Ginneken, C. M. Schaefer-Prokop, and M. Prokop, “Computer-aided diagnosis: how to move from the laboratory to the clinic.,” *Radiology*, vol. 261, pp. 719–732, 2011.
- [28] Z. Huo, M. L. Giger, C. J. Vyborny, and C. E. Metz, “Breast Cancer : Effectiveness of Computer-aided Diagnosis — Observer Study with of Mammograms,” *Radiology*, vol. 224, pp. 560–568, 2002.
- [29] H. D. Cheng, X. J. Shi, R. Min, L. M. Hu, X. P. Cai, and H. N. Du, “Approaches for automated detection and classification of masses in mammograms,” *Pattern Recognit.*, vol. 39, pp. 646–668, 2006.
- [30] R. C. Gonzalez and R. E. Woods, *Digital Image Processing*, 3rd ed. Upper Saddle River, NJ: Pearson Prentice Hall, 2007.

- [31] D. Brzakovic, X. M. Luo, and P. Brzakovic, "An approach to automated detection of tumors in mammograms," *IEEE Trans. Med. Imaging*, vol. 9, pp. 233–241, 1990.
- [32] M. Kallergi, K. Woods, L. P. Clarke, W. Qian, and R. A. Clark, "Image segmentation in digital mammography: Comparison of local thresholding and region growing algorithms," *Comput. Med. Imaging Graph.*, vol. 16, pp. 323–331, 1992.
- [33] H. D. Li, M. Kallergi, L. P. Clarke, V. K. Jain, and R. A. Clark, "Markov random field for tumor detection in digital mammography," *IEEE Trans. Med. Imaging MedImg*, vol. 14, pp. 565–576, 1995.
- [34] T. McInerney and D. Terzopoulos, "Deformable models in medical image analysis: a survey.," *Med. Image Anal.*, vol. 1, pp. 91–108, 1996.
- [35] M. Kass, A. Witkin, and D. Trezopoulos, "Snakes : Active Contour Models," *Int. J. Comput. Vis.*, vol. 1, pp. 321–331, 1988.
- [36] M. Sameti, R. K. Ward, B. Palcic, and J. Morgan-Parkes, "Texture feature extraction for tumor detection in mammographic images," *1997 IEEE Pacific Rim Conf. Commun. Comput. Signal Process. PACRIM 10 Years Netw. Pacific Rim 1987/1997*, vol. 2, pp. 831–834, 1997.
- [37] Z. Huo, M. Giger, C. J. Vyborny, D. E. Wolverton, R. A. Schmidt, and K. Doi, "Automated computerized classification of malignant and benign masses on digitized mammograms," *Acad. Radiol.*, vol. 5, pp. 155–168, 1998.
- [38] R. M. Haralick and K. Shanmugam, "Textural Features for Image Classification," *IEEE Trans. Syst. Man. Cybern.*, vol. 3, pp. 610–621, 1973.
- [39] H. P. Chan, D. Wei, M. A. Helvie, B. Sahiner, D. D. Adler, M. M. Goodsitt, and N. Petrick, "Computer-aided classification of mammographic masses and normal tissue: linear discriminant analysis in texture feature space.," *Phys. Med. Biol.*, vol. 40, pp. 857–876, 1995.
- [40] R. O. Duda, P. E. Hart, and D. G. Stork, *Pattern Classification*, 2nd ed., vol. 2. New York, NY: Wiley-Interscience, 2001.
- [41] F. V Jensen, *An Introduction to Bayesian Networks*, vol. 39. New York, NY: Springer, 1996.

- [42] P. Sahoo, S. Soltani, and A. Wong, “A survey of thresholding techniques,” *Comput. Vis. Graph. Image Process.*, vol. 41, pp. 233–260, 1988.
- [43] W. M. I. Wells, W. E. L. Grimson, R. Kikinis, and F. A. Jolesz, “Adaptive segmentation of MRI data,” *IEEE Trans. Med. Imaging*, vol. 15, pp. 429–442, 1996.
- [44] J. K. Udupa and S. Samarasekera, “Fuzzy Connectedness and Object Definition: Theory, Algorithms, and Applications in Image Segmentation,” *Graph. Model. Image Process.*, vol. 58, pp. 246–261, 1996.
- [45] P. Gibbs, D. L. Buckley, S. J. Blackband, and A. Horsman, “Tumour volume determination from MR images by morphological segmentation,” *Phys. Med. Biol.*, vol. 41, pp. 2437–2446, 1996.
- [46] J. C. Bezdek, L. O. Hall, and L. P. Clarke, “Review of MR image segmentation techniques using pattern recognition.,” *Med. Phys.*, vol. 20, pp. 1033–1048, 1993.
- [47] J. C. Rajapakse, J. N. Giedd, and J. L. Rapoport, “Statistical approach to segmentation of single-channel cerebral MR images.,” *IEEE Trans. Med. Imaging*, vol. 16, pp. 176–186, 1997.
- [48] D. L. Pham, C. Xu, and J. L. Prince, “Current methods in medical image segmentation,” *Annu. Rev. Biomed. Eng.*, vol. 2, pp. 315–337, 2000.
- [49] J. Sethian, *Level Set Methods*. New York, NY: Cambridge University Press, 1996.
- [50] M. Sonka and J. Fitzpatrick, Eds., *Medical Imaging: Volume 2. Medical Image Processing and Analysis*. Bellingham, WA: SPIE, 2009.
- [51] M. Kupinski and M. Giger, “Automated seeded lesion segmentation on digital mammograms,” *IEEE Trans. Med. Imaging*, vol. 17, pp. 510–517, 1998.
- [52] I. Reiser, S. P. Joseph, R. M. Nishikawa, M. L. Giger, J. Boone, K. Lindfors, A. Edwards, N. Packard, R. H. Moore, and D. B. Kopans, “Evaluation of a 3D lesion segmentation algorithm on DBT and breast CT images,” in *Proceedings of SPIE*, 2010, vol. 7624, p. 76242N.

- [53] S. Ray, N. Prionas, K. Lindfors, and J. Boone, "Analysis of breast CT lesions using computer-aided diagnosis: an application of neural networks on extracted morphologic and texture feature," in *Proceedings of SPIE*, 2012, vol. 8315, p. 83152E-1.
- [54] M. Mancas and B. Gosselin, "Fuzzy tumor segmentation based on iterative watersheds," in *ProcRISC*, 2003.
- [55] M. Atkins and B. Mackiewich, "Fully automatic segmentation of the brain in MRI," *IEEE Trans. Med. Imaging*, vol. 17, pp. 98-107, 1998.
- [56] T. Cootes, A. Hill, C. Taylor, and J. Haslam, "The use of active shape models for locating structures in medical images," *Image Vis. Comput.*, vol. 12, pp. 355-366, 1994.
- [57] J. Yang, J. Staib, and J. Duncan, "Neighbor-constrained segmentation with level set based 3D deformable models," *IEEE Trans. Med. Imaging*, vol. 23, pp. 940-948, 2004.
- [58] F. Liu, B. Zhao, and P. Kijewski, "Liver segmentation for CT images using GVF snake," *IEEE Trans. Med. Imaging*, vol. 32, pp. 3699-3706, 2005.
- [59] G. Brake and P. Karssemeijer, "Segementation of suspicious densities in digital mammograms," *Med. Phys.*, vol. 28, pp. 259-266, 2001.
- [60] B. Sahiner, N. Petrick, H. Chan, L. Hadjiiski, C. Paramagul, M. Helvie, and M. Curcan, "Computer-aided characterization of mammographic masses: accuracy of mass segmentation and its effects on characterization," *IEEE Trans. Med. Imaging*, vol. 20, pp. 1275-1284, 2001.
- [61] Y. Yuan, M. Giger, H. Li, K. Suzuki, and C. Sennett, "A dual-stage method for lesion segmentation on digital mammograms," *Med. Phys.*, vol. 34, pp. 4180-4193, 2007.
- [62] S. Osher and J. a Sethian, "Fronts propagating with curvature-dependent speed: Algorithms based on Hamilton-Jacobi formulations," *J. Comput. Phys.*, vol. 79, pp. 12-49, 1988.
- [63] V. Caselles, F. Catt, T. Coil, and F. Dibos, "A geometric model for active contours in image processing," *Numer. Math.*, vol. 31, pp. 1-31, 1993.

- [64] R. Malladi, J. a. Sethian, and B. C. Vemuri, "Shape modeling with front propagation: a level set approach," *IEEE Trans. Pattern Anal. Mach. Intell.*, vol. 17, pp. 158–175, 1995.
- [65] C. Li, C. Xu, C. Gui, and M. Fox, "Level set evolution without re-initialization: A new variational formulation," *2005 IEEE Comput. Soc. Conf. Comput. Vis. Pattern Recognit.*, vol. 1, pp. 430–436, 2005.
- [66] D. Adalsteinsson and S. JA, "A fast level set method for propagating interfaces," *J. Comput. Phys.*, vol. 118, pp. 268–277, 1995.
- [67] D. Peng, B. Merriman, S. Osher, H. Zhao, and M. Kang, "A PDE-based fast local level set method," *J. Comput. Phys.*, vol. 155, pp. 410–438, 1999.
- [68] H. Kuo, M. L. Giger, I. S. Reiser, J. M. Boone, K. K. Lindfors, K. Yang, and A. Edwards, "Evaluation of stopping criteria for level set segmentation of breast masses in contrast-enhanced dedicated breast CT," in *Proceedings of SPIE*, 2012, vol. 8315, p. 83152C.
- [69] R. Hogg, A. Craig, and J. McKean, *Introduction to mathematical statistics*, 6th ed. Upper Saddle River, NJ: Pearson Prentice Hall, 2005.
- [70] K. H. Zou, S. K. Warfield, A. Bharatha, C. M. C. Tempany, M. R. Kaus, S. J. Haker, W. M. Wells, F. a. Jolesz, and R. Kikinis, "Statistical validation of image segmentation quality based on a spatial overlap index," *Acad. Radiol.*, vol. 11, pp. 178–189, 2004.
- [71] A. P. Zijdenbos, B. M. Dawant, R. A. Margolin, and A. C. Palmer, "Morphometric analysis of white matter lesions in MR images: method and validation," *IEEE Trans. Med. Imaging*, vol. 13, pp. 716–724, 1994.
- [72] H. Kuo, M. L. Giger, I. Reiser, K. Drukker, A. Edwards, and C. a. Sennett, "Automatic 3D lesion segmentation on breast ultrasound images," in *Proceedings of SPIE*, 2013, vol. 8670, pp. 867025.
- [73] S. Timp and N. Karssemeijer, "A new 2D segmentation method based on dynamic programming applied to computer aided detection in mammography.," 2004.
- [74] H. Kuo, M. L. Giger, I. Reiser, J. M. Boone, K. K. Lindfors, K. Yang, and A. Edwards, "Level Set Segmentation of Breast Masses in Contrast-Enhanced

- Dedicated Breast CT and Evaluation of Stopping Criteria,” *J. Digit. Imaging*, vol. 27, pp. 237-247, 2014
- [75] H. Kuo, M. L. Giger, I. Reiser, J. M. Boone, K. K. Lindfors, K. Yang, and A. Edwards, “Level Set Breast Mass Segmentation in Contrast-Enhanced and Non-contrast-Enhanced Breast CT,” in *11th International Workshop, IWDM*, 2012, pp. 697–704.
- [76] L. L. Cohen, “On active contour models and balloons,” *Comput. Vis. Graph. Image Process.*, vol. 53, pp. 211–218, 1991.
- [77] V. Caselles, R. O. N. Kimmel, and G. Sapiro, “Geodesic Active Contours,” *Int. J. Comput. Vis.*, vol. 22, pp. 61–79, 1997.
- [78] C. Li, C. Kao, J. C. Gore, and Z. Ding, “Minimization of Region-Scalable Fitting Energy for Image Segmentation,” *IEEE Trans. Image Process.*, vol. 17, pp. 1940–1949, 2008.
- [79] C. Fox, *An Introduction to the Calculus of Variations*. New York, NY: Oxford University Press, 1987.
- [80] R. W. Hamming, *Numerical Methods for Scientists and Engineers*. New York, NY: Dover Publications Inc, 1986.
- [81] I. Reiser, R. M. Nishikawa, M. L. Giger, J. M. Boone, K. K. Lindfors, and K. Yang, “Automated detection of mass lesions in dedicated breast CT: a preliminary study,” *Med. Phys.*, vol. 39, pp. 866–73, 2012.
- [82] M. J. Yaffe, J. M. Boone, N. Packard, O. Alonzo-Proulx, S. Huang, C. L. Peressotti, A. Al-Mayah, and K. Brock, “The myth of the 50-50 breast,” *Med. Phys.*, vol. 36, pp. 5437–5443, 2009.
- [83] J. J. Heine, E. E. E. Fowler, and C. I. Flowers, “Full field digital mammography and breast density: comparison of calibrated and noncalibrated measurements,” *Acad. Radiol.*, vol. 18, pp. 1430–1436, 2011.
- [84] V. A. McCormack and I. dos Santos Silva, “Breast density and parenchymal patterns as markers of breast cancer risk: a meta-analysis,” *Cancer Epidemiol. Biomarkers Prev.*, vol. 15, pp. 1159–1169, 2006.

- [85] N. F. Boyd, H. Guo, L. J. Martin, L. Sun, J. Stone, E. Fishell, R. A. Jong, G. Hislop, A. Chiarelli, S. Minkin, and M. J. Yaffe, "Mammographic density and the risk and detection of breast cancer," *N. Engl. J. Med.*, vol. 356, pp. 227–236, 2007.
- [86] C. J. D'Orsi and D. B. Kopans, "Mammographic feature analysis.," *Semin. Roentgenol.*, vol. 28, pp. 204–230, 1993.
- [87] D. B. Kopans, "Standard mammography reporting," *Radiol. Clin. North Am.*, vol. 30, pp. 257–261, 1992.
- [88] T. Franquet, C. D. Miguel, R. Cozcolluela, and L. Donoso, "Spiculated Lesions of the Breast : Mammographic-Pathologic Correlation," *RadioGraphics*, vol. 13, pp. 841–852, 1993.
- [89] W. P. Kegelmeyer, "Computer detection of stellate lesions in mammograms," in *Proceedings of SPIE*, 1992, pp. 446–454.
- [90] J. Kilday, F. Palmieri, and M. D. Fox, "Classifying mammographic lesion using computerized image analysis," *IEEE Trans. Med. Imaging*, vol. 12, pp. 664–669, 1993.
- [91] M. L. Giger, C. J. Vyborny, and R. A. Schmidt, "Computerized characterization of mammographic masses: analysis of spiculation," *Cancer Lett.*, vol. 77, pp. 201–211, 1994.
- [92] Z. Huo, M. L. Giger, C. J. Vyborny, U. Bick, P. Lu, D. E. Wolverton, and R. a Schmidt, "Analysis of spiculation in the computerized classification of mammographic masses.," *Med. Phys.*, vol. 22, pp. 1569–1579, 1995.
- [93] B. Sahiner, H.-P. Chan, N. Petrick, M. a. Helvie, and L. M. Hadjiiski, "Improvement of mammographic mass characterization using spiculation measures and morphological features," *Med. Phys.*, vol. 28, pp. 1455–1465, 2001.
- [94] E. a Sickles, D. L. Miglioretti, R. Ballard-Barbash, B. M. Geller, J. W. T. Leung, R. D. Rosenberg, R. Smith-Bindman, and B. C. Yankaskas, "Performance benchmarks for diagnostic mammography.," *Radiology*, vol. 235, pp. 775–790, 2005.

- [95] K. G. Gilhuijs, M. L. Giger, and U. Bick, "Computerized analysis of breast lesions in three dimensions using dynamic magnetic-resonance imaging.," *Med. Phys.*, vol. 25, pp. 1647–1654, 1998.
- [96] W. Chen, M. L. Giger, H. Li, U. Bick, and G. M. Newstead, "Volumetric texture analysis of breast lesions on contrast-enhanced magnetic resonance images," *Magn. Reson. Med.*, vol. 58, pp. 562–571, 2007.
- [97] C. E. Metz, "Basic Principles of ROC analysis," *Semin. Nucl. Med.*, vol. 8, pp. 283–298, 1978.
- [98] M. L. Giger, D. P. Miller, J. B. Brown, M. F. Inciardi, C. E. Metz, Y. Jiang, R. F. Brem, R. M. Nishikawa, A. V. Edwards, and J. Papaioannou, "Clinical reader study examining the performance of mammography and automatic breast ultrasound in breast cancer screening," in *RSNA*, 2012, pp. SSJ01–04.
- [99] K. Drukker, K. J. Horsch, L. L. Pesce, and M. L. Giger, "Interreader scoring variability in an observer study using dual-modality imaging for breast cancer detection in women with dense breasts," *Acad. Radiol.*, vol. 20, pp. 847–853, 2013.

VITA

NAME: Hsien-Chi Kuo

EDUCATION: B.S., Biochemical Science and Technology,
National Taiwan University, Taipei, Taiwan, 2006

Ph.D., Bioengineering, University of Illinois at Chicago,
succesfully defended in 2013

RESEARCH EXPERIENCE: **Department of Radiology, The University of Chicago,
Chicago, IL, USA**

Research Advisor: Maryellen L. Giger, PhD
Development of CADx system for dedicated breast CT and 3D
breast ultrasound. (2010 to present)

**Bioinformatics and Biostatistics Core, Center for Genomic
Medicine, National Taiwan University, Taipei, Taiwan**

Research Advisor: Eric Y. Chuang, PhD
Development of online analytic tools for DNA methylation
microarray: DBCAT (<http://dbcat.cgm.ntu.edu.tw/>) (2008 - 2009)

PROFESSIONAL AND ACADEMIC MEMBERSHIPS: Student Member, Biomedical Engineering Society
Student Member, The International Society for Optics and
Photonics

Student Member, American Chemical Society
HonorSociety.org

ABSTRACTS: **H. Kuo**, M. L. Giger, I. Reiser, K. Drukker, J. M. Boone, K. K.
Lindfors, K. Yang, C. A. Sennett, and A. Edwards, "Computerized
3D segmentation of breast tumors on dedicated breast CT and 3D
ultrasound," in *MBECC*, 2013, Chicago, US.

H. Kuo, M. L. Giger, I. Reiser, K. Drukker, J. M. Boone, K. K.
Lindfors, K. Yang, C. A. Sennett, and A. Edwards, "Computerized
3D segmentation of breast tumors on dedicated breast CT," in
UC-NorthShore Joint Institutional Symposium, 2012, Chicago,
US.

PUBLICATIONS: **H. Kuo**, M. L. Giger, I. Reiser, K. Drukker, J. M. Boone, K. K. Lindfors, K. Yang, and A. Edwards, "Computer classification of breast masses on dedicated breast CT using 3D lesion surface analysis," submitted for publication, under review.

H. Kuo, M. L. Giger, I. Reiser, K. Drukker, J. M. Boone, K. K. Lindfors, K. Yang, A. Edwards, and C. A. Sennett, "Segmentation of breast masses on dedicated breast CT and 3D breast ultrasound images," *Journal of Medical Imaging*, accepted for publication.

H. Kuo, M. L. Giger, I. Reiser, J. M. Boone, K. K. Lindfors, K. Yang, and A. Edwards, "Level set segmentation of breast masses in contrast-enhanced dedicated breast CT and evaluation of stopping criteria," *Journal of Digital Imaging*, e-published ahead of print, DOI: 10.1007/s10278-013-9652-1

H. Kuo, M. L. Giger, I. Reiser, K. Drukker, C. A. Sennett, and A. Edwards, "Automatic 3D lesion segmentation on breast ultrasound images," *Proceedings of SPIE*, vol. 8670, pp. 867025, 2013.

H. Kuo, M. L. Giger, I. Reiser, J. M. Boone, K. K. Lindfors, K. Yang, and A. Edwards, "Level set breast mass segmentation in contrast-enhanced and non-contrast-enhanced breast CT," *IWDM*, vol. LNCS 7361, pp. 697-704, 2012.

H. Kuo, M. L. Giger, I. Reiser, J. M. Boone, K. K. Lindfors, K. Yang, and A. Edwards, "Evaluation of level set model and stopping criteria for breast CT lesion segmentation," *Proceedings of SPIE*, vol. 8315, pp. 83152C, 2012.

H. Kuo, P. Lin, T. Chung, C. Chao, L. Lai, M. Tsai, and E. Y. Chuang, "DBCAT: Database of CpG islands and analytical tools for identifying comprehensive methylation profiles in cancer cells," *Journal of Computational Biology*, vol. 18, pp. 1013-1017, 2011.

Appendix

The reprint permissions are included in appendix:



American Association of Physicists in Medicine

One Physics Ellipse
College Park, MD 20740-3846
(301) 209-3350
Fax (301) 209-0862
<http://www.aapm.org>

Office of the Executive Director

Angela R. Keyser
Phone: 301-209-3385 Fax: 301-209-0862
E-mail: akeyser@aapm.org

DATE OF REQUEST: 3/4/2014

FROM:

Hsien-Chi Kuo
1000 N LaSalle Dr Apt 213 Chicago IL 60610 USA

EMAIL ADDRESS: hkuo6@uic.edu

1. Permission is granted to:

Hsien-Chi Kuo, University of Illinois at Chicago

2. Permission is requested to use the following material:

Maryellen L. Giger, Heang-Ping Chan and John Boone, "Anniversary Paper: History and status of CAD and quantitative image analysis: The role of Medical Physics and AAPM." *Med. Phys.* 35(12) 5799-5820 (2008).

Fig 1 and Fig 3 being used.

3. For what purpose:

Dissertation

Title: Development and Evaluation of Computerized Segmentation Algorithm for 3D Multimodality Breast Images

Authors seeking permission must also notify the first author of the article from which permission is being sought.

Permission is hereby granted:


Signature

March 12, 2014
Date

Submit via Email

Reset Form

The Association's Journals are *Medical Physics* and *Journal of Applied Clinical Medical Physics*
Member Society of the American Institute of Physics and the International Organization of Medical Physics

RE: Reprint permission request

From: Karen Thomas
Sent: Friday, March 07, 2014 5:05:51 AM
To: Hsien-Chi Kuo (mars930@msn.com)

Hsien-Chi Kuo,

Thank you for seeking permission from SPIE to reprint material from our publications. As author, SPIE shares the copyright with you, so you retain the right to reproduce your paper in part or in whole.

Publisher's permission is hereby granted under the following conditions:

(1) the material to be used has appeared in our publication without credit or acknowledgment to another source; and

(2) you credit the original SPIE publication. Include the authors' names, title of paper, volume title, SPIE volume number, and year of publication in your credit statement.

Sincerely,

Karen Thomas for

Eric Pepper, Director of Publications

SPIE

P.O. Box 10, Bellingham WA 98227-0010 USA

360/676-3290 (Pacific Time) eric@spie.org

From:
Sent: Tuesday, March 04, 2014 7:51 PM

reprint_permission

Subject: Reprint permission request

Good morning,

My name is Hsien-Chi Kuo, a PhD candidate working in Dr. Giger's lab at the University of Chicago.

Recently I am about to finalize my dissertation.

In my dissertation, I used the materials from the papers that I have and is going to publish in SPIE proceedings and journals.

I am writing this email for the permission which allows me to use those materials in my dissertation.

The papers are as follow:

1.

H. Kuo, M. L. Giger, I. S. Reiser, J. M. Boone, K. K. Lindfors, K. Yang, and A. Edwards, "Evaluation of stopping criteria for level set segmentation of breast masses in contrast-enhanced dedicated breast CT," in *Proceedings of SPIE*, 2012, vol. 8315, pp. 83152C.

2.

H. Kuo, M. L. Giger, I. Reiser, K. Drukker, A. Edwards, and C. A. Sennett, "Automatic 3D lesion segmentation on breast ultrasound images," in *Proceedings of SPIE*, 2013, vol. 8670, pp. 867025.

3.

H. Kuo, M. L. Giger, I. Reiser, K. Drukker, J. M. Boone, K. K. Lindfors, K. Yang, A. Edwards, and C. A. Sennett, "Segmentation of breast masses on dedicated breast CT and 3D breast ultrasound images," *Journal of Medical Imaging*, accepted for publication in Jan 2014.

Here I kindly request a permission that I can use whole text of above 3 papers in my dissertation.

**SPRINGER LICENSE
TERMS AND CONDITIONS**

Mar 04, 2014

This is a License Agreement between Hsien-Chi Kuo ("You") and Springer ("Springer") provided by Copyright Clearance Center ("CCC"). The license consists of your order details, the terms and conditions provided by Springer, and the payment terms and conditions.

information listed at the bottom of this form.

License Number	3342240778301
License date	Mar 04, 2014
Licensed content publisher	Springer
Licensed content publication	Journal of Digital Imaging
Licensed content title	Level Set Segmentation of Breast Masses in Contrast-Enhanced Dedicated Breast CT and Evaluation of Stopping Criteria
Licensed content author	Hsien-Chi Kuo
Licensed content date	Jan 1, 2013
Type of Use	Thesis/Dissertation
Portion	Full text
Number of copies	1
Author of this Springer article	Yes and you are the sole author of the new work
Order reference number	74
Title of your thesis / dissertation	Development and Evaluation of Computerized Segmentation Algorithm for 3D Multimodality Breast Images
Expected completion date	Mar 2014
Estimated size(pages)	120
Total	0.00 USD

Terms and Conditions

Introduction

The publisher for this copyrighted material is Springer Science + Business Media. By clicking "accept" in connection with completing this licensing transaction, you agree that the following terms and conditions apply to this transaction (along with the Billing and Payment terms and conditions established by Copyright Clearance Center, Inc. ("CCC"), at the time that you opened your Rightslink account and that are available at any time at _____).

Limited License

With reference to your request to reprint in your thesis material on which Springer Science and

Business Media control the copyright, permission is granted, free of charge, for the use indicated in your enquiry.

Licenses are for one-time use only with a maximum distribution equal to the number that you identified in the licensing process.

This License includes use in an electronic form, provided its password protected or on the university's intranet or repository, including UMI (according to the definition at the Sherpa website: <http://www.sherpa.ac.uk/romeo/>). For any other electronic use, please contact Springer at (permissions.dordrecht@springer.com or permissions.heidelberg@springer.com).

The material can only be used for the purpose of defending your thesis, and with a maximum of 100 extra copies in paper.

Although Springer holds copyright to the material and is entitled to negotiate on rights, this license is only valid, subject to a courtesy information to the author (address is given with the article/chapter) and provided it concerns original material which does not carry references to other sources (if material in question appears with credit to another source, authorization from that source is required as well).

Permission free of charge on this occasion does not prejudice any rights we might have to charge for reproduction of our copyrighted material in the future.

Altering/Modifying Material: Not Permitted

You may not alter or modify the material in any manner. Abbreviations, additions, deletions and/or any other alterations shall be made only with prior written authorization of the author(s) and/or Springer Science + Business Media. (Please contact Springer at (permissions.dordrecht@springer.com or permissions.heidelberg@springer.com))

Reservation of Rights

Springer Science + Business Media reserves all rights not specifically granted in the combination of (i) the license details provided by you and accepted in the course of this licensing transaction, (ii) these terms and conditions and (iii) CCC's Billing and Payment terms and conditions.

Copyright Notice:Disclaimer

You must include the following copyright and permission notice in connection with any reproduction of the licensed material: "Springer and the original publisher /journal title, volume, year of publication, page, chapter/article title, name(s) of author(s), figure number(s), original copyright notice) is given to the publication in which the material was originally published, by adding; with kind permission from Springer Science and Business Media"

Warranties: None

Example 1: Springer Science + Business Media makes no representations or warranties with respect to the licensed material.

Example 2: Springer Science + Business Media makes no representations or warranties with

respect to the licensed material and adopts on its own behalf the limitations and disclaimers established by CCC on its behalf in its Billing and Payment terms and conditions for this licensing transaction.

Indemnity

You hereby indemnify and agree to hold harmless Springer Science + Business Media and CCC, and their respective officers, directors, employees and agents, from and against any and all claims arising out of your use of the licensed material other than as specifically authorized pursuant to this license.

No Transfer of License

This license is personal to you and may not be sublicensed, assigned, or transferred by you to any other person without Springer Science + Business Media's written permission.

No Amendment Except in Writing

This license may not be amended except in a writing signed by both parties (or, in the case of Springer Science + Business Media, by CCC on Springer Science + Business Media's behalf).

Objection to Contrary Terms

Springer Science + Business Media hereby objects to any terms contained in any purchase order, acknowledgment, check endorsement or other writing prepared by you, which terms are inconsistent with these terms and conditions or CCC's Billing and Payment terms and conditions. These terms and conditions, together with CCC's Billing and Payment terms and conditions (which are incorporated herein), comprise the entire agreement between you and Springer Science +

In the event of any conflict between your obligations established by these terms and conditions and those established by CCC's Billing and Payment terms and conditions, these terms and conditions shall control.

Jurisdiction

All disputes that may arise in connection with this present License, or the breach thereof, shall be settled exclusively by arbitration, to be held in The Netherlands, in accordance with Dutch law, and to be conducted under the Rules of the 'Netherlands Arbitrage Instituut' (Netherlands Institute of Arbitration). **OR:**

All disputes that may arise in connection with this present License, or the breach thereof, shall be settled exclusively by arbitration, to be held in the Federal Republic of Germany,

Other terms and conditions:

v1.3

If you would like to pay for this license now, please remit this license along with your payment made payable to "COPYRIGHT CLEARANCE CENTER" otherwise you will be invoiced within 48 hours of the license date. Payment should be in the form of a check or money order referencing your account number and this invoice number RLNK501242068. Once you receive your invoice for this order, you may pay your invoice by credit card.

**SPRINGER LICENSE
TERMS AND CONDITIONS**

Mar 04, 2014

This is a License Agreement between Hsien-Chi Kuo ("You") and Springer ("Springer") provided by Copyright Clearance Center ("CCC"). The license consists of your order details, the terms and conditions provided by Springer, and the payment terms and conditions.

information listed at the bottom of this form.

License Number	3342251393597
License date	Mar 04, 2014
Licensed content publisher	Springer
Licensed content publication	Springer eBook
Licensed content title	Level Set Breast Mass Segmentation in Contrast-Enhanced and Non-Contrast-Enhanced Breast CT
Licensed content author	Hsien-Chi Kuo
Licensed content date	Jan 1, 2012
Type of Use	Thesis/Dissertation
Portion	Full text
Number of copies	1
Author of this Springer article	Yes and you are the sole author of the new work
Order reference number	75
Title of your thesis / dissertation	Development and Evaluation of Computerized Segmentation Algorithm for 3D Multimodality Breast Images
Expected completion date	Mar 2014
Estimated size(pages)	120
Total	0.00 USD

Terms and Conditions

Introduction

The publisher for this copyrighted material is Springer Science + Business Media. By clicking "accept" in connection with completing this licensing transaction, you agree that the following terms and conditions apply to this transaction (along with the Billing and Payment terms and conditions established by Copyright Clearance Center, Inc. ("CCC"), at the time that you opened your Rightslink account and that are available at _____).

Limited License

With reference to your request to reprint in your thesis material on which Springer Science and

Business Media control the copyright, permission is granted, free of charge, for the use indicated in your enquiry.

Licenses are for one-time use only with a maximum distribution equal to the number that you identified in the licensing process.

This License includes use in an electronic form, provided its password protected or on the university's intranet or repository, including UMI (according to the definition at the Sherpa website: <http://www.sherpa.ac.uk/romeo/>). For any other electronic use, please contact Springer at (permissions.dordrecht@springer.com or permissions.heidelberg@springer.com).

The material can only be used for the purpose of defending your thesis, and with a maximum of 100 extra copies in paper.

Although Springer holds copyright to the material and is entitled to negotiate on rights, this license is only valid, subject to a courtesy information to the author (address is given with the article/chapter) and provided it concerns original material which does not carry references to other sources (if material in question appears with credit to another source, authorization from that source is required as well).

Permission free of charge on this occasion does not prejudice any rights we might have to charge for reproduction of our copyrighted material in the future.

Altering/Modifying Material: Not Permitted

You may not alter or modify the material in any manner. Abbreviations, additions, deletions and/or any other alterations shall be made only with prior written authorization of the author(s) and/or Springer Science + Business Media. (Please contact Springer at (permissions.dordrecht@springer.com or permissions.heidelberg@springer.com))

Reservation of Rights

Springer Science + Business Media reserves all rights not specifically granted in the combination of (i) the license details provided by you and accepted in the course of this licensing transaction, (ii) these terms and conditions and (iii) CCC's Billing and Payment terms and conditions.

Copyright Notice:Disclaimer

You must include the following copyright and permission notice in connection with any reproduction of the licensed material: "Springer and the original publisher /journal title, volume, year of publication, page, chapter/article title, name(s) of author(s), figure number(s), original copyright notice) is given to the publication in which the material was originally published, by adding; with kind permission from Springer Science and Business Media"

Warranties: None

Example 1: Springer Science + Business Media makes no representations or warranties with respect to the licensed material.

Example 2: Springer Science + Business Media makes no representations or warranties with

respect to the licensed material and adopts on its own behalf the limitations and disclaimers established by CCC on its behalf in its Billing and Payment terms and conditions for this licensing transaction.

Indemnity

You hereby indemnify and agree to hold harmless Springer Science + Business Media and CCC, and their respective officers, directors, employees and agents, from and against any and all claims arising out of your use of the licensed material other than as specifically authorized pursuant to this license.

No Transfer of License

This license is personal to you and may not be sublicensed, assigned, or transferred by you to any other person without Springer Science + Business Media's written permission.

No Amendment Except in Writing

This license may not be amended except in a writing signed by both parties (or, in the case of Springer Science + Business Media, by CCC on Springer Science + Business Media's behalf).

Objection to Contrary Terms

Springer Science + Business Media hereby objects to any terms contained in any purchase order, acknowledgment, check endorsement or other writing prepared by you, which terms are inconsistent with these terms and conditions or CCC's Billing and Payment terms and conditions. These terms and conditions, together with CCC's Billing and Payment terms and conditions (which are incorporated herein), comprise the entire agreement between you and Springer Science +

In the event of any conflict between your obligations established by these terms and conditions and those established by CCC's Billing and Payment terms and conditions, these terms and conditions shall control.

Jurisdiction

All disputes that may arise in connection with this present License, or the breach thereof, shall be settled exclusively by arbitration, to be held in The Netherlands, in accordance with Dutch law, and to be conducted under the Rules of the 'Netherlands Arbitrage Instituut' (Netherlands Institute of Arbitration). **OR:**

All disputes that may arise in connection with this present License, or the breach thereof, shall be settled exclusively by arbitration, to be held in the Federal Republic of Germany,

Other terms and conditions:

v1.3

If you would like to pay for this license now, please remit this license along with your payment made payable to "COPYRIGHT CLEARANCE CENTER" otherwise you will be invoiced within 48 hours of the license date. Payment should be in the form of a check or money order referencing your account number and this invoice number RLNK501242068. Once you receive your invoice for this order, you may pay your invoice by credit card.